Micromechanical modeling of rough interface behavior

BY

Shiping Huang

Submitted to the graduate degree program in the Department of Civil, Environmental, and Architectural Engineering and the Graduate Faculty of the University of Kansas in partial fulfillment of the requirements for the degree of Doctor of Philosophy in Civil Engineering

Chairperson Dr. Anil Misra

Committee Members

Dr. Jie Han

Dr. Robert L. Parsons

Dr. Xinmai Yang

Dr. Weishi Liu

Date Defended: July 28, 2011

The Dissertation Committee for Shiping Huang

certifies that this is the approved version of the following dissertation:

Micromechanical modeling of rough interface behavior

_____

Chairperson Dr. Anil Misra

Date approved: July 28, 2011

Abstract

In this dissertation, the interface behavior of contacting rough surfaces was studied systematically based upon micromechanical modeling. Firstly, asperity contact mechanics was further developed. It was found that tangential tractions, displacement and compliance are path dependent in both in-plane and out-of-plane shear loading, which lead to energy dissipation during the loading. Secondly, statistical description of interface geometry was obtained based upon random process model of rough surfaces. As a result, the probability distributions of asperity contact height, curvature, and orientation were derived. Thirdly, asperity contact mechanics and interface description were considered to develop a homogenization model. The resultant nonlinear stress-displacement relationship of the interface was solved numerically using the Newton method. Finally, the proposed model was used to study the interface behavior. It was shown that normal stiffness of the rough interface is softer than that of the smooth interface, which is highly nonlinear and does not follow the Hertz power law. It was also shown that the shear behavior of the interfaces under constant normal stress exhibits two distinct regimes during shear loading. In the small shear displacement regime, the smooth interfaces were found to have a higher shear resistance. In the large shear displacement regime, the rough interfaces were found to have a higher shear resistance, and eventually, a higher frictional strength compared to smooth interfaces. Furthermore, the scale

dependency of the rough interface was discussed. We found that fractal dimension, sample size and resolution have strong effects on the interface behavior.

Keywords: Contact mechanics; Asperity contact mechanics; Random process; Rough interface; Shear behavior; Scale dependency

Acknowledgement

I would like to gratefully and sincerely thank Dr. Misra for his guidance, understanding, patience, and support during my PhD studies at the University of Kansas. Without his help, this work could never been done. In the last three years, he always sides with me and brings me into a new world of science.

I would like to thank those members of my doctoral committee for their time, valuable discussions. I also benefit a lot from their classes.

I also would like to thank my friends in Lawrence, especially those friends in KUGS, BERC. They make my life in Lawrence wonderful.

Finally, I would like to thank my parents for their love and understanding.

This page left intentionally blank.

Contents

Figures

Tables

Chapter 1 Introduction

1.1 Overview of problem

All surfaces are rough (see Figure 1.1) by nature irrespective of the scale of observation. The contact mechanics of interfaces formed by joining surfaces is, therefore, a fundamental problem in engineering. The understanding of the rough contact behavior and its effective modeling continues to be a challenging problem even with contributions spanning more than a century. Generally, two categories of loading are applied to study the rough interface contact behavior, as shown in Figure 1.2.

The pioneering work related to the contact mechanics of deformable bodies is attributed to Hertz [1, 2] who developed the stress-displacement relationship of contact between two perfectly smooth convex elastic bodies under normal interfacial loading. Hertz's work was subsequently extended to a variety of loading conditions and material behavior, notable among which is the solution for the contact behavior of two smooth spheres under combined normal and shear loading by Mindlin and Deresiewicz in 1953[3]. Hertz-Mindlin solutions have provided the foundation of most developments in contact mechanics. However, since the middle of the last century, there has been an increasing realization that even the elastic contact behavior between real surfaces is much more complicated than that predicted by Hertz and Mindlin solutions. The root cause of this complexity, that has confounded the development of universal approaches for contact

models, is the presence of numerous irregular asperities which strongly affect the contact behavior.

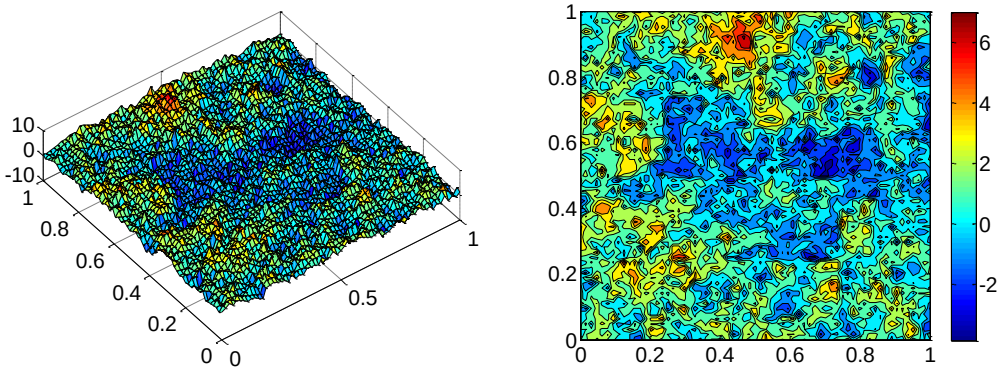

Figure 1.1: Scan of a rough micro-mechanical surface geometry.

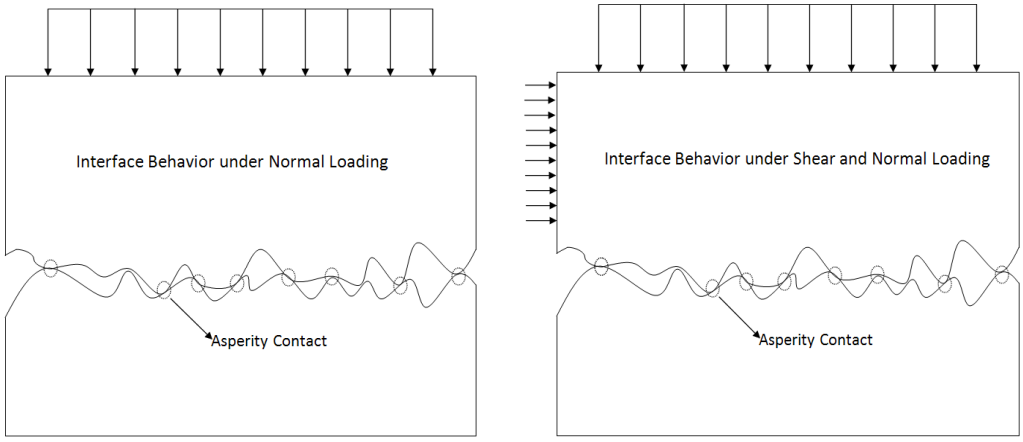

Figure 1.2: Interface behavior under two loading conditions.

1.2 Brief literature review

Numerous researchers have investigated approaches for incorporating the effect of asperity contacts. The notable early efforts along these lines can be traced to the works of Archard [4], Bowden and Tabor [5], and Greenwood and coworkers[6, 7]. The recent

approaches of rough contact modeling can be considered in three categories based upon how the surface roughness is incorporated in the calculations: (1) direct simulation using the finite element method [8-13], (2) fractal representation [11, 14-17] and (3) statistical methods [6, 7, 18-29].

Direct simulation of rough contact is useful for providing perceptual intuition and showing details of the local behavior at the interfaces [8-13]. Most contact problems in practice could not be solved analytically since they involve solving highly nonlinear partial differential equations system. Therefore, to obtain a deeper understanding of contact problems under both normal and shear loading, numerical approach, such as the finite element and the meshfree methods have been utilized recently (see [9-11, 30-33]and many others). The foremost limitation of the finite element and meshfree methods remains their computational expense especially when dealing with 3-dimensional contact problems involving numerous asperities.

Along the lines of fractal representation, a number of authors have shown that the rough interface demonstrates self-affine feature which indicates the geometry of the interface are scale dependent [11, 14-17]. The fractal model was proposed to account for such feature. However, the fractal model typically does not incorporate the local asperity

contact behavior which is important when considering the shear behavior. Furthermore, many material like thin-film disks, magnetic tapes and geotechnical materials have been shown to have little scale dependency and can be described by statistical approach [34]. In contrast to the fractal approach, the statistical approach is an asperity contact based model, in which the interface behavior is described as a group effect of numerous local asperity contacts [6, 7, 18-29]. The advantage of the statistical method is that it not only considers the local behavior of contacting surface, but also describes the interface geometry in a simple way. Therefore, this method continues to be attractive for describing rough surface contact behavior and is used in this dissertation.

Among the early efforts of the statistical method, Greenwood and Williamson[6] introduced this approach to describe the roughness of the interface, assuming each asperity had the same radius but different heights. Since then statistical methods have prevailed and a vast amount of literature has been contributed to this field. Whitehouse and Archard[18] developed the Greenwood and Williamson (G-W) model by accounting for the random radii of curvature of the asperity tips. Nayak[19, 35, 36] introduced the techniques of random process theory into the analysis of Gaussian roughness which was subsequently used by Bush, Gibson and Thomas[20] in rough surface contact. Adler and Firman[22] proposed a non-Gaussian random surfaces; Yamada, Takeda, Kagami and Naoi[37, 38] derived their contact model formed by two rough surfaces described by

probability density function of the peak height of each asperity; Brown and Scholz[24, 25] presented a composite height model for the contact between two random nominally flat elastic surfaces. McCool and co-worker[23, 39] treated anisotropic rough surfaces with ellipsoidal asperities; however, they found a good agreement with the simpler G-W model and suggested that spherical shape asperity assumption is not only simplifying but also representative of the asperity contact behavior. A preponderance of the above-cited work[6, 18, 20, 23, 24, 39] was concerned with contact behavior under loading in the normal direction to the nominal orientation of the interface. Under shear loading, sliding of asperity contact becomes significant in determining the overall friction of the interface. The early work related to the modeling of friction of the rough interface was done by Archard[4]. Contact friction and its dependence on interface roughness has been widely recognized and deemed important in a variety of problems as seen from the recent works of Ozaki, Hashiguchi, Okayasu and Chen[40], Guz, Menshykov, Zozulya and Guz[41]; Guz and Zozulya[42], Vignjevic, De Vuyst and Campbell [30] and many others. Clearly, both contact closure and friction modeling remains an active area and satisfactory models for rough contacts under combined normal and shear loading remain elusive. Consequently, this approach continues to be developed and refined as evident from recent works on viscoelastic [43-46], elasto-plastic [47-50], and anisotropic interfaces [51-55]. A micromechanics based statistical approach that incorporates asperity contact

orientation distribution and iterative approaches has been developed and applied to model anisotropic interfaces [56], and surfaces undergoing damage [57]. More recently, we have utilized this approach to develop numerical implementation applicable for modeling rough contact behavior under combined normal and shear loading [58, 59].

Most statistical approaches reviewed above consider either the contact of one rough surface with a nominally flat surface or two surfaces treated as one new equivalent rough surface in contact with a flat surface. It is noted that when one rough surface comes into contact with a flat surface, the asperity contacts are only observed in vertical direction, which is not true in the real case. For two rough surfaces, the asperity contact can form between any two points of the surfaces. In this case, the relationship between surface topography measurements and the statistical descriptions of actual asperity contacts need to consider the geometry of both surfaces. In addition, the application of the statistical methods has been mostly to closure behavior under loading in the normal direction to the nominal orientation of the interface. The applications of the statistical methods to the shear behavior as well as the coupled shear and normal behavior of rough interfaces have been relatively few [4, 27, 29, 34, 60]. Undoubtedly, there is a need to investigate both the geometry of two rough surfaces contact as well as the mechanical response of this contact when subjected to combined normal-shear loading.

1.3 Focus and structure in this dissertation

The main purpose in this dissertation is to study the interface behavior of rough surfaces via micromechanical modeling. To this end, three fundamental aspects have been discussed in details :(1) asperity contact mechanics, which is considered in chapter 2 and chapter 3, (2) rough contacting surface geometry description, which is developed in chapter 4, and (3) homogenization of asperity contact behavior to obtain the interface contact behavior, which is proposed in chapter 5. Furthermore, scale dependency effects have been discussed in chapter 6.

This page left intentionally blank.

Chapter 2 Asperity Contact Mechanics – In-plane Loading

The rough interface behavior is the group effect of the local behaviors. Thus the local behavior, i.e., asperity contact mechanics, is essential to rough interface behavior. Traditionally, asperity contact is simplified as sphere contact problem. Therefore, for the contact between nonconforming solids, the contact mechanics of elastic spheres has served as a benchmark and as a fundamental basis for rough contact mechanics [6, 18, 20, 24, 26, 29, 58] and granular mechanics [67, 68].

The pioneering work of sphere contact problem under normal loading was published by Hertz in 1881 and 1882 [1, 2]. From then on, the sphere contact problem has attracted many researchers. Cattaneo and Mindlin independently derived the force-displacement relationship when considering combined normal and shear loading [3, 63, 64, 69] (referred as C-M solutions hereafter). In a number of applications relating to contact of solid bodies the contact force is oblique containing both normal and tangential force components. By dividing the loading into infinite loading steps, Mindlin and Deresiewicz [3] made use of the sphere contact solution under constant normal force to derive the force-displacement relationships under varying oblique forces. The solutions given by Mindlin and Deresiewicz are widely cited, although seldom used in their complete form.

In most applications, these solutions have been modified or simplified to reduce the computational requirements [70, 71].

Mindlin and Deresiewicz [3], abbreviated as MD53 hereafter, presented an analysis of the contact behavior of elastic spheres by considering the history of changes in normal and tangential forces. In that paper, they investigated the changes in surface traction and compliance between spherical bodies in contact arising from the various potential combinations of incremental change in loads. Their classic solution has been adopted for application in many areas, including mechanics of rough surfaces, granular and fractured materials. In their pioneering paper, Mindlin and Deresiewicz first discussed the incremental approach in detail (Sections 7-13 of MD53); they then derived the continuous approach under an oscillating oblique force with constant inclination (Sections 14-19 of MD53). Using the incremental approach, expressions for compliance can be obtained as the contact is subjected to a change in the normal or tangential force under a given current contact loading condition. The incremental approach has been widely used in mechanics of granular materials, such as the discrete element method [61]. However, as noted in Section 17 of MD53, the incremental approach does not necessarily yield the same result as the continuous approach. Thus only the current loading condition is not enough to determine the compliance and loading history must be incorporated. For example, in many applications, the contacts are subjected to oblique forces whose

inclination is different at different loading stages. Moreover, in general, the initial tangential traction for cyclic variation of the oblique force is more complex than that considered in MD53. Alternate approaches to the tangential problems have been developed in terms of 2-d plasticity [34, 62]. The plasticity-based approaches have the ability to model the contact behavior under loading with varying oblique forces and have shown good agreement with the cases discussed in MD53 [62]. However, these plasticity approaches are phenomenological and differ fundamentally from the approach by Mindlin and Deresiewicz, which is based upon elasticity theory and considers the compatibility of displacements in the non-slip contact region.

To address the cases involving variation of oblique force inclination and complex initial tangential traction under cyclic loading, we further develop the continuous approach described in MD53. We present a general procedure for obtaining the expression for the tangential traction which contains the loading history information. We then derive the shear displacement and compliance of elastic spheres subjected to oblique force whose inclination changes during the loading process. We have also applied our general procedure to investigate the cyclic behavior under complicated initial tangential traction. To be consistent with MD53, the friction coefficient is denoted by f, and the shear modulus by μ in chapter 2 and 3, however, in later chapters (chapter 5 and chapter 6) the friction coefficient is denoted by μ and shear modulus by G.

2.1 Basic formulation for Hertz-Mindlin system

The Mindlin-Deresiewicz analysis is based upon the following four assumptions:

1) Normal loading obeys Hertz theory [1, 2] and the normal traction is not disturbed by tangential traction.
2) Prior to contact sliding, an infinitesimal tangential force dT will result in a uniform infinitesimal tangential deformation of the contact surface. The contact problem is, therefore, posed as a mixed boundary-value problem in elasticity.
3) The surface tangential deformation is uniquely determined by the tangential traction.
4) Amonton's law should be satisfied, which requires that the tangential traction not exceed the slip limit in contacting surface.

In the subsequent discussion, we first describe the seminal equations derived by [1, 2] and [63] since these are later used in our results.

2.2 Tangential traction under oscillating tangential force and constant normal force

For contact of spherical bodies, the Hertz theory gives the relationship of circular contact surface radius and normal force as:

$$a = (KNR)^{1/3} \tag{2.1}$$

where N is the normal force, R is the radius of spheres, and $K = 3(1-\nu^2)/4E$, in which ν and E are the material Poisson's ratio and Young's modulus, respectively. The normal displacement and the distribution of normal traction on the contact surface is given by

$$\delta_n = \frac{a^2}{R} \tag{2.2}$$

$$\sigma = \frac{3N}{2\pi a^3}(a^2 - \rho^2)^{1/2} \tag{2.3}$$

If a tangential force T is applied while keeping the normal force N constant, the contact surface will experience a uniform displacement and the tangential traction is given by

$$\tau = \frac{T}{2\pi a^2}(1-\frac{\rho^2}{a^2})^{-1/2} \tag{2.4}$$

assuming that the friction coefficient, f, is infinite, that is no slip or sliding is considered in this process. As seen in equation(2.4), as ρ approaches a, the shear stress goes to infinity which will, in general, exceed the friction limit, $\tau = f\sigma$. Therefore, in practice, slip will go inward from the boundary to the center as T increases. Thus equation (2.4) is not valid and the tangential traction is given by (as shown in Figure 2.1(a))

$$\begin{aligned} \tau &= \frac{3fN}{2\pi a^3}(a^2 - \rho^2)^{1/2}, c \le \rho \le a \\ \tau &= \frac{3fN}{2\pi a^3}\left[(a^2 - \rho^2)^{1/2} - (c^2 - \rho^2)^{1/2}\right], \rho \le c \end{aligned} \tag{2.5}$$

where c is given by

$$c = a(1-\frac{T}{fN})^{1/3} \tag{2.6}$$

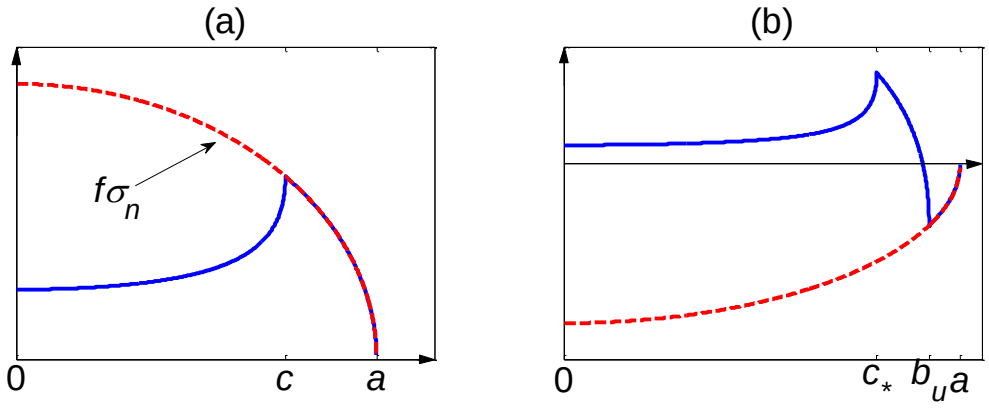

Figure 2.1: Tangential tractions under constant normal force given by the solid line where dashed line gives the slip limit.

If the whole contact surface reaches the friction limit (that is, c=0), the tangential traction is given by

$$\tau = \frac{3fN}{2\pi a^3}(a^2 - \rho^2)^{1/2} \tag{2.7}$$

Thus the tangential force reaches the magnitude $T = fN$ and the contact surface begins to slide. In this chapter, our discussion is limited to tangential force T less than fN.

The displacement of distant points with respect to the uniform displacement of the 'stick' area is given by

$$\delta = \frac{3(2-\nu)fN}{16\mu a}(1-\frac{c^2}{a^2}) = \frac{3(2-\nu)fN}{16\mu a}\left[1-(1-\frac{T}{fN})^{2/3}\right] \tag{2.8}$$

The unloading process, once the tangential force T reaches T^* (where a becomes a_* and c becomes c_*), is taken as the application of a new reversed sign tangential force, T'. According to equation (2.4), it is seen that reversed slip goes inward from boundary to

the center as *T'* increases. During the unloading process the tangential traction is given by (as shown in Figure 2.1(b))

$$\begin{aligned}
\tau &= -\frac{3fN}{2\pi a^3}(a^2-\rho^2)^{1/2}, b_u \le \rho \le a \\
\tau &= -\frac{3fN}{2\pi a^3}\left[(a^2-\rho^2)^{1/2} - 2(b_u^2-\rho^2)^{1/2}\right], c_* \le \rho \le b_u \\
\tau &= -\frac{3fN}{2\pi a^3}\left[(a^2-\rho^2)^{1/2} - 2(b_u^2-\rho^2)^{1/2} + (c_*^2-\rho^2)^{1/2}\right], \rho \le c_*
\end{aligned} \tag{2.9}$$

With the equilibrium condition,

$$T = \int_0^{2\pi}\int_0^a \tau\rho d\rho d\theta \tag{2.10}$$

where $T = T^* - T'$. Equation (2.10) leads to

$$T = \frac{fN}{a^3}(a^3-c^3) - \frac{2fN}{a^3}(a^3-b_u^3) \tag{2.11}$$

$$b_u = a\left(1-\frac{T'}{2fN}\right)^{1/3} \tag{2.12}$$

Therefore during the unloading process, the tangential displacement is given by

$$\begin{aligned}
\delta &= \frac{3(2-\nu)fN}{16\mu a}\left(2\frac{b_u^2}{a^2} - \frac{c_*^2}{a^2} - 1\right) \\
&= \frac{3(2-\nu)fN}{16\mu a}\left[2\left(1-\frac{T^*-T}{fN}\right)^{2/3} - \left(1-\frac{T^*}{fN}\right)^{2/3} - 1\right]
\end{aligned} \tag{2.13}$$

When b_u equals c_*, the loading is completely reversed and the tangential traction has the same magnitude as that at the end of original loading but with reversed sign. The subsequent reloading is symmetrical to the unloading with reversed sign.

2.3 Tangential traction under monotonic oblique loads with constant inclination

Based upon equation (2.4), any increment in tangential force will lead to slip beginning at the boundary if the normal force is kept constant. However, if the normal and the tangential forces are applied simultaneously, slip is not necessary. To illustrate this, an initial normal load is applied, followed by an oblique force. For the initial normal load, N_0, we have from equation (2.1)

$$a_0 = (KN_0R)^{1/3} \tag{2.14}$$

Let us now denote the ratio of the normal to tangential component of the oblique force increment as the oblique ratio, β, written as

$$\beta = \frac{dT}{dN} \tag{2.15}$$

Further, the incremental growth of the contact radius is given by differentiating equation (2.1), thus

$$3a^2da = RKdN = RKdT / \beta \tag{2.16}$$

If we assume a no-slip condition (friction coefficient, *f*, is infinite), we can make use of equation (2.4) to get the consequent increment in tangential traction

$$d\tau = \frac{dT}{2\pi a}(a^2 - \rho^2)^{-1/2} \tag{2.17}$$

Combining equations (2.16) and (2.17) and integrating with respect to, *a*, will give us the total tangential traction [64]

$$\tau(\rho) = \frac{3\beta}{2\pi RK}\int_{a_0}^{a_1} a(a^2-\rho^2)^{-1/2}da$$
$$= \frac{3\beta(N_0+N_1)}{2\pi a_1^3}\left[(a_1^2-\rho^2)^{1/2}-(a_0^2-\rho^2)^{1/2}\right], 0 \le \rho \le a_0 \qquad (2.18)$$
$$\tau(\rho) = \frac{3\beta}{2\pi RK}\int_{\rho}^{a_1} a(a^2-r^2)^{-1/2}da = \frac{3\beta(N_0+N_1)}{2\pi a_1^3}(a_1^2-r^2)^{1/2}, a_0 \le \rho \le a_1$$

Comparing equations (2.18) and (2.7) after the appropriate replacements have been made, it is seen that there is no slip only when oblique ratio β is less than *f*. If β is larger than *f*, equation (2.18) is not valid and the tangential traction are given by equation (2.5) where *N* is replaced by N_0+N_1. Tangential traction under arbitrarily oscillating oblique loads with constant inclination has been further elaborated using Preisach analysis [65].

2.4 Extension of Mindlin-Deresiewicz Continuous Approach

To extend the Mindlin-Deresiewicz analysis to contact problems with varying inclination of the oblique loads and complex initial tangential traction, we have developed a general procedure for obtaining tangential traction as the loading proceeds along a prescribed loading path. To this end we employ the basic solutions of the contact problem given by equations (2.5), (2.9) and (2.18). We note that the superposition of these basic solutions is also valid [66]. However, when we construct solutions for arbitrary loading paths by superposition of the basic solutions, Amonton's law should be satisfied. Therefore, to utilize the basic solution given by equation (2.18) for contacts subjected to oblique loading, we use a modified oblique ratio rather than the actual oblique ratio. The choice

of the modified oblique ratio depends upon the prior loading and is described below in rule 2(a). The use of modified oblique ratio means that only a part of tangential force is applied simultaneously with the normal force. The remainder part of the tangential force, if any, is applied subsequently, while keeping the normal forces constant. For the remainder part, equation (2.5) or (2.9) with an appropriate oblique ratio is applied to determine the tangential traction. The tangential tractions under different loading conditions and history are obtained by applying the following rules:

1) The tangential traction is recorded during all the loading history. For an arbitrary loading process, the initial tangential traction is taken as that at the end of the preceding loading path. The corresponding tangential force is denoted as T_0. For the first (virgin) loading, the initial tangential traction is zero.

2) The new tangential force in the current loading step is split into two parts, denoted by T_{n1} and T_{n2}, depending upon the oblique ratio β. At this loading stage, the total tangential force will be the sum of T_0, T_{n1} and T_{n2}. The subsequent determination of the tangential traction is accomplished by sequentially considering the following two sub-rules:

   a) Determination of the traction τ_1 due T_0 and T_{n1}. In this case, the first part of the new tangential force, denoted as T_{n1}, is applied simultaneously with the normal force. When the normal force is increasing, the tangential traction corresponding

to T_{n1} is given by equation (2.18) if the oblique ratio of the loading is less than f. If the oblique ratio is larger than f, the tangential traction corresponding to T_{n1} is given by equation (2.18) where β is replaced by f. The total tangential traction τ_1 at the contact is then obtained as the superposition of the tangential traction corresponding to T_{n1} and the initial traction corresponding to T_0. When the normal force is decreasing, the tangential traction corresponding to T_{n1} is given by equation (2.18) using the modified oblique ratio which is taken to be same as that at the end of the preceding loading path. This choice of the modified oblique ratio will ensure that the total tangential traction τ_1 in the lost area becomes zero.

b) Determination of the traction τ_2 due to T_{n2}. The second part of the new tangential force, denoted by, T_{n2}, if present, is applied while keeping the normal force constant. When the normal force is constant, a infinitesimal tangential force will result in the development of either the slip or the reversal slip annulus. If T_{n2} is positive, it indicates a loading process. The corresponding tangential traction τ_2 is obtained by applying equation (2.5) using an appropriate oblique ratio such that the superposition of the tangential traction τ_1 and τ_2 results in the development of slip that goes inward from the boundary. On the other hand, if T_{n2} is negative, it indicates an unloading process. The corresponding tangential traction is obtained by applying equation (2.9) using an appropriate oblique ratio such that the

superposition of the tangential traction τ_1 and τ_2 results in the development of reversed slip that goes inward from the boundary.

To illustrate the applicability of the above rules, we apply this procedure to two sets of loading cases: (1) when the contacting spheres are subjected to oblique forces whose inclination changes at different loading stages as shown by loading paths 1-2-3 and 1-2-4 in Figure 2.2, and (2) when the contacting spheres are subjected to cyclic loading as shown by loading paths 1-2-5-2 and 1-2-6-2 in Figure 2.2(a). We obtain the expressions for tangential tractions and force-displacement relationships at the various loading stages.

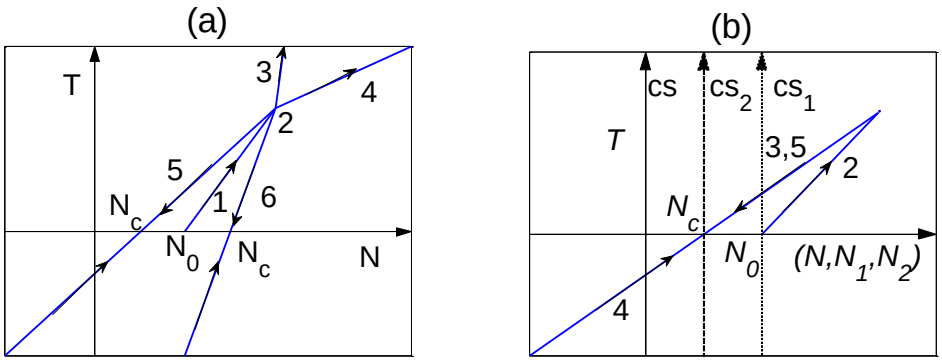

Figure 2.2: Sketch of loading path and coordinate systems.

2.5 Contact behavior under monotonic oblique force with varying inclinations

For simplicity and without loss of generality, we consider the loading paths 1-2-3 and 1-2-4 that consist of 3 steps including two oblique forces with different oblique ratios. We apply a force N_0 in normal direction in step 1, followed by oblique force $F_1(T_1,N_1)$, with oblique ratio β_1 in step 2, and oblique force $F_2(T_2,N_2)$, with oblique ratio β_2, in step 3.

The tangential traction for these loading paths depends on whether β_1 and β_2 are larger or less than contact friction coefficient f. For further discussion, we define the following notation

$$
\begin{aligned}
l_1 &= \frac{T_1}{fN_0}, l_1^* = \frac{T_1^*}{fN_0}, \theta_1 = \frac{f}{\beta_1} \\
l_2 &= \frac{T_2}{fN_0}, l_2^* = \frac{T_2^*}{fN_0}, \theta_2 = \frac{f}{\beta_2} \\
\lambda_m &= \frac{T_2}{T_1^*}
\end{aligned}
\tag{2.19}
$$

We note that the quantities with * refer to that at the end of load step 2 throughout the manuscript.

2.5.1 Monotonic loading with $\beta_1 > f$ and $\beta_2 > f$

The case when $\beta_1 > f$, the application of rule 2 of the general procedure requires that we split β_1 into f and $\beta_1 - f$, such that the tangential force is split into $N_1 f$ and $N_1(\beta_1 - f)$. In this case, the tangential traction is given as the sum of two parts τ_1 and τ_2, respectively. Traction τ_1 is given by rewriting equation (2.18) as follows.

$$
\begin{aligned}
\tau_1(\rho) &= \frac{3f(N_0 + N_1)}{2\pi a_1^3}\left[(a_1^2 - \rho^2)^{1/2} - (a_0^2 - \rho^2)^{1/2}\right], 0 \le r \le a_0 \\
\tau_1(\rho) &= \frac{3f(N_0 + N_1)}{2\pi a_1^3}(a_1^2 - r^2)^{1/2}, a_0 \le r \le a_1
\end{aligned}
\tag{2.20}
$$

We see from the expression for τ_1 that the traction in annulus a_1 to a_0 in under incipient slip. Therefore, any additional shear force, in this case given by $N_1(\beta_1 - f)$, will have to be

sustained by the stick part of the contact area, that is the circular area inside a_0. According to rule 2b, the expression for traction τ_2 is given by

$$\begin{aligned}\tau_2 &= \frac{3fN_0}{2\pi a_0^3}(a_0^2-\rho^2)^{1/2}, c \le \rho \le a \\ \tau_2 &= \frac{3fN_0}{2\pi a_0^3}\left[(a_0^2-\rho^2)^{1/2}-(c^2-\rho^2)^{1/2}\right], \rho \le c\end{aligned} \tag{2.21}$$

We can easily see that the superposition of tractions τ_1 and τ_2, will yield a tangential traction expression given by equation (2.5) where c is given by equation(2.6). The result is the same as the solution obtained by Mindlin and Deresiewicz (equation 61 of MD53) for this simple case. Thus, the tangential displacement for step 2 is obtained by rewriting equation (2.8) as follows:

$$\begin{aligned}\delta_1 &= \frac{3(2-\nu)f(N_0+N_1)}{16\mu a_1}(1-\frac{c^2}{a_1^2}) \\ &= \frac{3(2-\nu)fa_0^2}{16\mu KR}\left[(1+\theta_1 l_1)^{2/3}-(1+\theta_1 l_1-l_1)^{2/3}\right]\end{aligned} \tag{2.22}$$

And the tangential compliance is given as follows

$$c_1 = \frac{d\delta_1}{dT} = \frac{2-\nu}{8\mu a_1}(\theta_1+(1-\theta_1)(1-\frac{l_1}{1+\theta_1 l_1})^{-1/3}) \tag{2.23}$$

Similarly for load step 3, when $\beta_2 > f$, we split β_2 into f and $\beta_2 - f$, such that the tangential force is split into $T_1^* + N_2 f$ and $N_2(\beta_2 - f)$. Repeating the analysis described for load step 2, we find that the tangential traction is obtained to be same as equation (2.5) where the following expression for c is used:

$$c = a_2(1-\frac{T_1^* + T_2}{f(N_0 + N_1^* + N_2)})^{1/3} \tag{2.24}$$

The corresponding tangential displacement is given by

$$\begin{aligned}\delta_2 &= \frac{3(2-\nu) f(N_0 + N_1^* + N_2)}{16\mu a_2}(1-\frac{c^2}{a_2^2}) \\ &= \frac{3(2-\nu) f a_0^2}{16\mu KR}\left[(1+\theta_1 l_1^* + \theta_2 l_2)^{2/3} - (1+\theta_1 l_1^* + \theta_2 l_2 - l_1^* - l_2)^{2/3}\right]\end{aligned} \tag{2.25}$$

and the tangential compliance is given by

$$c_2 = \frac{d\delta_2}{dT} = \frac{2-\nu}{8\mu a_2}(\theta_2 + (1-\theta_2)(1-\frac{l_1^* + l_2}{1+\theta_1 l_1^* + \theta_2 l_2})^{-1/3}) \tag{2.26}$$

2.5.2 Monotonic loading with $\beta_1 < f$ and $\beta_2 < f$

Since $\beta_1 < f$, the application of rule 2(a) will yield the tangential traction expression in equation (2.18) as shown in Figure 2.3(a). The tangential displacement, in this case, is given by

$$\delta_1 = \frac{3(2-\nu)\beta_1(N_0 + N_1)}{16\mu a_1}(1-\frac{a_0^2}{a_1^2}) = \frac{3(2-\nu)\beta_1 a_0^2}{16\mu KR}((1+\theta_1 l_1)^{2/3} - 1) \tag{2.27}$$

Thus, the tangential compliance in this load interval is given by

$$c_1 = \frac{d\delta_l}{dT} = \frac{2-\nu}{8\mu a_1} \tag{2.28}$$

Further, in the loading step 3, since $\beta_2 < f$, only rule 2(a) is applicable. Thus, we obtain the tangential traction as follows

$$\tau(\rho)=\frac{3\beta_1(N_0+N_1^*)}{2\pi a_{1^*}^3}\left[(a_{1^*}^2-\rho^2)^{1/2}-(a_0^2-\rho^2)^{1/2}\right]$$
$$+\frac{3\beta_2(N_0+N_1^*+N_2)}{2\pi a_2^3}\left[(a_2^2-\rho^2)^{1/2}-(a_{1^*}^2-\rho^2)^{1/2}\right], 0\le\rho\le a_0$$
$$\tau(\rho)=\frac{3\beta_1(N_0+N_1^*)}{2\pi a_{1^*}^3}(a_{1^*}^2-\rho^2)^{1/2} \qquad (2.29)$$
$$+\frac{3\beta_2(N_0+N_1^*+N_2)}{2\pi a_2^3}\left[(a_2^2-\rho^2)^{1/2}-(a_{1^*}^2-\rho^2)^{1/2}\right], a_0\le\rho\le a_{1^*}$$
$$\tau(\rho)=\frac{3\beta_2(N_0+N_1^*+N_2)}{2\pi a_2^3}(a_2^2-\rho^2)^{1/2}, a_{1^*}\le\rho\le a_2$$

The tangential displacement in loading step 3 is also the sum of that due to F_1 and F_2,

$$\delta_2=\frac{3(2-\nu)\beta_1(N_0+N_1^*)}{16\mu a_{1^*}}(1-\frac{a_0^2}{a_{1^*}^2})+\frac{3(2-\nu)\beta_2(N_0+N_1^*+N_2)}{16\mu a_2}(1-\frac{a_{1^*}^2}{a_2^2})$$
$$=\frac{3(2-\nu)\beta_1 a_0^2}{16\mu KR}(\frac{1}{\theta_1}(1+\theta_1 l_1^*)^{2/3}-1)+\frac{1}{\theta_2}((1+\theta_1 l_1^*+\theta_2 l_2)^{2/3}-(1+\theta_1 l_1^*)^{2/3})) \qquad (2.30)$$

And the tangential compliance in this load interval (load step 3) is given by

$$c_2=\frac{d\delta_2}{dT}=\frac{2-\nu}{8\mu a_2} \qquad (2.31)$$

The tangential traction for this case is illustrated in Figure 2.3(b), which shows that the contact does not experience any slip during the loading as both β_1 and β_2 are less than f.

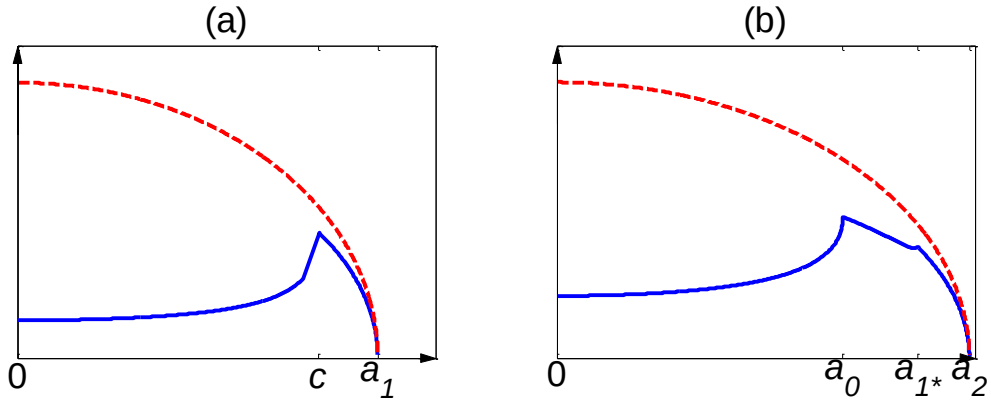

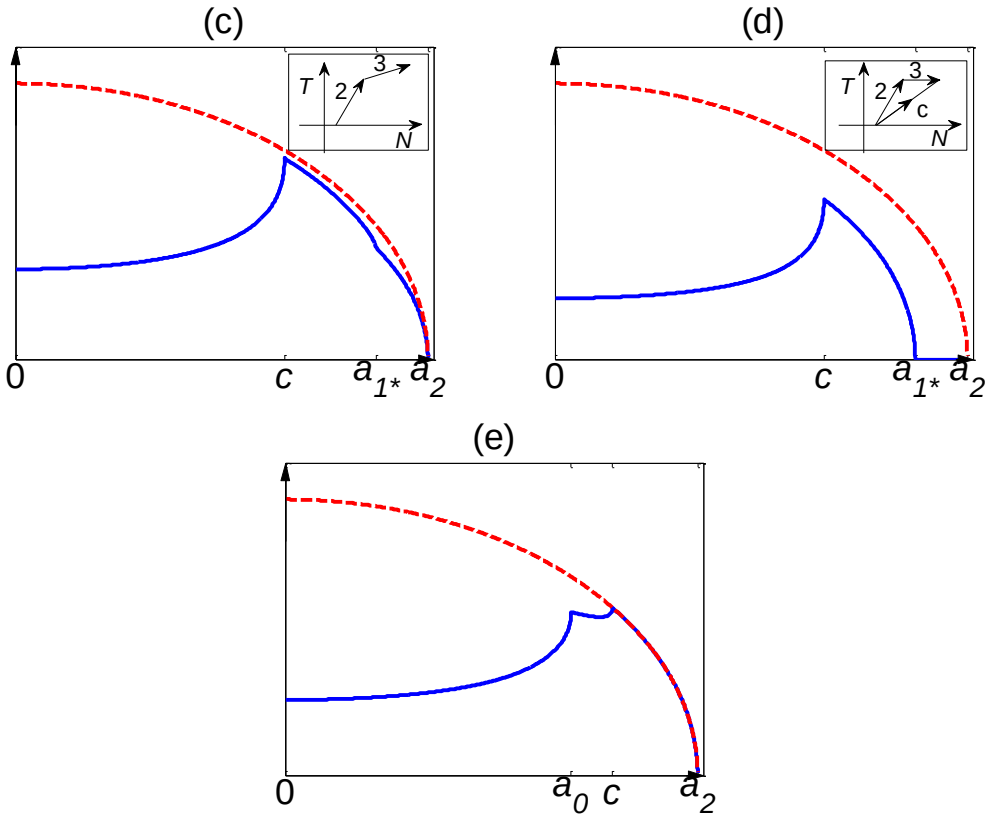

Figure 2.3: Tangential traction for monotonic loading given by the solid line where dashed line gives the slip limit.

2.5.3 Monotonic loading with $\beta_1 > f$ and $\beta_2 < f$

In this case, for the load step 2, the analysis is same as that in sub-section 'Monotonic loading with $\beta_1 > f$ and $\beta_2 > f$'. Consequently, the tangential traction, displacement and the compliance are given by equations (2.20), (2.22) and (2.23). In load step 3, since $\beta_2 < f$, only rule 2(a) is applicable and, therefore, the analysis is same as that for load step 3 in sub-section 'Monotonic loading with $\beta_1 < f$ and $\beta_2 < f$'. The tangential traction is obtained as follows:

$$\tau(\rho)=\frac{3f(N_0+N_1^*)}{2\pi a_{1^*}^3}\left[(a_{1^*}^2-\rho^2)^{1/2}-(c^2-\rho^2)^{1/2}\right]$$
$$+\frac{3\beta_2(N_0+N_1^*+N_2)}{2\pi a_2^3}\left[(a_2^2-\rho^2)^{1/2}-(a_{1^*}^2-\rho^2)^{1/2}\right], 0\le\rho\le c$$
$$\tau(\rho)=\frac{3f(N_0+N_1^*)}{2\pi a_{1^*}^3}(a_{1^*}^2-\rho^2)^{1/2} \qquad (2.32)$$
$$+\frac{3\beta_2(N_0+N_1^*+N_2)}{2\pi a_2^3}\left[(a_2^2-\rho^2)^{1/2}-(a_{1^*}^2-\rho^2)^{1/2}\right], c\le\rho\le a_{1^*}$$
$$\tau(\rho)=\frac{3\beta_2(N_0+N_1^*+N_2)}{2\pi a_2^3}(a_2^2-\rho^2)^{1/2}, a_{1^*}\le\rho\le a_2$$

The tangential traction for this case is shown in Figure 2.3(c), which shows that the contact does not experience any slip during the load step 3 since β_2 is less than f, although, as expected, the contact experiences slip in load step 2, since β_1 is greater than f. This arrest in slip is further illustrated in Figure 2.3(d) for $\beta_2=0$, wherein only the normal force is applied in load step 3. As the contact normal force increases, the contact radius will increase while the tangential traction will remain unchanged as we do not expect any tangential movement (Section 9 of MD53). Clearly, the tangential traction in this case is well below the slip limit; consequently, the slip from load step 2 is arrested. We note that if a different load path was follows as indicated by path C shown in Figure 2.3(c) inset, and the same force condition reached, a different result will be obtained, which will depend upon the oblique ratio β. For example, equation (2.5) will be applicable for $\beta>f$, and equation (2.18) will be used for $\beta<f$. This difference is a consequence of the strong load-history dependency of the contact behavior and is, generally not replicated by

plasticity models such as that in [34, 62]. The tangential displacement in load step 3 is given by

$$\begin{aligned}\delta &= \frac{3(2-\nu) f (N_0 + N_1^*)}{16\mu a_{1*}}(1-\frac{c^2}{a_{1*}^2}) + \frac{3(2-\nu)\beta_2 (N_0 + N_1^* + N_2)}{16\mu a_2}(1-\frac{a_{1*}^2}{a_2^2}) \\ &= \frac{3(2-\nu) f a_0^2}{16\mu KR}\left[(1-\frac{1}{\theta_1})(1+\theta_1 l_1^*)^{2/3} - (1+\theta_1 l_1^* - l_1^*)^{2/3} + \frac{1}{\theta_1}((1+\theta_1 l_1^* + \theta_2 l_2)^{2/3})\right]\end{aligned} \quad (2.33)$$

And the tangential compliance is found to be same as that in equation(2.31).

2.5.4 Monotonic loading with $\beta_1 < f$ and $\beta_2 \geq f$

In this case, for the load step 2, the result is the same as that in sub-section 'Monotonic loading with $\beta_1 < f$ and $\beta_2 < f$'. In load step 3, since $\beta_2 > f$, the application of rule 2 requires that we split β_2 into f and β_2-f, such that the tangential force is split into $T_1^* + N_2 f$ and $N_2(\beta_2 - f)$. In this case, the tangential traction is given as the sum of two parts τ_1 corresponding to force $T_1^* + N_2 f$ and τ_2 corresponding to force $N_2(\beta_2 - f)$, respectively. Traction τ_1 is given by equation (2.29) where β_2 is replaced by f. We see from the expression for τ_1 that the traction in annulus a_{1*} to a_2 is under incipient slip. Therefore, any additional shear force, in this case given by $N_2(\beta_2 - f)$, will have to be sustained by the stick part of the contact area, that is the circular area inside a_{1*} which is the contact radius at the end of load step 2. According to rule 2b, the expression for traction τ_2 is given by

$$\begin{aligned}\tau_2 &= \frac{3(f-\beta_1)(N_0 + N_1^*)}{2\pi a_{1*}^3}(a_{1*}^2 - \rho^2)^{1/2}, c \le \rho \le a_{1*} \\ \tau_2 &= \frac{3(f-\beta_1)(N_0 + N_1^*)}{2\pi a_{1*}^3}\left[(a_{1*}^2 - \rho^2)^{1/2} - (c^2 - \rho^2)^{1/2}\right], \rho \le c\end{aligned} \quad (2.34)$$

Where c is expressed as

$$c = a_{1^*}(1-\frac{T_2 - fN_2}{(f-\beta_1)(N_0+N_1^*)})^{1/3} \tag{2.35}$$

The total tangential traction is given as follows (shown in Figure 2.3(e))

$$\begin{aligned}
&\tau = \tau_1 + \tau_2 = \frac{3f(N_0+N_1^*+N_2)}{2\pi a_2^3}(a_2^2-\rho^2)^{1/2}, c \le \rho \le a_2 \\
&\tau = \tau_1 + \tau_2 = \frac{3f(N_0+N_1^*+N_2)}{2\pi a_2^3}\left[(a_2^2-\rho^2)^{1/2} - \frac{f-\beta_1}{f}(c^2-\rho^2)^{1/2}\right], a_0 \le \rho \le c \\
&\tau = \tau_1 + \tau_2 = \frac{3f(N_0+N_1^*+N_2)}{2\pi a_2^3}\left[(a_2^2-\rho^2)^{1/2} - \frac{\beta_1}{f}(a_0^2-\rho^2)^{1/2} - \frac{f-\beta_1}{f}(c^2-\rho^2)^{1/2}\right], \rho \le a_0
\end{aligned} \tag{2.36}$$

And the corresponding tangential displacement is given by

$$\begin{aligned}
\delta_2 &= \frac{3(2-\nu)f(N_0+N_1^*+N_2)}{16\mu a_2}(1-\frac{f-\beta_1}{f}\frac{c^2}{a_2^2}-\frac{\beta_1}{f}\frac{a_0^2}{a_2^2}) \\
&= \frac{3(2-\nu)fa_0^2}{16\mu KR}\left[(1+\theta_1 l_1^* + \theta_2 l_2)^{2/3} - (1-\frac{1}{\theta_1})(1+\theta_1 l_1^* + \theta_2 l_2 - l_2\frac{\theta_1-\theta_2}{\theta_1-1})^{2/3} - \frac{1}{\theta_1}\right]
\end{aligned} \tag{2.37}$$

The compliance is given by

$$c_2 = \frac{d\delta_2}{dT} = \frac{2-\nu}{8\mu a_2}(\theta_2 + (1-\theta_2)(1-\frac{l_2}{1+\theta_1 l_1^* + \theta_2 l_2}\frac{\theta_1-\theta_2}{\theta_1-1})^{-1/3}) \tag{2.38}$$

We note that as load step 3 progresses, the stick radius c will transition from greater than a_0 to less than a_0. When $c=a_0$, the tangential traction recovers back to equation (2.5) after N is replaced by $N_0+N_1^*+N_2$ and a by a_2. The shear displacement and the tangential compliance are the same as that in load step 3 of sub-section 'Monotonic loading with $\beta_1>f$ and $\beta_2>f$'. Furthermore, when $c=a_0$, we have

$$c = a_{1^*}(1-\frac{T_2 - fN_2}{(f-\beta_1)(N_0+N_1^*)})^{1/3} = a_0 = a_{1^*}(\frac{N_0}{N_0+N_1^*})^{1/3}$$
$$\Rightarrow \lambda_m = \frac{T_2}{T_1^*} = \frac{f(f-\beta_1)}{\beta_1(\beta_2 - f)} = \frac{\theta_2(\theta_1 - 1)}{1-\theta_2} \quad (2.39)$$

Thus, in load step 3, as the loading progresses to λ_m, the tangential traction expressed in equation (2.36) will recover back to equation (2.5). We also note that the contact does not experience slip in load step 2, since β_1 is less than f. However, as loading proceeds in step 3, slip penetrates first into a_0 and further towards the center of the contact area.

2.6 Cyclic behavior under multiple oblique forces

We now consider cyclic contact loading divided into 5 steps. In step 1, we apply N_0 in normal direction, followed by step 2 loading with oblique force F_1 (oblique ratio β_1), step 3 unloading with oblique force F_2 (oblique ratio β_2), step 4 reloading with oblique force F_2 (oblique ratio β_2), and step 5 unloading with oblique force F_2 (oblique ratio β_2) as illustrated by load paths 1-2-5-2 and 1-2-6-2 in Figure 2.2(a). Such contact loading is seen in multi-asperity contact models of rough surfaces subjected to cyclic shear under a constant normal load. Different combinations of β_1 and β_2 will be discussed in the subsequent discussion. For further discussion of these loading paths, we use the three coordinate systems shown in Figure 2.2(b), denoted by *cs*, cs_1 and cs_3, respectively. The coordinate system *cs* refers to *N*-*T* space, where *N* and *T* are total normal and tangential force, respectively. Coordinate systems cs_1 and cs_2 refer to N_1-*T* and N_2-*T* space, which are *N*-*T* spaces shifted by N_0 and N_c, respectively. The shifting forces N_0 and N_c

correspond to the original loading and unloading points when tangential force T is zero. Also for further derivations, we define the following notation

$$\begin{aligned} L_1 &= \frac{T}{fN_0}, L_1^* = \frac{T^*}{fN_0}, \theta_1 = \frac{f}{\beta_1} \\ L_2 &= \frac{T}{fN_c}, L_2^* = \frac{T^*}{fN_c}, \theta_2 = \frac{f}{\beta_2} \\ N_c &= N_0 + \frac{T^*}{\beta_1} - \frac{T^*}{\beta_2} \end{aligned} \tag{2.40}$$

And note that

$$\begin{aligned} \frac{a_0}{a_c} &= (\frac{N_0}{N_c})^{1/3} = (1 + \theta_2 L_2^* - \theta_1 L_2^*)^{1/3} \\ \frac{a_c}{a} &= (\frac{N_c}{N_c + N_2})^{1/3} = (\frac{1}{1 + \theta_2 L_2})^{1/3} \end{aligned} \tag{2.41}$$

2.6.1 Cyclic loading with $\beta_1 < f$, $\beta_2 < f$, and $\beta_1 > \beta_2$

For this case, in load step 2, the tangential traction is identical to that discussed in sub-section 'Monotonic loading with $\beta_1 < f$ and $\beta_2 < f$', such that the shear displacement and the tangential compliance are given by equations (2.27) and (2.28). The force-displacement relationship is given by curve OA in Figure 2.4(a) in this loading interval. In the subsequent load step 3 (load path 2-5 of Figure 2.2(a)), the tangential force at point (N,T) is $T^*-\beta_2(N_2^*-N_2)$. It is noted tangential force T^* and normal force N_2^* refer to the end of load step 2, which is same as the initial force for load step 3. According to rule 2, we split the applied tangential force into $T^*-\beta_1(N_2^*-N_2)$ and $(\beta_1-\beta_2)(N_2^*-N2)$. Thus, the tangential traction is obtained as the sum of two parts: τ_1 corresponding to force T^*-

$\beta_1(N_2^*-N_2)$, and τ_2 corresponding to force $(\beta_1-\beta_2)(N_2^*-N_2)$, respectively. Traction τ_1 is given by equation (2.18), where $N=N_c+N_2$ and $\beta=\beta_1$. Since tangential force $(\beta_1-\beta_2)(N_2^*-N_2)$ is larger than zero, it implies a loading process while keeping the normal force constant. According to rule 2b, τ_2, takes the following form

$$\begin{aligned}\tau_2 &= \frac{3(f-\beta_1)(N_c+N_2)}{2\pi a^3}(a^2-\rho^2)^{1/2}, c \le \rho \le a \\ \tau_2 &= \frac{3(f-\beta_1)(N_c+N_2)}{2\pi a^3}\left[(a^3-\rho^2)^{1/2}-(c^2-\rho^2)^{1/2}\right], \rho \le c\end{aligned} \tag{2.42}$$

Where c is given by

$$c = a\left(1-\frac{(T^*-T)(\beta_1-\beta_2)}{(f-\beta_1)\beta_2(N_c+N_2)}\right)^{1/3} \tag{2.43}$$

Thus the total traction can be expressed as (shown in Figure 2.3(e))

$$\begin{aligned}\tau &= \tau_1+\tau_2 = \frac{3f(N_c+N_2)}{2\pi a^3}(a^2-\rho^2)^{1/2}, c \le \rho \le a \\ \tau &= \tau_1+\tau_2 = \frac{3f(N_c+N_2)}{2\pi a^3}\left[(a^2-\rho^2)^{1/2}-\frac{f-\beta_1}{f}(c^2-\rho^2)^{1/2}\right], a_0 \le \rho \le c \\ \tau &= \tau_1+\tau_2 = \frac{3f(N_c+N_2)}{2\pi a^3}\left[(a^2-\rho^2)^{1/2}-\frac{\beta_1}{f}(a_0^2-\rho^2)^{1/2}-\frac{f-\beta_1}{f}(c^2-\rho^2)^{1/2}\right], a_0 \le \rho \le c\end{aligned} \tag{2.44}$$

For the tangential traction given above, the tangential displacement is given by

$$\delta_{u1} = \frac{3(2-\nu)f(N_0+N)}{16\mu a}\left(1-\frac{f-\beta_1}{f}\frac{c^2}{a^2}-\frac{\beta_1}{f}\frac{a_0^2}{a^2}\right) \tag{2.45}$$

With the help of equations (2.40), (2.41) and (2.43), equation (2.45) is rewritten as

$$\delta_{u1} = \frac{3(2-\nu)fa_c^2}{16\mu KR}\left[(1+\theta_2 L_2)^{2/3}\left(1-\left(1-\frac{1}{\theta_1}\right)\left(1-\frac{L_2^*-L_2}{1+\theta_2 L_2}\frac{\theta_2-\theta_1}{\theta_1-1}\right)^{2/3}-\frac{1}{\theta_1}(1+L_2^*\theta_2-L_2^*\theta_1)^{2/3}\right]\right.$$

(2.46)

The tangential compliance in this unloading interval (first part of load step 3 given by curve AB in Figure 2.4(a)) is given by

$$c_{u1} = \frac{d\delta_{u1}}{dT} = \frac{2-\nu}{8\mu a}(\theta_2 - (\theta_2 - 1)(1 - \frac{\theta_2 - \theta_1}{\theta_1 - 1}\frac{L_2^* - L_2}{1 + \theta_2 L_2})^{-1/3}) \qquad (2.47)$$

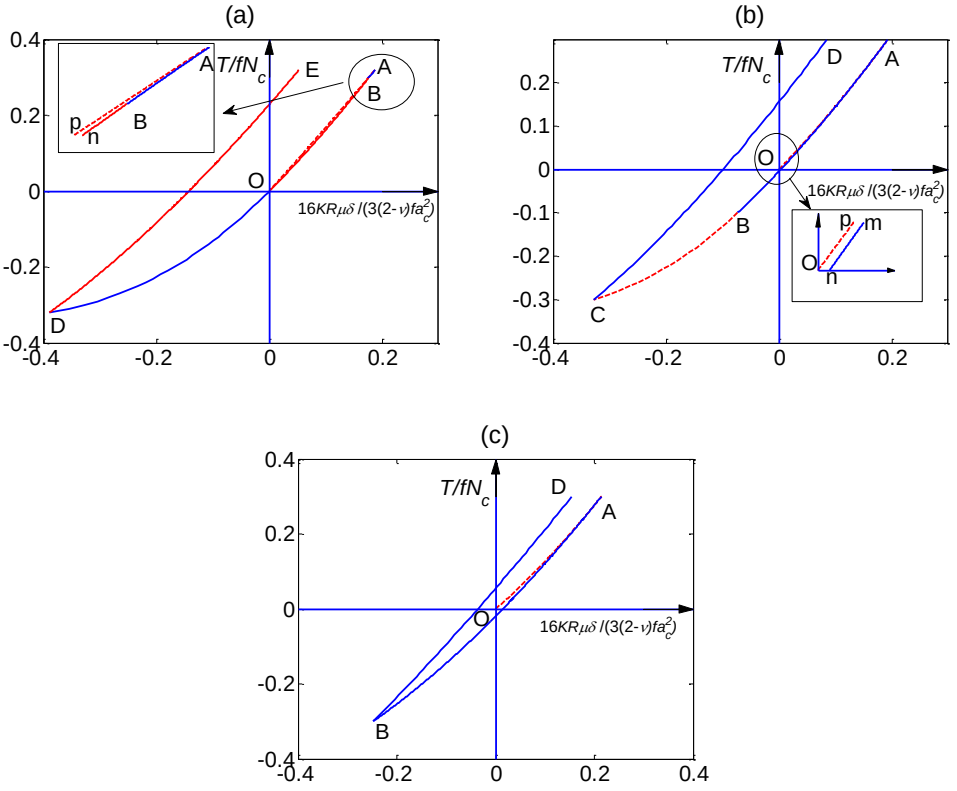

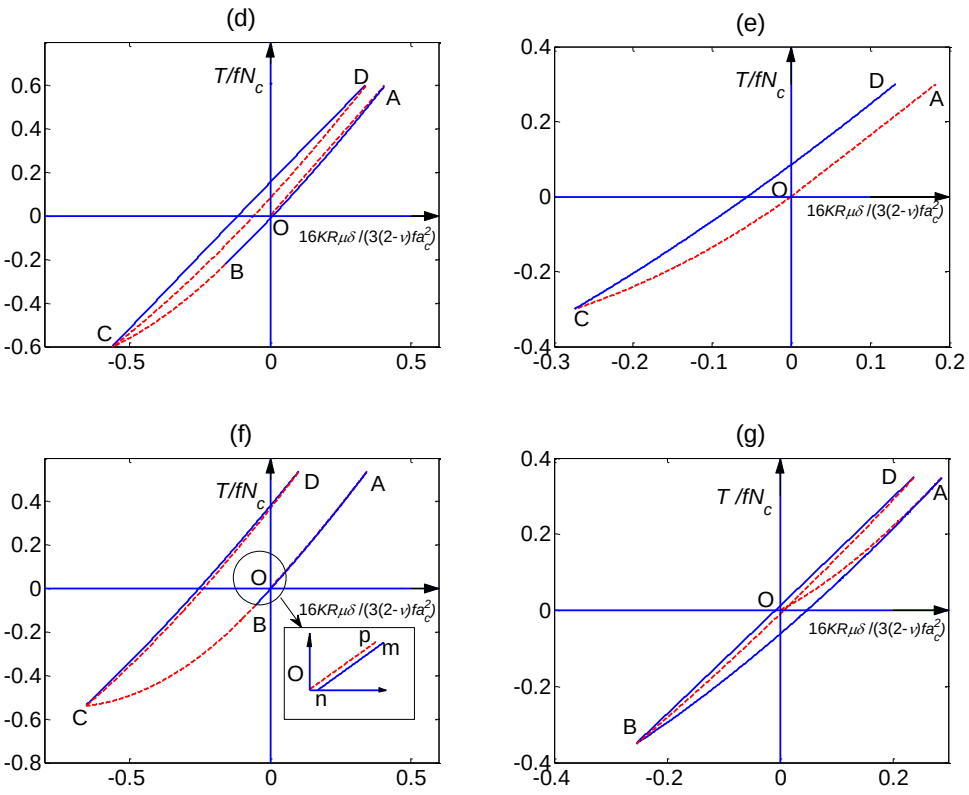

Figure 2.4: Force-displacement relationships for cyclic loading.

As the unloading progresses, it is noted that c approaches a_0. When c becomes equal to a_0, equation (2.44) reduces to equation (2.5), where c is given by equation (2.6) after N is replaced by N_1+N_0. Furthermore, at $a_0=c$, we have

$$\begin{aligned} c = a(1-\frac{T}{f(N_c+N_2)})^{1/3} = a_0 = a(\frac{N_0}{N_c+N_2})^{1/3} \\ \Rightarrow \frac{T}{T^*} = \frac{f(\beta_1-\beta_2)}{\beta_1(f-\beta_2)} = \frac{\theta_2-\theta_1}{\theta_2-1} \end{aligned} \tag{2.48}$$

As we continue unloading and reach $T=0$ (second part of load step 3 given by curve BO in Figure 2.4(a)), contact radius $a=c$, and the tangential traction will become zero.

During this unloading process, the tangential displacement is given by rewriting equation (2.8) as follows

$$\delta_{u2} = \frac{3(2-\nu) f (N_c + N_2)}{16\mu a}(1-\frac{c^2}{a^2}) = \frac{3(2-\nu) f a_c^2}{16\mu KR}\left[(1+\theta_2 L_2)^{2/3} - (1+\theta_2 L_2 - L_2)^{2/3}\right] \quad (2.49)$$

The tangential compliance in this unloading interval (second part of load step 3) is given by

$$c_{u2} = \frac{d\delta_{u2}}{dT} = \frac{2-\nu}{8\mu a}(\theta_2 + (1-\theta_2)(1-\frac{L_2}{1+\theta_2 L_2})^{-1/3}) \quad (2.50)$$

Further unloading (from $T=0$) will result in increasing T in the opposite direction while N_2 is decreasing. During this part of unloading (given by curve OD in Figure 2.4(a)), slip annulus will develop and the tangential traction will be given by equation (2.5) with sign reversed and N replaced by N_c+N_2. In this load interval, c is given by

$$c = a(1-\frac{|T|}{f(N_c + N_2)})^{1/3} \quad (2.51)$$

Thus the tangential displacement can be written by equation (2.8) with sign reversed

$$\delta_{u3} = -\frac{3(2-\nu) f (N_c + N_2)}{16\mu a}(1-\frac{c^2}{a^2}) = \frac{3(2-\nu) f a_c^2}{16\mu KR}\left[-(1+\theta_2 L_2)^{2/3} + (1+\theta_2 L_2 + L_2)^{2/3}\right]$$

(2.52)

The tangential compliance is given by

$$c_{u3} = \frac{d\delta_{u3}}{dT} = \frac{2-\nu}{8\mu a}(-\theta_2 + (1+\theta_2)(1+\frac{L_2}{1+\theta_2 L_2})^{-1/3}) \quad (2.53)$$

When T reaches $-T^*$, we begin to reload with oblique ratio β_2 (load step 4 given by curve DE in Figure 2.4(a)). In this loading interval, the tangential force at a point (N,T) is $\beta_2(N_2-N_2^*) - T^*$. Since β_2 is less than f no slip annulus will develop at the boundary. Superposing the traction due to force $\beta_2(N_2-N_2^*)$ and $-T^*$, we obtain the total traction, shown in Figure 2.5(a), as:

$$\tau = \frac{3\beta_2(N_c+N_2)}{2\pi a^3}(a^2-\rho^2)^{1/2}, b_r \le \rho \le a$$
$$\tau = \frac{3\beta_2(N_c+N_2)}{2\pi a^3}\left[(a^2-\rho^2)^{1/2} - (1+\frac{f}{\beta_2})(b_r^2-\rho^2)^{1/2}\right], c_{-*} \le \rho \le b_r \qquad (2.54)$$
$$\tau = \frac{3\beta_2(N_c+N_2)}{2\pi a^3}\left[(a^2-\rho^2)^{1/2} - (1+\frac{f}{\beta_2})(b_r^2-\rho^2)^{1/2} + \frac{f}{\beta_2}(c_{-*}^2-\rho^2)^{1/2}\right], \rho \le c_{-*}$$

Where c_{-*} is given by equation (2.51) after T and N_2 are replaced by $-T^*$ and $-N_2^*$, respectively, and b_r is given by

$$b_r = a(1-\frac{f(N_2+N_2^*)+T+T^*}{(f+\beta_2)(N_c+N_2)})^{1/3} \qquad (2.55)$$

The tangential displacement in this load interval (load step 4) up to the T^* is given by

$$\delta_r = \frac{3(2-\nu)\beta_2 a_c^2}{16\mu KR}\left[(1+\theta_2 L_2)^{2/3}(1-(1+\theta_2)(\frac{1-L_2^*\theta_2}{1+\theta_2 L_2})^{2/3}) - \theta_2(1-\theta_2 L_2^* - L_2^*)^{2/3}\right] \qquad (2.56)$$

The tangential compliance is given by equation (2.28) and the corresponding

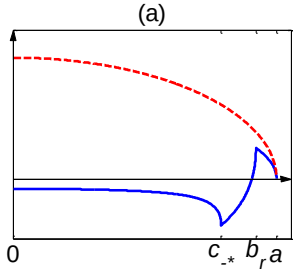

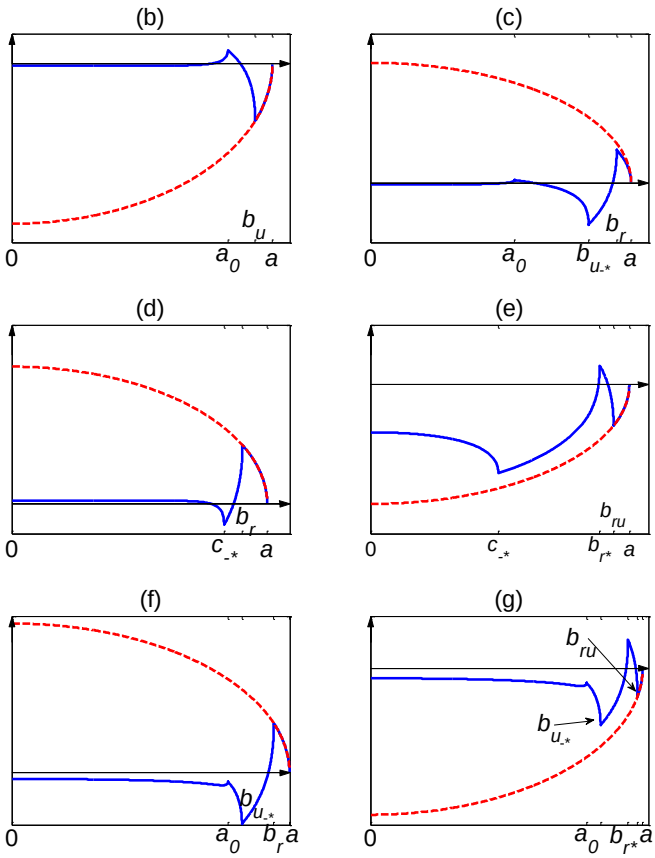

Figure 2.5: Tangential traction for cyclic loading given by the solid line where dashed line gives the slip limit.

force-displacement relationship is given by curve DE in Figure 2.4(a). As we unload again from T^* with oblique ratio β_2 (load step 5), the results will be identical to that obtained for the reloading (load step 4). Further reloading-unloading will yield the same result as the first reload-unload cycle.

2.6.2 Cyclic loading with $\beta_1 < f$, $\beta_2 < f$, and $\beta_1 < \beta_2$

For this combination of β_1 and β_2, the result is exactly the same as that in sub-section 'Cyclic loading with $\beta_1<f$, $\beta_2<f$, and $\beta_1>\beta_2$' in the loading process (load step 2). The force-displacement relationship is given by curve OA in Figure 2.4(b) in this loading interval. In the subsequent load step 3 (load path 2-6), the tangential force at point (N,T) is $T^*-\beta_2(N_2^*-N_2)$. According to rule 2, this force is split into $T^*-\beta 1(N2^*-N2)$ and $(\beta_1-\beta_2)(N_2^*-N_2)$. Again, the tangential traction is obtained as the sum of these two parts τ_1 corresponding to force $T^*-\beta_1(N_2^*-N_2)$ and τ_2 corresponding to force $(\beta_1-\beta_2)(N_2^*-N_2)$, respectively. Traction τ_1 is given by equation (2.18), where $N=N_c+N_2$ and $\beta=\beta_1$. Since $(\beta_1-\beta_2)$ less than zero, it implies an unloading while the normal force is constant. Thus the traction for τ_2 is given as follows in order to satisfy the requirement of uniform displacement in the stick region:

$$\begin{aligned}\tau_2 &= -\frac{3(f+\beta_1)N}{2\pi a^3}(a^2-\rho^2)^{1/2}, b_u \le \rho \le a \\ \tau_2 &= -\frac{3(f+\beta_1)N}{2\pi a^3}\left[(a^2-\rho^2)^{1/2}-(b_u^2-\rho^2)^{1/2}\right], \rho \le b_u\end{aligned} \tag{2.57}$$

From the equilibrium condition equation (2.10), b_u is given by

$$b_u = a\left(1-\frac{(T^*-T)(\beta_2-\beta_1)}{(f+\beta_1)\beta_2(N_c+N_2)}\right)^{1/3} \tag{2.58}$$

By superposing of τ_1 and τ_2, at the point (N,T) of the unloading path 2-6 in Figure 2.2(a), the tangential traction is given by (as shown in Figure 2.5(b))

$$\tau = -\frac{3f(N_c+N_2)}{2\pi a^3}(a^2-\rho^2)^{1/2}, b_u \le \rho \le a$$
$$\tau = -\frac{3f(N_c+N_2)}{2\pi a^3}\left[(a^2-\rho^2)^{1/2}-(1+\frac{\beta_1}{f})(b_u^2-\rho^2)^{1/2}\right], a_0 \le \rho \le b_u \qquad (2.59)$$
$$\tau = -\frac{3f(N_c+N_2)}{2\pi a^3}\left[(a^2-\rho^2)^{1/2}-(1+\frac{\beta_1}{f})(b_u^2-\rho^2)^{1/2}+\frac{\beta_1}{f}(a_0^2-\rho^2)^{1/2}\right], \rho \le a_0$$

With the help of equations (2.40), (2.41) and (2.43), the shear displacement(as shown in curve AB in Figure 2.4(b) and Figure 2.4(c)) is obtained as

$$\delta_{u1} = \frac{3(2-\nu)fa_c^2}{16\mu KR}\left[(1+\theta_2 L_2)^{2/3}((1+\frac{1}{\theta_1})(1-\frac{L_2^*-L_2}{1+\theta_2 L_2}\frac{\theta_1-\theta_2}{\theta_1+1})^{2/3}-1)-\frac{1}{\theta_1}(1+L_2^*\theta_2-L_2^*\theta_1)^{2/3}\right]$$

(2.60)

And the tangential compliance in this loading interval (load step 3) is given by

$$c_{u1} = \frac{d\delta_{u1}}{dT} = \frac{2-\nu}{8\mu a}(-\theta_2+(1+\theta_2)(1-\frac{\theta_1-\theta_2}{\theta_1+1}\frac{L_2^*-L_2}{1+\theta_2 L_2})^{-1/3}) \qquad (2.61)$$

When $b_u \le a_0$, equation (2.59) recovers to equation (2.5) but with sign reversed and c is given by equation (2.6), after N is replaced by N_0+N. However, as the loading progresses, b_u approaches a_0 .When $b_u=a_0$, we have

$$b_u = a(1-\frac{(T^*-T)(\beta_2-\beta_1)}{(f+\beta_1)\beta_2(N_c+N_2)})^{1/3} = a_0 = a(\frac{N_0}{N_c+N_2})^{1/3}$$
$$\Rightarrow \frac{T}{T^*} = \frac{f(\beta_1-\beta_2)}{\beta_1(f+\beta_2)} = \frac{\theta_2-\theta_1}{\theta_2+1} \qquad (2.62)$$

Further unloading will result in increasing T in the opposite direction while N is decreasing. Under this part of unloading, given by the curve BC in Figure 2.4(b), slip annulus will develop and the tangential traction will be given by equation (2.5) with sign

reversed until T=-T*. The tangential displacement in this load interval is given by equation (2.52).

In load step 4, as the tangential force is reversed into the reloading path, the initial traction will be determined by the final condition of load step 3. If $b_u \le a_0$, the initial traction is given by equation (2.5). In this case, the reloading and, further unloading steps can be treated in the same manner as sub-section 'Cyclic loading with $\beta_1 < f$, $\beta_2 < f$, and $\beta_1 > \beta_2$', as shown by curve CD and DC in Figure 2.4(b). However, if $b_u > a_0$ at the point T=-T*, the initial traction in the loading step 4 is given by equation (2.59). In this reloading step, given by the curve BD in Figure 2.4(c), the tangential force at point (N,T) is $\beta_2(N_2-N_2^*) - T^*$. Since β_2 is less than f no slip annulus will develop at the boundary. Superposing the traction due to tangential forces $\beta_2(N_2-N_2^*)$ and $-T^*$, the total traction is obtained as (shown in Figure 2.5(c)):

$$
\begin{aligned}
&\tau = \frac{3\beta_2(N_c+N_2)}{2\pi a^3}(a^2-\rho^2)^{1/2}, b_r \le \rho \le a \\
&\tau = \frac{3\beta_2(N_c+N_2)}{2\pi a^3}\left[(a^2-\rho^2)^{1/2} - (\frac{f+\beta_2}{\beta_2})(b_r^2-\rho^2)^{1/2}\right], b_{u-*} \le \rho \le b_r \\
&\tau = \frac{3\beta_2(N_c+N_2)}{2\pi a^3}\left[(a^2-\rho^2)^{1/2} - (\frac{f+\beta_2}{\beta_2})(b_r^2-\rho^2)^{1/2} + (\frac{f+\beta_1}{\beta_2})(b_{u-*}^2-\rho^2)^{1/2}\right], a_0 \le \rho \le b_{u-*} \\
&\tau = \frac{3\beta_2(N_c+N_2)}{2\pi a^3}\left[(a^2-\rho^2)^{1/2} - (\frac{f+\beta_2}{\beta_2})(b_r^2-\rho^2)^{1/2} + (\frac{f+\beta_1}{\beta_2})(b_{u-*}^2-\rho^2)^{1/2} - \frac{\beta_1}{\beta_2}(a_0^2-\rho^2)^{1/2}\right], \rho \le a_0
\end{aligned}
\qquad (2.63)
$$

From the equilibrium condition, b_r is given by

$$b_r = a\left(1 - \frac{f(N_2+N_2^*)+T+T^*}{(f+\beta_2)(N_c+N_2)}\right)^{1/3} \qquad (2.64)$$

Thus the tangential displacement is given by

$$\delta_r = \frac{3(2-\nu) f a_c^2}{16\mu KR}\frac{a^2}{a_c^2}\left(\frac{1}{\theta_2}-\frac{1}{\theta_2}\frac{b_r^2}{a^2}+\left(1+\frac{\beta_1}{f}\right)\frac{b_{u-*}^2}{a^2}-\frac{\beta_1}{f}\frac{a_0^2}{a^2}\right) \tag{2.65}$$

$$= \frac{3(2-\nu) f a_c^2}{16\mu KR}\left\{\frac{1}{\theta_2}\left[(1+\theta_2 L_2)^{2/3}-(1+\theta_2)(1-\theta_2 L_2^*)^{2/3}\right]+\left(1+\frac{1}{\theta_1}\right)\left(1-\theta_2 L_2^*-\frac{2(\theta_1-\theta_2)}{(\theta_1+1)}L_2^*\right)^{2/3}-\frac{1}{\theta_1}(1+\theta_2 L_2^*-\theta_1 L_2^*)^{2/3}\right\}$$

And the tangential compliance is given by equation (2.28). Further reloading-unloading will yield the same result as the first reload-unload cycle shown by the curve BD in Figure 2.4(c).

2.6.3 Cyclic loading with $\beta_1, \beta_2 > f$

For this combination of β_1 and β_2, the load step 2 is similar to load step 2 of sub-section 'Monotonic loading with $\beta_1 > f$ and $\beta_2 > f$'. The force-displacement relationship is given by curve OA in Figure 2.4(d) in this loading interval. In the subsequent load step 3 (load path 2-5 or 2-6), the tangential force at point (N,T) is $T^*-\beta_2(N_2^*-N_2)$. According to rule 2, this force is split into $T^*-f(N_2^*-N_2)$ and $(f-\beta_2)(N_2^*-N_2)$. Again, the tangential traction is obtained as the sum of these two parts τ_1 corresponding to force $T^*-f(N_2^*-N_2)$ and τ_2 corresponding to force $(f-\beta_2)(N_2^*-N_2)$, respectively. Traction τ_1 is given by equation(2.18), where $N=N_c+N_2$, $\beta=f$ and $a_0=c_*$. Since $(f-\beta 2)$ is less than zero, it implies an unloading while the normal force is constant. Thus the traction for τ_2 is given as follows according to rule 2b:

$$\tau_2 = -\frac{3(f+f)N}{2\pi a^3}(a^2-\rho^2)^{1/2}, b_u \le \rho \le a$$
$$\tau_2 = -\frac{3(f+f)N}{2\pi a^3}\left[(a^2-\rho^2)^{1/2}-(b_u^2-\rho^2)^{1/2}\right], \rho \le b_u \tag{2.66}$$

From the equilibrium condition, b_u is given by

$$b_u = a(1-\frac{(T^*-T)(\beta_2-f)}{2f\beta_2(N_c+N_2)})^{1/3} \tag{2.67}$$

By superposing of τ_1 and τ_2, at the point (N,T) of the unloading path 2-5 or 2-6 in Figure 2.2(a), the tangential traction is given by equation (2.9) after N is replaced by N_c+N_2. Thus the tangential displacement is given by

$$\delta_{u1} = \frac{3(2-\nu)fa_c^2}{16\mu KR}\frac{a^2}{a_c^2}(2\frac{b_u^2}{a^2}-1-\frac{c_*^2}{a^2})$$
$$= \frac{3(2-\nu)fa_c^2}{16\mu KR}\{2\left[1+\frac{\theta_2}{2}(L_2^*+L_2)-\frac{L_2^*-L_2}{2}\right]^{2/3}-(1+\theta L_2)^{2/3}-(1+\theta_2 L_2^*-L_2^*)^{2/3}\} \tag{2.68}$$

And the tangential compliance in this loading interval (load step 3) is given by

$$c_{u1} = \frac{d\delta_{u1}}{dT} = \frac{2-\nu}{8\mu a}(-\theta_2+(1+\theta_2)(1-(1-\theta_2)\frac{L_2^*-L_2}{2(1+\theta_2 L_2)})^{-1/3}) \tag{2.69}$$

The force-displacement relationship is given by curve AB in Figure 2.4(d) in this loading interval. It is noted that during this process, c_* is not changing while b_u is increasing. When b_u is equal to c_* ,we have

$$b_u = \frac{a}{a_*}a_*(1-\frac{(T^*-T)(\beta_2-f)}{2f\beta_2(N_c+N_2)})^{1/3} = c_* = a_*(1-\frac{T^*}{f(N_c+N_2^*)})^{1/3}$$
$$\Rightarrow \frac{T}{T^*} = \frac{f-\beta_2}{f+\beta_2} = \frac{\theta_2-1}{\theta_2+1} \tag{2.70}$$

In addition, the tangential traction recovers to equation (2.5) with sign reversed. Upon further unloading, since N is decreasing while absolute value of T is increasing, slip is always present and the tangential traction will be the same as equation (2.5) with sign reversed. In this case, c is given by

$$c = a(1-\frac{|T|}{f(N_c+N_2)})^{1/3} \tag{2.71}$$

Thus the tangential displacement can be written from equation (2.8) with sign reversed

$$\delta_{u2} = -\frac{3(2-\nu)f(N_c+N_2)}{16\mu a}(1-\frac{c^2}{a^2}) = \frac{3(2-\nu)fa_c^2}{16\mu KR}\left[-(1+\theta_2 L_2)^{2/3}+(1+\theta_2 L_2+L_2)^{2/3}\right] \tag{2.72}$$

And the tangential compliance is given by

$$c_{u2} = \frac{d\delta_{u2}}{dT} = \frac{2-\nu}{8\mu a}(-\theta_2+(1+\theta_2)(1+\frac{L_2}{1+\theta_2 L_2})^{-1/3}) \tag{2.73}$$

The force-displacement relationship is given by curve BC in Figure 2.4(d) in this loading interval. Beginning at $T=-T^*$(where c became c_{-*}), we reload the contact (load step 4) and the traction will be given by equation (2.9) after appropriate change (shown in Figure 2.5(d))

$$\begin{aligned}
\tau &= \frac{3f(N_c+N_2)}{2\pi a^3}(a^2-\rho^2)^{1/2}, b_r \le \rho \le a \\
\tau &= \frac{3f(N_c+N_2)}{2\pi a^3}\left[(a^2-\rho^2)^{1/2}-2(b_r^2-\rho^2)^{1/2}\right], c_{-*} \le \rho \le b_r \\
\tau &= \frac{3f(N_c+N_2)}{2\pi a^3}\left[(a^2-\rho^2)^{1/2}-2(b_r^2-\rho^2)^{1/2}+(c_{-*}^2-\rho^2)^{1/2}\right], \rho \le c_{-*}
\end{aligned} \tag{2.74}$$

where c_{-*} is given by equation (2.71) after substitution $T=-T^*$ and $N_2=N_2^{-*}$, and b_r is given by

$$b_r = a(1-\frac{f(N_2+N_2^*)+T+T^*}{2f(N_c+N_2)})^{1/3} \tag{2.75}$$

The tangential displacement in this load interval, as shown by the curve CD (upper curve) in Figure 2.4(d), is given by

$$\begin{aligned}\delta_r &= \frac{3(2-\nu)fa_c^2}{16\mu KR}\frac{a^2}{a_c^2}(1-2\frac{b_r^2}{a^2}+\frac{c_{-*}^2}{a^2}) \\ &= \frac{3(2-\nu)fa_c^2}{16\mu KR}\{(1+\theta L_2)^{2/3}-2\left[1-\frac{\theta_2}{2}(L_2^*-L_2)-\frac{L_2^*+L_2}{2}\right]^{2/3}+(1-\theta_2 L_2^*-L_2^*)^{2/3}\}\end{aligned} \tag{2.76}$$

And the tangential compliance is given by

$$c_r = \frac{d\delta_r}{dT} = \frac{2-\nu}{8\mu a}(\theta_2+(1-\theta_2)(1-(1+\theta_2)\frac{L_2^*+L_2}{2(1+\theta_2 L_2)})^{-1/3}) \tag{2.77}$$

As we unload again from T^* (load step 5), both the normal force N and the tangential force T will be decreasing. According to rule 2, the tangential traction is given by (shown in Figure 2.5(e))

$$\begin{aligned}\tau &= -\frac{3f(N_c+N_2)}{2\pi a^3}(a^2-\rho^2)^{1/2}, b_{ru}\le\rho\le a \\ \tau &= -\frac{3f(N_c+N_2)}{2\pi a^3}\left[(a^2-\rho^2)^{1/2}-2(b_{ru}^2-\rho^2)^{1/2}\right], b_{r*}\le\rho\le b_{ru} \\ \tau &= -\frac{3f(N_c+N_2)}{2\pi a^3}\left[(a^2-\rho^2)^{1/2}-2(b_{ru}^2-\rho^2)^{1/2}+2(b_{r*}^2-\rho^2)^{1/2}\right], c_{-*}\le\rho\le b_{r*} \\ \tau &= -\frac{3f(N_c+N_2)}{2\pi a^3}\left[(a^2-\rho^2)^{1/2}-2(b_{ru}^2-\rho^2)^{1/2}+2(b_{r*}^2-\rho^2)^{1/2}-(c_{-*}^2-\rho^2)^{1/2}\right], \rho\le c_{-*}\end{aligned}$$

(2.78)

Where b_{r*} is given by equation (2.75) after N_2 and T are replaced by N_2* and T*, respectively, and b_{ru} is given by

$$b_{ru} = a(1-\frac{(T*-T)(\beta_2 - f)}{2f\beta_2(N_c + N_2)})^{1/3} \tag{2.79}$$

Therefore the tangential displacement, as given by the curve DC (lower curve) in Figure 2.4(d), is given by

$$\delta_{ru} = \frac{3(2-\nu) f a_c^2}{16\mu KR}\frac{a^2}{a_c^2}(2\frac{b_{ru}^2}{a^2} + \frac{c_{-*}^2}{a^2} - 2\frac{b_{r*}^2}{a^2} - 1)$$
$$= \frac{3(2-\nu) f a_c^2}{16\mu KR}\{2\left[1+\frac{\theta_2}{2}(L_2^* + L_2) - \frac{L_2^* - L_2}{2}\right]^{2/3} + (1-\theta_2 L_2^* - L_2^*)^{2/3} - 2(1-L_2^*)^{2/3} - (1+\theta_2 L_2)^{2/3}\}$$

(2.80)

And the tangential compliance is given by

$$c_{ru} = \frac{d\delta_{ru}}{dT} = \frac{2-\nu}{8\mu a}(-\theta_2 + (1+\theta_2)(1-(1-\theta_2)\frac{L_2^* - L_2}{2(1+\theta_2 L_2)})^{-1/3}) \tag{2.81}$$

At the point T=-T*, b_{ru} = b_{r*} and equation (2.78) recovers to equation (2.5) but with sign reversed. Further reloading and unloading steps can be treated in the same manner as described above. We note in this case that there is a dissipation of energy as the contact undergoes unload-reload cycles.

2.6.4 Cyclic loading with $\beta_1 > f$, $\beta_2 < f$

For this case of β_1, the load step 2 is similar to load step 2 of sub-section 'Monotonic loading with $\beta_1 > f$ and $\beta_2 > f$'. The force-displacement relationship is given by curve OA in

Figure 2.4(e) in this loading interval. In load step 3, the results are identical to the second part of load step 3 described in sub-section 'Cyclic loading with $\beta_1<f$, $\beta_2<f$, and $\beta_1>\beta_2$' till $T=0$, as shown by curve AO in Figure 2.4(e). Upon further unloading, T increases in the opposite direction while N is decreasing, and the results are same as the third part of load step 3 described in sub-section 'Cyclic loading with $\beta_1<f$, $\beta_2<f$, and $\beta_1>\beta_2$', as shown by curve OC in Figure 2.4(e). The reloading step (load step 4) and further unloading is same as that discussed in sub-section 'Cyclic loading with $\beta_1<f$, $\beta_2<f$, and $\beta_1>\beta_2$' since β_2 less than f which is given by the curve CD in Figure 2.4(e).

2.6.5 Cyclic loading with $\beta_1<f$, $\beta_2>f$

For this case, in load step 2, the tangential traction is identical to that discussed in sub-section 'Monotonic loading with $\beta_1<f$ and $\beta_2<f$'. The force-displacement relationship is given by curves OA in Figure 2.4(f) and Figure 2.4(g) in this loading interval. Since β_1 is less than β_2, thus the unloading (load step 3) is similar to sub-section 'Cyclic loading with $\beta_1<f$, $\beta_2<f$, and $\beta_1<\beta_2$', as given by curves AB in Figure 2.4(f) and Figure 2.4(g), respectively. In load step 4, as the tangential force is reversed into the reloading path, the initial traction will be determined by the final condition of load step 3. If $b_u \leq a_0$, the initial traction is given by equation (2.5). In this case, the further unloading, reloading and, further unloading steps can be treated in the same manner as sub-section 'Cyclic loading with $\beta_1>f$, $\beta_2>f$', as given by curve BC, CD (upper curve) and DC (lower curve)

Figure 2.4(f). However, if $b_u > a_0$ at the point $T=-T^*$, the initial traction in the loading step 4 is given by equation (2.59). According to rule 2, the reloading tangential traction is given by (shown in Figure 2.5(f))

$$\tau = \frac{3f(N_c+N_2)}{2\pi a^3}(a^2-\rho^2)^{1/2}, b_r \le \rho \le a$$
$$\tau = \frac{3f(N_c+N_2)}{2\pi a^3}\left[(a^2-\rho^2)^{1/2}-2(b_r^2-\rho^2)^{1/2}\right], b_{u\_*} \le \rho \le b_r$$
$$\tau = \frac{3f(N_c+N_2)}{2\pi a^3}\left[(a^2-\rho^2)^{1/2}-2(b_r^2-\rho^2)^{1/2}+(1+\frac{\beta_1}{f})(b_{u\_*}^2-\rho^2)^{1/2}\right], a_0 \le \rho \le b_{u\_*}$$
$$\tau = \frac{3f(N_c+N_2)}{2\pi a^3}\left[(a^2-\rho^2)^{1/2}-2(b_r^2-\rho^2)^{1/2}+(1+\frac{\beta_1}{f})(b_{u\_*}^2-\rho^2)^{1/2}-\frac{\beta_1}{f}(a_0^2-\rho^2)^{1/2}\right], \rho \le a_0$$

(2.82)

Where

$$b_r = a(1-\frac{f(N_2+N_2^*)+T+T^*}{2f(N_c+N_2)})^{1/3} \tag{2.83}$$

Therefore the tangential displacement, as shown by curve BD (upper curve) in Figure 2.4(g), is given by

$$\delta_r = \frac{3(2-\nu)fa_c^2}{16\mu KR}\frac{a^2}{a_c^2}(1-2\frac{b_r^2}{a^2}+(1+\frac{\beta_1}{f})\frac{b_{u\_*}^2}{a^2}-\frac{\beta_1}{f}\frac{a_0^2}{a^2})$$
$$= \frac{3(2-\nu)fa_c^2}{16\mu KR}\{(1+\theta_2 L_2)^{2/3}-2\left[1-\frac{\theta_2}{2}(L_2^*-L_2)-\frac{L_2^*+L_2}{2}\right]^{2/3}+(1+\frac{1}{\theta_1})(1-\theta_2 L_2^*-\frac{2(\theta_1-\theta_2)}{(\theta_1+1)}L_2^*)^{2/3}-\frac{1}{\theta_1}(1+\theta_2 L_2^*-\theta_1 L_2^*)^{2/3}\}$$

(2.84)

And the tangential compliance is given by

$$c_r = \frac{d\delta_r}{dT} = \frac{2-\nu}{8\mu a}(\theta_2+(1-\theta_2)(1-(1+\theta_2)\frac{L_2^*+L_2}{2(1+\theta_2 L_2)})^{-1/3}) \tag{2.85}$$

Furthermore, since the initial traction at the end of load step 4 is given by equation (2.82), according to rule 2, the subsequent unloading (load step 5) traction is given by (shown in Figure 2.5(g))

$$\tau = -\frac{3f(N_c+N_2)}{2\pi a^3}(a^2-\rho^2)^{1/2}, b_{ru} \le \rho \le a$$
$$\tau = -\frac{3f(N_c+N_2)}{2\pi a^3}\left[(a^2-\rho^2)^{1/2}-2(b_{r_u}^2-\rho^2)^{1/2}\right], b_{r_*} \le \rho \le b_{r_u}$$
$$\tau = -\frac{3f(N_c+N_2)}{2\pi a^3}\left[(a^2-\rho^2)^{1/2}-2(b_{r_u}^2-\rho^2)^{1/2}+2(b_{r_*}^2-\rho^2)^{1/2}\right], b_{u\_*} \le \rho \le b_{r_*}$$
$$\tau = -\frac{3f(N_c+N_2)}{2\pi a^3}\left[(a^2-\rho^2)^{1/2}-2(b_{r_u}^2-\rho^2)^{1/2}+2(b_{r_*}^2-\rho^2)^{1/2}-(1+\frac{\beta_1}{f})(b_{u\_*}^2-\rho^2)^{1/2}\right], a_0 \le \rho \le b_{u\_*}$$
$$\tau = -\frac{3f(N_c+N_2)}{2\pi a^3}\left[(a^2-\rho^2)^{1/2}-2(b_{r_u}^2-\rho^2)^{1/2}+2(b_r^2-\rho^2)^{1/2}-(1+\frac{\beta_1}{f})(b_{u\_*}^2-\rho^2)^{1/2}+\frac{\beta_1}{f}(a_0^2-\rho^2)^{1/2}\right], \rho \le a_0$$

(2.86)

Where b_{ru}

$$b_{ru} = a(1-\frac{(T^*-T)(\beta_2-f)}{2f\beta_2(N_c+N_2)})^{1/3} \tag{2.87}$$

Therefore the tangential displacement, as given by curve DB (lower curve) in Figure 2.4(g), is given by

$$\begin{aligned}\delta_{ru} &= \frac{3(2-\nu)fa_c^2}{16\mu KR}\frac{a^2}{a_c^2}(2\frac{b_{ru}^2}{a^2}-2\frac{b_{r_*}^2}{a^2}+(1+\frac{\beta_1}{f})\frac{b_{u\_*}^2}{a^2}-\frac{\beta_1}{f}\frac{a_0^2}{a^2}-1)\\ &= \frac{3(2-\nu)fa_c^2}{16\mu KR}\{2\left[1+\frac{\theta_2}{2}(L_2^*+L_2)-\frac{L_2^*-L_2}{2}\right]^{2/3}-2(1-L_2^*)^{2/3}\\ &+(1+\frac{1}{\theta_1})(1-\theta_2L_2^*-\frac{2(\theta_1-\theta_2)}{(\theta_1+1)}L_2^*)^{2/3}-\frac{1}{\theta_1}(1+\theta_2L_2^*-\theta_1L_2^*)^{2/3}-(1+\theta_2L_2)^{2/3}\}\end{aligned} \tag{2.88}$$

The tangential compliance is given by equation (2.81).

$$c_{ru} = \frac{d\delta_{ru}}{dT} = \frac{2-\nu}{8\mu a}(-\theta_2+(1+\theta_2)(1-(1-\theta_2)\frac{L_2^*-L_2}{2(1+\theta_2L_2)})^{-1/3}) \tag{2.89}$$

Further reloading and unloading steps can be treated in the same manner as described above. In this case also we note a dissipation of energy as the contact undergoes unload-reload cycles.

2.7 Summary

In a pioneering paper, Mindlin and Deresiewicz (MD53) had developed methods and expressions for the force-deformation relationships of contacting elastic spheres subjected to oscillating oblique loading whose inclination or oblique ratio remains constant during the loading process. They had presented two methods of analysis; the incremental and the continuous method. The incremental method relies on the current loading condition of the contact, while the continuous method incorporates the loading history. This chapter has extended the continuous method to contacts under oblique forces whose inclination is different at different loading stages. We have presented a general procedure for obtaining the tangential traction at any loading stage of both monotonic and cyclic loading. Since this procedure updates the tangential traction with loading, it has the ability to account for the effect of loading history on the contact behavior. Once the tangential traction has been determined, the tangential displacement and the compliance can be obtained. The devised procedure was applied to study selected loading cases with different oblique ratios under both monotonic and cyclic loading paths. The procedure was also applied to describe the cyclic behavior with

complicated initial state of tangential traction. The contact tangential traction was found to be strongly dependent upon the oblique ratio and the contact loading history. As a result, it was demonstrated that the tangential displacement, compliance and energy dissipation can be totally different for different loading paths although the final loading state may be same. This loading history effect cannot be easily described by the traditional plasticity models or incremental method. The developed procedure can be applied to arbitrary loading paths that may be encountered in contact mechanics of rough surfaces and granular materials.

This page left intentionally blank.

Chapter 3 Asperity Contact Mechanics – Out-of-plane Loading

In the last chapter, we have extended the continuous method to contacts under oblique forces whose inclination is different at different loading stages. These solutions are based on the fundamental work of Cattaneo and Mindlin (referred as C-M solutions hereafter). We also have presented a general procedure for obtaining the tangential traction at any loading stage of both monotonic and cyclic loading.

It is noteworthy that the C-M solutions for elastic sphere contacts are incomplete and require additional considerations in a number of aspects. We mention here three fundamental aspects that pertain to the relatively simple loading conditions which comprises the application of a shear action while an initially applied normal force is held constant. Firstly, the C-M solutions neglect the transverse tangential tractions perpendicular to the direction of applied shear force that arise due to the Poisson's ratio effect. Secondly, these solutions do not consider tangential forces that do not pass through the center of the contact area and produce a twisting moment. Thirdly, these solutions only consider contact loading confined within an *N*-*T* plane as shown in Figure 3.1. Subsequent application of out-of-plane tangential loading, such as that denoted by T_2, was not considered. The first two aspects have been investigated in some detail [72-75]; however, the third aspect has received scant attention. While it is tempting to consider the general problem of tangential loading, the complexities of the solutions are likely to

obfuscate the individual effects produced by these aspects, particularly for the first and third aspects, since they deal with tangential loading passing through the center of the contact area. In this chapter, we focus our effort upon contact of similar spheres that are subjected to sequential tangential loading that is not confined within a unique *N*-*T* plane. For contact of similar spheres, the overall tangential compliance are known to be insignificantly affected by the transverse tangential tractions that arise due to the Poisson's ratio effect [75]. Therefore, to simplify our development we ignore the contributions of the transverse tangential tractions (first aspect).

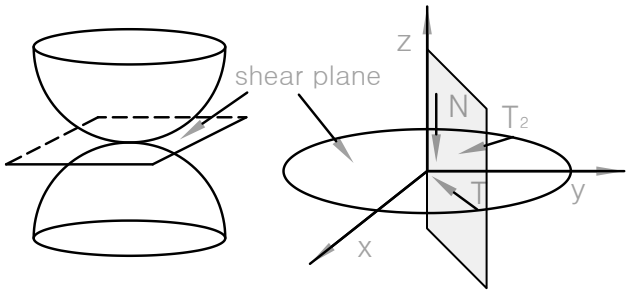

Figure 3.1: Schematic of arbitrarily directed contact shear loading.

We note that for loading confined in-plane, a contact can be considered to be undergoing either loading or unloading. However, when the shear forces are out-of-plane, both loading and unloading can happen simultaneously in orthogonal shear directions. It is found in this chapter that the C-M solution cannot be used when *N*-*T* is not confined to a plane and that the C-M solutions are only a special case of the arbitrarily directed shear plane loading. Since the contact problems are well known to be path dependent due to energy dissipation, the tangential forces and tractions are recorded during the contact

loading process. Once the solution for the tangential traction has been established, tangential displacement and compliance can be obtained.

In the following discussion, we first summarize the basic characteristics of the elastic sphere contact problem based upon the previous work. We then present the tangential traction based upon the elastic half space theory. Subsequently, we derive the tangential tractions under different loading conditions, and obtain the expressions for tangential displacements and compliances. We then present a numerical example to illustrate the methodology for the sequential application of two shear forces. Finally, we describe how the method is generalized as the contact is subjected to sequential application of more than two arbitrarily directed shear forces.

3.1 Fundamental assumptions of contact theory of elastic spheres

The contact behavior of elastic spheres subjected to tangential loading has the following characteristic[3, 64]:

1) The forces acting on the contacting bodies at any pair of contact points are equal with opposite direction per Newton's third law. In addition, an infinitesimal tangential force dT results in a uniform infinitesimal tangential displacement of the contact surface prior to contact sliding. Therefore, the contact problem is posed as a mixed boundary-value problem in elasticity.

2) The superposition of contact tangential tractions results in a uniform contact

tangential displacement, if each traction distribution itself causes a uniform tangential displacement at the contact. This superposition is known as Cattaneo's technique.

3) Coulomb-Amonton's law is satisfied, which requires that the tangential traction not exceed the slip limit on the contact surface. In a recent paper this assumption has been challenged in favor of plastic yielding [76]. However, for loading within elastic limits and for brittle materials, such as ceramics and rock minerals, the condition of partial slip at contact edge is a reasonable assumption.

Furthermore, the following assumptions are adopted to simplify the analysis for the contact of similar spheres:

1) Normal loading obeys Hertz theory [1, 2] and the normal traction is not affected by tangential traction.

2) The tangential traction is not affected by normal traction and is given by the elastic half-space theory. The transverse tangential tractions that arise due to the Poisson's ratio effect are ignored. The tangential displacement is uniquely determined by the tangential traction.

3.2 Force-displacement relationship under tangential loading with varying directions

3.2.1 Classical Cattaneo-Mindlin (C-M) solution

For contact of spherical bodies, the Hertz theory gives the relationship of circular contact surface radius and normal force as:

$$a = (KNR)^{1/3} \tag{3.1}$$

where N is the normal force, R is the radius of spheres, and $K = 3(1-\nu^2)/4E$, in which ν and E are the material Poisson's ratio and Young's modulus, respectively. The normal displacement and the distribution of normal traction on the contact surface are given by

$$\delta_n = \frac{a^2}{R} \tag{3.2}$$

$$\sigma_n = \frac{3N}{2\pi a^3}(a^2 - \rho^2)^{1/2} \tag{3.3}$$

where ρ is the radial distance from the contact center. For constant normal force, the tangential traction caused by a shear force T_1, directed at an angle θ_1 form the x-axis in x-y plane is given by the following expression [63, 69]:

$$\begin{aligned}
\tau_x &= \frac{3f\cos\theta_1 N}{2\pi a^3}(a^2-\rho^2)^{1/2}, c \le \rho \le a \\
\tau_x &= \frac{3f\cos\theta_1 N}{2\pi a^3}\left[(a^2-\rho^2)^{1/2} - (c^2-\rho^2)^{1/2}\right], \rho \le c \\
\tau_y &= \frac{3f\sin\theta_1 N}{2\pi a^3}(a^2-\rho^2)^{1/2}, c \le \rho \le a \\
\tau_y &= \frac{3f\sin\theta_1 N}{2\pi a^3}\left[(a^2-\rho^2)^{1/2} - (c^2-\rho^2)^{1/2}\right], \rho \le c
\end{aligned} \tag{3.4}$$

where f is the friction coefficient, and the radius of the stick area, c, is given by:

$$c = a\left(1 - \frac{T_1}{fN}\right)^{1/3} \tag{3.5}$$

Since θ expresses the directional information of the tangential forces in the formula, all of the equations in this chapter take the absolute value of the shear forces *T*. The tangential displacement in the x-direction of a point far removed from the interface is given by

$$\delta_{x1} = \frac{3(2-\nu) f \cos\theta_1 N}{16\mu a}(1-\frac{c^2}{a^2}) = \frac{3(2-\nu) f \cos\theta_1 N}{16\mu a}\left[1-(1-\frac{T_1}{fN})^{2/3}\right] \qquad (3.6)$$

where μ is the shear modulus and the relative tangential displacement between two similar spheres in contact is twice that given in equation (3.6). This, the tangential compliance is given by

$$c_{x1} = \frac{d\delta_{x1}}{dT} = \frac{(2-\nu)\cos\theta_1}{8\mu a}(1-\frac{T_1}{fN})^{-1/3} \qquad (3.7)$$

Similarly, the displacement and compliance in the y-direction can be obtained by replacing $\cos\theta_1$ with $\sin\theta_1$ in equations (3.6) and (3.7). For illustration, we plot in Figure 3.2(a) and Figure 3.2(b), the tangential traction when the contact is subjected to a tangential force along the x-direction (θ_1=0). Figure 3.2(a) gives the distribution of the tangential traction on the contact area. The inner circle represents the stick region, while the annular space *c*-*a*, represents the slip region. Figure 3.2(b) gives the profile of the tangential traction along with the slip limit. For this case of shear loading, the slip-

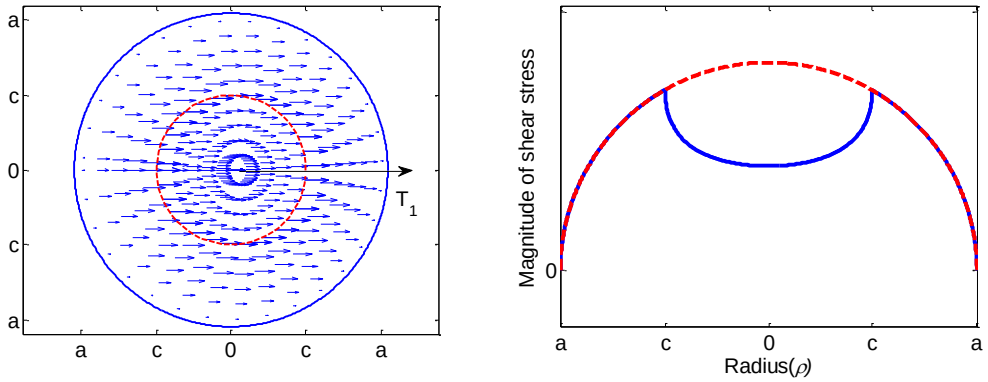

Figure 3.2: Tangential traction field: (Left) vector plot, and (Right) profile plot with slip limit (dashed lines) showing contact traction distribution.

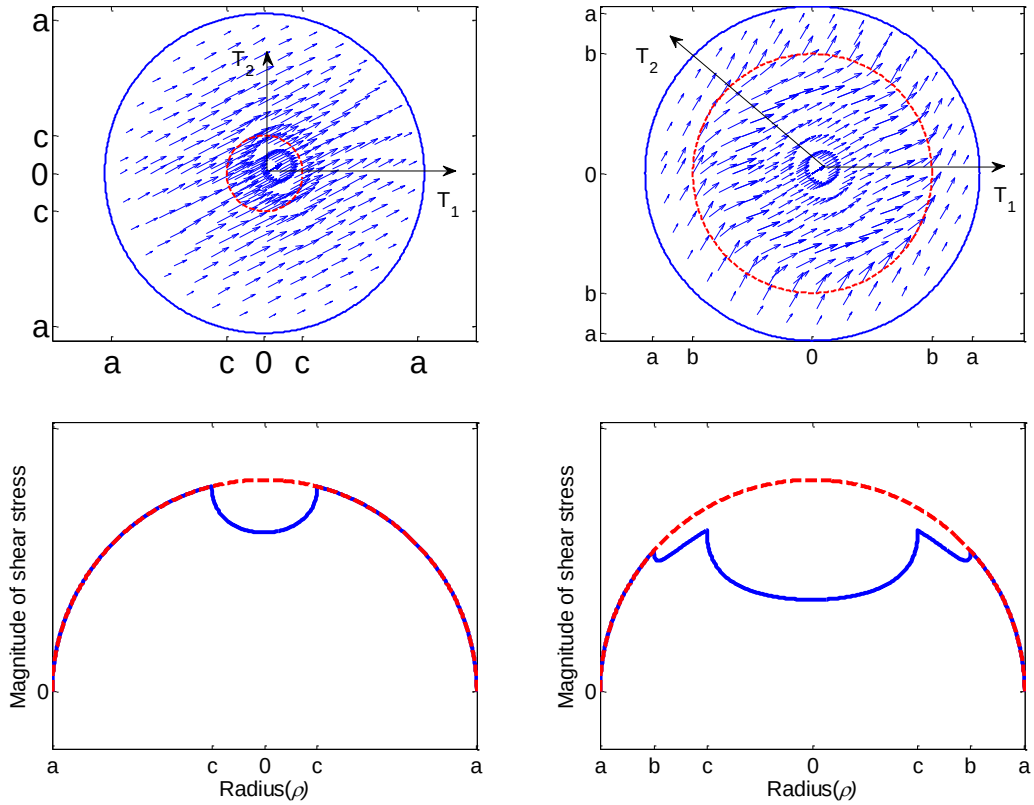

Figure 3.3: Tangential traction field: (a) and (b) vector plot, and (c) and (d) profile plot with slip limit (dashed lines) showing contact traction distribution for two loading cases(Case 1: $|\theta_2-\theta_1|\leq\pi/2$ and Case 2: $|\theta_2-\theta_1|>\pi/2$).

direction, the tangential displacement direction and the shear force-direction all lie on the N-T_1 plane.

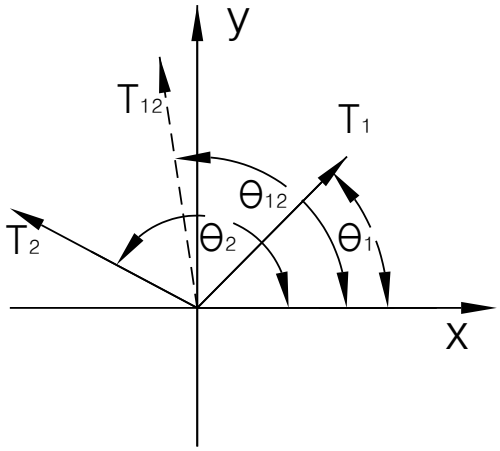

Figure 3.4: Loading in shear plane.

3.2.2 Solutions for varying tangential loading directions

Now, in addition to T_1, we consider a new shear force T_2, directed at an angle θ_2 as shown in Figure 3.3, which does not lie in the N-T_1 plane. Since the normal force is constant, a slip annulus will be present. The new shear force could result in either the growth of the existing slip annulus or the development of a new slip annulus. Let us first consider that a new slip annulus a-b develops (the conditions for the validity of this assumption will be determined later). In this case, the tangential traction due to T_2 will be given by

$$
\begin{aligned}
\tau_x &= \frac{3k\cos\theta_2 N}{2\pi a^3}(a^2-\rho^2)^{1/2}, b \le \rho \le a \\
\tau_x &= \frac{3k\cos\theta_2 N}{2\pi a^3}\left[(a^2-\rho^2)^{1/2}-(b^2-\rho^2)^{1/2}\right], \rho \le b \\
\tau_y &= \frac{3k\sin\theta_2 N}{2\pi a^3}(a^2-\rho^2)^{1/2}, b \le \rho \le a \\
\tau_y &= \frac{3k\sin\theta_2 N}{2\pi a^3}\left[(a^2-\rho^2)^{1/2}-(b^2-\rho^2)^{1/2}\right], \rho \le b
\end{aligned}
\tag{3.8}
$$

Where, using the equilibrium condition which indicates the integration of equation (3.8) equals T_2, b is given by

$$
b = a\left(1-\frac{T_2}{kN}\right)^{1/3} \tag{3.9}
$$

Note that in equations (3.8) and (3.9), f is replaced by a yet to be determined positive constant k. We note here that the constant k will be determined considering the Amonton's law in the slip region. In this case, the total traction is obtained via the superposition of equations (3.4) and (3.8) as follows:

$$
\begin{aligned}
\tau_x &= \frac{3(k\cos\theta_2 + f\cos\theta_1)N}{2\pi a^3}(a^2-\rho^2)^{1/2}, b \le \rho \le a \\
\tau_x &= \frac{3N}{2\pi a^3}\left[(k\cos\theta_2 + f\cos\theta_1)(a^2-\rho^2)^{1/2} - k\cos\theta_2(b^2-\rho^2)^{1/2}\right], c < \rho \le b \\
\tau_x &= \frac{3N}{2\pi a^3}\left[(k\cos\theta_2 + f\cos\theta_1)(a^2-\rho^2)^{1/2} - k\cos\theta_2(b^2-\rho^2)^{1/2} - f\cos\theta_1(c^2-\rho^2)^{1/2}\right], 0 < \rho \le c \\
\tau_y &= \frac{3(k\sin\theta_2 + f\sin\theta_1)N}{2\pi a^3}(a^2-\rho^2)^{1/2}, b \le \rho \le a \\
\tau_y &= \frac{3N}{2\pi a^3}\left[(k\sin\theta_2 + f\sin\theta_1)(a^2-\rho^2)^{1/2} - k\sin\theta_2(b^2-\rho^2)^{1/2}\right], c < \rho \le b \\
\tau_y &= \frac{3N}{2\pi a^3}\left[(k\sin\theta_2 + f\sin\theta_1)(a^2-\rho^2)^{1/2} - k\sin\theta_2(b^2-\rho^2)^{1/2} - f\sin\theta_1(c^2-\rho^2)^{1/2}\right], 0 < \rho \le c
\end{aligned}
\tag{3.10}
$$

The corresponding tangential displacement of a distant point is given by

$$\delta_{x2} = \frac{3(2-\nu)(f\cos\theta_1 + k\cos\theta_2)N}{16\mu a}\left(1 - \frac{k\cos\theta_2}{f\cos\theta_1 + k\cos\theta_2}\frac{b^2}{a^2} - \frac{f\cos\theta_1}{f\cos\theta_1 + k\cos\theta_2}\frac{c^2}{a^2}\right)$$
$$= \frac{3(2-\nu)(f\cos\theta_1 + k\cos\theta_2)N}{16\mu a}\left(1 - \frac{k\cos\theta_2}{f\cos\theta_1 + k\cos\theta_2}\left(1 - \frac{T_2}{kN}\right)^{2/3} - \frac{f\cos\theta_1}{f\cos\theta_1 + k\cos\theta_2}\left(1 - \frac{T_1}{fN}\right)^{2/3}\right) \quad (3.11)$$

And the compliance when applying T_2 is given by

$$c_{x2} = \frac{d\delta_{x2}}{dT_2} = \frac{(2-\nu)\cos\theta_2}{8\mu a}\left(1 - \frac{T_2}{kN}\right)^{-1/3} \quad (3.12)$$

The displacement and compliance in the y-direction are given by (3.11) and (3.12) after cosine is replaced by sine as before.

Since the slip goes from *a* inward to *b*, the tangential traction in that region *a*-*b* has to satisfy Amonton's law, which results in the following condition from equation (3.10):

$$(f\cos\theta_1 + k\cos\theta_2)^2 + (f\sin\theta_1 + k\sin\theta_2)^2 = f^2 \quad (3.13)$$

Thus, *k* is obtained as follows by rewriting equation (3.13)

$$k = -2f\cos(\theta_1 - \theta_2) \quad (3.14)$$

We see from equation (3.14) that the constant, *k*, takes a positive value only for the condition $|\theta_1\text{-}\theta_2| > \pi/2$. Thus the assumption that a new slip annulus develops with the application of T2 is valid only for this condition.

When $|\theta_1\text{-}\theta_2| \le \pi/2$, equation (3.14) leads to a negative value for constant, *k*. Therefore, the assumption that a new slip annulus develops is not valid. In this case the existing slip annulus caused by shear force T_1 will continue to develop inward from *c* as T_2 increases. The developed slip annulus will be determined by the vector sum of T_1 and T_2 and the traction, in this case will be given by

$$\tau_x = \frac{3f\cos\theta_{12}N}{2\pi a^3}(a^2-\rho^2)^{1/2}, c \le \rho \le a$$
$$\tau_x = \frac{3f\cos\theta_{12}N}{2\pi a^3}\left[(a^2-\rho^2)^{1/2}-(c^2-\rho^2)^{1/2}\right], \rho \le c$$
$$\tau_y = \frac{3f\sin\theta_{12}N}{2\pi a^3}(a^2-\rho^2)^{1/2}, c \le \rho \le a \qquad (3.15)$$
$$\tau_y = \frac{3f\sin\theta_{12}N}{2\pi a^3}\left[(a^2-\rho^2)^{1/2}-(c^2-\rho^2)^{1/2}\right], \rho \le c$$

In addition, the direction of vector sum of T_1 and T_2, denoted by θ_{12} is given by

$$\cos\theta_{12} = \frac{T_1\cos\theta_1 + T_2\cos\theta_2}{\sqrt{T_1^2+T_2^2+2T_1T_2\cos(\theta_1-\theta_2)}}$$
$$\sin\theta_{12} = \frac{T_1\sin\theta_1 + T_2\sin\theta_2}{\sqrt{T_1^2+T_2^2+2T_1T_2\cos(\theta_1-\theta_2)}} \qquad (3.16)$$

and, c is given by

$$c = a\left(1-\frac{\sqrt{T_1^2+T_2^2}}{fN}\right)^{1/3} \qquad (3.17)$$

The displacement in x direction are given by equation(2.8) after $\cos\theta_1$ is replaced by $\cos\theta_{12}$, and the compliance is given by

$$c_{x2} = \frac{d\delta_x}{dT_2} = \frac{(2-\nu)\cos\theta_{12}}{8\mu a}\left(1-\frac{\sqrt{T_1^2+T_2^2}}{fN}\right)^{-1/3}\frac{T_2}{\sqrt{T_1^2+T_2^2}} \qquad (3.18)$$

The tangential traction vector fields and the tangential traction profiles for the two cases, case 1 with $|\theta_2-\theta_1| \le \pi/2$ and case 2 with $|\theta_2-\theta_1| > \pi/2$ are shown in Figure 3.3. In Figure 3.3(a), we observe that the tangential traction field for case 1 is directed along a unique N-T plane formed by the normal force N and resultant shear force T_{12} (see Figure 3.4). In contrast in Figure 3.3(b), the tangential traction field is not directed along a unique N-T

plane. The direction in the slip region *a*-*b* is different from that in the stick region. In addition, Figure 3.3(c) and Figure 3.3(d) give the tangential traction profile along with the slip limit for the two cases. It is also noted that for case 1, the slip direction is parallel to the resultant force direction of T_{12}. However, for case 2, the slip direction is not parallel to the resultant force direction of T_{12}.

Now let us define the angle between slip direction and x-axis, as θ_s, such that equation (3.13) can be rewritten in the following form:

$$(f\cos\theta_s)^2 + (f\sin\theta_s)^2 = f^2 \tag{3.19}$$

where the slip direction θ_s is illustrated in Figure 3.5. From the Figure 3.5 and equation (3.14), θ_s for case 2 is given by

$$\begin{cases} \cos\theta_s = \cos\theta_1 - 2\cos(\theta_1 - \theta_2)\cos\theta_2 \\ \sin\theta_s = \sin\theta_1 - 2\cos(\theta_1 - \theta_2)\sin\theta_2 \end{cases} \tag{3.20}$$

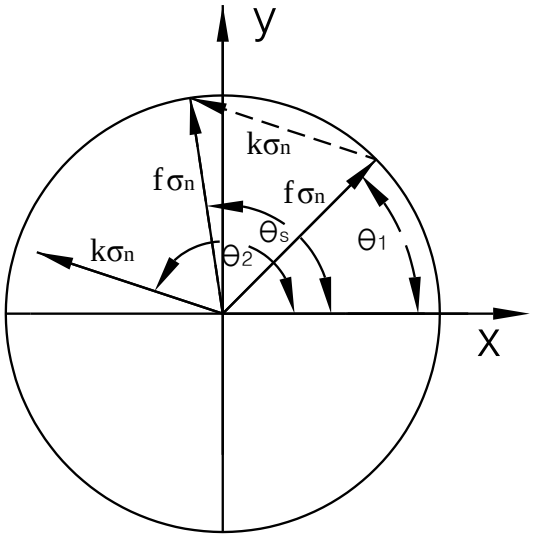

Figure 3.5: Determination of slip direction.

We observe from equation (3.20) that the slip direction is independent of the applied shear force magnitude. For $|\theta_1-\theta_2| = \pi$, which is same as the unloading condition discussed by Mindlin and Deresiewicz [3], equation (3.20) yields $\theta_s=-\theta_1$, that is, the slip direction is opposite to the initial loading direction as expected. Furthermore, in this case, it can be seen that equations (3.10), (3.11) and (3.12) recover back to Mindlin and Deresiewicz's results.

As the shear force T_2 increases, the slip annulus *a-b* expands as *b* moves inwards. When $b=c$, at shear force T_2 equal to say T_2' *(T_2 prime)*, the total traction in equation (3.10) is reduced to

$$\begin{aligned}
\tau_x &= \frac{3(f\cos\theta + k\cos\theta_2)N}{2\pi a^3}(a^2-\rho^2)^{1/2}, c \le \rho \le a \\
\tau_x &= \frac{3(f\cos\theta + k\cos\theta_2)N}{2\pi a^3}\left[(a^2-\rho^2)^{1/2} - (c^2-\rho^2)^{1/2}\right], \rho \le c \\
\tau_y &= \frac{3(f\sin\theta + k\sin\theta_2)N}{2\pi a^3}(a^2-\rho^2)^{1/2}, c \le \rho \le a \\
\tau_y &= \frac{3(f\sin\theta + k\sin\theta_2)N}{2\pi a^3}\left[(a^2-\rho^2)^{1/2} - (c^2-\rho^2)^{1/2}\right], \rho \le c
\end{aligned} \tag{3.21}$$

Equation (3.21) can be written in an alternative form as:

$$\begin{aligned}
\tau_x &= \frac{3f\cos\theta_s N}{2\pi a^3}(a^2-\rho^2)^{1/2}, c \le \rho \le a \\
\tau_x &= \frac{3f\cos\theta_s N}{2\pi a^3}\left[(a^2-\rho^2)^{1/2} - (c^2-\rho^2)^{1/2}\right], \rho \le c \\
\tau_y &= \frac{3f\sin\theta_s N}{2\pi a^3}(a^2-\rho^2)^{1/2}, c \le \rho \le a \\
\tau_y &= \frac{3f\sin\theta_s N}{2\pi a^3}\left[(a^2-\rho^2)^{1/2} - (c^2-\rho^2)^{1/2}\right], \rho \le c
\end{aligned} \tag{3.22}$$

Where we use the relationship in equation (3.19). Since $b=c$, from equations (3.5) and (3.9), we have

$$\frac{T_1}{f} = \frac{T_2}{k} \tag{3.23}$$

Which leads to $\theta_s = \theta_{12}$ (see Figure 3.4 and Figure 3.5) using the fact that f and k are proportional to T_1 and T_2. Clearly, when $T_2=T_2'$, the tangential traction is the same as the traction caused by a shear force T_{12}' which is a vector sum of T_1 and T_2'.

As we keep increasing T_2, the new traction is obtained by applying T_{12}' and T_2-T_2'. The angle between T_{12}' and T_2-T_2' is equal to θ_2-θ_s and is given by (using equation (3.14) and geometry)

$$\arccos(\theta_2 - \theta_s) = \frac{k^2 + fk\cos(\theta_2 - \theta_1)}{fk} = \frac{2f^2\cos^2(\theta_2 - \theta_1)}{fk} > 0 \tag{3.24}$$

From equation (3.24) we can see θ_2-θ_s is less than $\pi/2$. Thus the problem becomes same as that of case 1 with $|\theta_2$-$\theta_1| \leq \pi/2$. Therefore, new traction can be directly obtained by applying T_{12}, and the slip direction becomes same as the total force direction. Needless to say, equation (3.20) is only applicable when $b>c$.

3.3 Illustrative example

We now use the developed method to illustrate the effect of varying tangential force direction upon the tangential-force displacement behavior through two numerical examples for the case $|\theta_1$-$\theta_2| > \pi/2$. In these examples, we first apply T_1 along the x-

direction, and then apply T_2 such that $|\theta_2-\theta_1|=2\pi/3$ in example 1, and $|\theta_2-\theta_1|=5\pi/6$ in example 2. The overall shear-force displacement curves for the two examples are shown in Figure 3.6(a). As the shear force T_2 is applied, the contact first experiences unloading from A to B1 or B2 as the overall shear force decreases. Subsequently, as T_2 is increased further, the overall shear force begins to increase and the contact again experiences loading from B1 or B2 to A to C. The resultant hysteretic loop represents a loss of energy during this loading process. The size of the loop is determined by the direction of shear force T_2 as seen from Figure 3.6(a). We further note that the direction of the resultant shear force changes during this loading process. However, the shear displacement is not coaxial with the resultant shear force during the unloading step A-B1 and A-B2, and reloading step B1-A and B2-A as shown in Figure 3.6(b). Such non-coaxiality between shear force and shear displacement cannot be easily described by contact models based upon 2-dimensional plasticity theories [62].

Now, if a third force T_3 directed at an angle θ_3 to the x-axis is applied, we first determine the angle $|\theta_3-\theta_s|$, where θ_s is the current slip direction. If $|\theta_3-\theta_s|\leq\pi/2$, the existing slip annulus will grow as in case 1 of Figure 3.4, while the traction distribution will retain its history. The total traction for this loading can be obtained by sequentially applying shear forces T_1 and the vector sum T_{23} of shear forces T_2 and T_3. If, on the other hand, $|\theta_3-\theta_s|>\pi/2$, a new slip annulus will develop. The new traction is given by the superposition

of the tractions due to T_{12} (obtained for case 1 using equations (3.15) and for case 2 using equations (3.10) and (3.22)) and the tangential traction due to the new force T_3 given by equation (3.8).

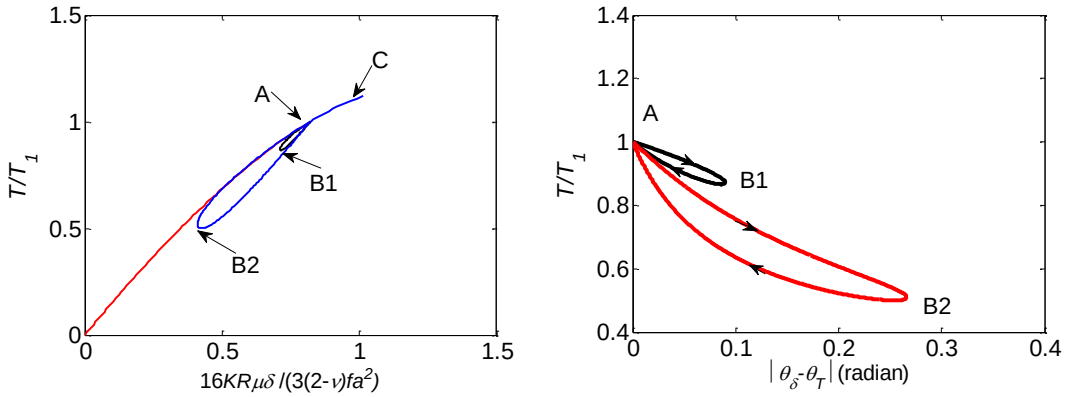

Figure 3.6: (a) Shear force-displacment curve; (b) The angle between the shear force and shear displacment showing non-coaxiality as the contact experiences unloading and reloading.

3.4 Summary

In applications such as contact mechanics of rough surfaces and discrete element modeling of granular media, the contacts are subjected to tangential forces that are not maintained in a unique *N*-*T* plane at different loading stages. The original C-M solutions as well later advancement of tangential contact problems along the lines of C-M solutions do not address the cases wherein the contact is subjected to sequential application of arbitrarily directed shear forces in the contact tangential plane. We have found that under such general loading condition, the contact undergoes simultaneous loading and unloading in orthogonal directions on the shear plane. Thus the tangential traction,

displacement and compliance cannot be merely labeled as that for loading or unloading condition. Moreover, due to its path dependent nature, the tangential traction cannot be simplified as that due to a resultant force. Instead, for each shear force application, the entire loading history has to be considered. In this chapter, a path dependent analysis of elastic sphere contact is presented that utilizes superposition to derive the expressions of the contact tangential traction at each loading step. The displacement and compliance are, subsequently, obtained based on the tangential traction. We have shown that the C-M solution is a special case when the angle $|\theta_i-\theta_j|=\pi$ in the general loading condition, where θ_i and θ_j represent the directions of the existing and the newly applied shear forces, respectively. We also find that the slip direction is more complicated than in C-M solution, in which the slip direction always coincides with the last applied shear force. Finally, we have presented numerical examples that show the development of hysteretic loop and non-coaxiality of shear force and displacement when the contact is subjected to sequentially applied shear force such that $|\theta_i-\theta_j|>\pi/2$. The hysteretic loop represents energy loss during the loading process. Since the contact undergoes simultaneous loading and unloading in out-of-plane loading condition, the energy dissipation is thus less than pure unloading in in-plane loading condition. In other words, the in-plane loading yields the upper bound of the energy dissipation as in Figure 3.7. These additional effects are

not insignificant even for contact of similar spheres for which the Poisson's ratio effect are typically small [75].

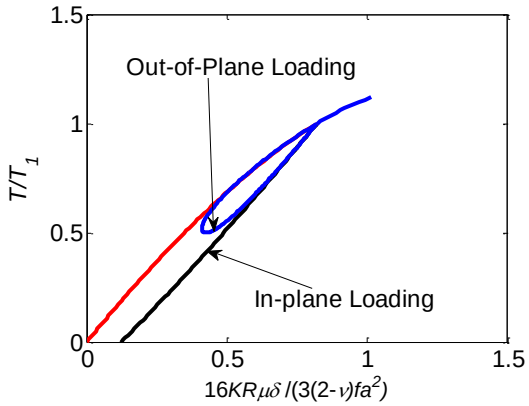

Figure 3.7: Upper bound energy dissipation of the in-plane loading.

Chapter 4 Statistical Description of the Rough Interface

In last two chapters, we discussed an asperity contact behavior modeled as the contact of two elastic spheres. The solutions are based on half space theory and perfect smooth surface assumption is made. However, in microscopic view, there is no perfect smooth surface. All the surfaces are rough and considered to be made of numerous irregular asperities. Thus the description of the surface became complicated. For these irregular surfaces, statistical method is an attractive choice. The pioneering work regarding the rough surface statistical description was done by Longuet-Higgins[77, 78], who used random process to describe the sea surface. His work was subsequently introduced to contact mechanics as a method to described real surfaces by Nayak [19, 35, 36]. From then on, their works have been widely cited to study the contact between a rough surface and a plane[79-82]. However, in reality, the contact is between two rough surfaces. When two rough surfaces come into contact, numerous asperity contacts are formed. Whether an asperity contact forms or not depends on the composite height-asperity contact height. In other words, whether two asperities touch each other or not depends on the sum of their heights. In addition to the asperity contact formation, the way they are formed, such as the contact orientation and equivalent curvature, is significant. Thus two rough surface contacts are more complicated than the contact of one rough surface with a

plane. In this chapter, we have used Longuet-Higgins and Nayak's approach to study the statistical property of the contact of two rough surfaces.

4.1 Joint probability of interface variables

Following the random process description of a rough surface introduced by Longuet-Higgins[77, 78], we use 2-dimensional Fourier series to describe the two surfaces. Accordingly, the height of the lower surface and upper surface can be written as follows

$$z_1(x,y) = \sum_n c_{n1} \cos(xk_{xn} + yk_{yn} + \varepsilon_{n1}) \tag{4.1}$$

$$z_2(x,y) = \sum_n c_{n2} \cos(xk_{xn} + yk_{yn} + \varepsilon_{n2}) \tag{4.2}$$

where k_{xn},k_{yn} are the wave numbers, ε_{n1} and ε_{n2} are the random phases for each surface with a uniform probability in the range of $(0,2\pi)$, and c_{n1} and c_{n2} are the Fourier coefficients. Figure 4.1 is an example for the surface generation using 2-d Fourier series.

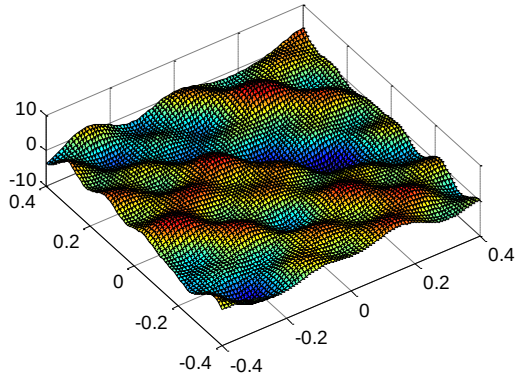

Figure 4.1: Rough surface generation using 2-d Fourier series.

The formation of asperity contacts depends on the sum of the two corresponding asperity heights, i.e., asperity contact height. Thus we define the composite topography as the sum of the two surfaces:

$$z(x,y) = z_1 + z_2 = \sum_{n1} c_{n1} \cos(xk_{xn1} + yk_{yn1} + \varepsilon_{n1}) + \sum_{n2} c_{n2} \cos(xk_{xn2} + yk_{yn2} + \varepsilon_{n2}) \quad (4.3)$$

Due to the symmetric property of the Fourier series, the mean value of the surface heights is zero, and the variance of composite height is obtained as

$$\sigma^2 = \frac{1}{A} \iint_A z(x,y)^2 dxdy \quad (4.4)$$

where A is the surface domain. Due to the orthogonal property of the Fourier basis functions, equation(4.4) yields

$$\sigma^2 = \frac{1}{2}\left(\sum_{n1} c_{n1}^2 + \sum_{n2} c_{n2}^2 \right) \quad (4.5)$$

On the other hand, the variance of the composite height can be obtained from its power spectral density (PSD), $\Phi(k_x,k_y)$[77, 78]. Thus we have

$$\sigma^2 = \int_{-\infty}^{\infty} \int_{-\infty}^{\infty} \Phi(k_x, k_y) dk_x dk_y = \frac{1}{2}\left(\sum_{n1} c_{n1}^2 + \sum_{n2} c_{n2}^2 \right) \quad (4.6)$$

Similarly, higher moments of the composite heights can be determined as

$$m_{pq} = \int_{-\infty}^{\infty} \int_{-\infty}^{\infty} k_x^p k_y^q \Phi(k_x, k_y) dk_x dk_y \quad (4.7)$$

which leads to the following expression for higher moments of the composite height, m_{pq}

$$m_{pq} = \frac{1}{2}\left(\sum_n c_{n1}^2 k_{xn}^p k_{yn}^q + \sum_n c_{n2}^2 k_{xn}^p k_{yn}^q \right) = m_{pq1} + m_{pq2} \quad (4.8)$$

We now consider a profile defined as the intersection of the surface with a vertical plane along the azimuthal direction, ϕ. The moments of the composite heights of the resultant profile are written as:

$$m_p(\phi) = \int_{-\infty}^{\infty} \omega^p \Phi_\phi(\omega) d\omega \tag{4.9}$$

where ω is the wave number and Φ_ϕ is the profile PSD. It was shown by Longuet-Higgins [77, 78] that moments, m_{pq}, of the surface is related to the moment of a profile, m_p, as follows:

$$m_n(\phi) = m_{n,0}\cos^n\phi + C_1^n m_{n-1,1}\cos^{n-1}\phi\sin\phi + ... + m_{0,n}\sin^n\phi \tag{4.10}$$

where C_r^n is the binomial coefficient. Furthermore, for isotropic surfaces the PSD of the profile should be independent of azimuthal direction, ϕ, thus we have

$$\begin{cases} m_{20} = m_{02} = m_2; m_{11} = m_{33} = m_{31} = 0 \\ m_{00} = m_0; 3m_{22} = m_{40} = m_{04} = m_4 \end{cases} \tag{4.11}$$

In order to study the joint probability of the random variables of interest in contact mechanics, we follow Longuet-Higgins and Nayak notations, defined as

$$\begin{cases} \xi_1 = z = z_1 + z_2 & \xi_4 = \dfrac{\partial^2 z}{\partial x^2} \\ \xi_2 = \dfrac{\partial z}{\partial x} & \xi_5 = \dfrac{\partial^2 z}{\partial x \partial y} \\ \xi_3 = \dfrac{\partial z}{\partial y} & \xi_6 = \dfrac{\partial^2 z}{\partial y^2} \end{cases} \tag{4.12}$$

The variables ξ_1 ξ_2… ξ_6 satisfy the central limit theorem and their joint probability density is given by the following multivariate Gaussian density function:

$$p(\xi_1 ... \xi_6) = (2\pi)^{-\frac{n}{2}} \Delta^{-\frac{n}{2}} \exp(-\frac{1}{2} M_{ij}\xi_i\xi_j) \tag{4.13}$$

Where M_{ij} is the inverse of the covariance matrix N_{ij}

$$N = \begin{pmatrix} \overline{\xi_1\xi_1} & \overline{\xi_1\xi_2} & \cdots & \overline{\xi_1\xi_n} \\ \overline{\xi_2\xi_1} & & & \\ \overline{\xi_n\xi_2} & \cdots & \cdots & \overline{\xi_n\xi_n} \end{pmatrix} \tag{4.14}$$

$$\overline{\xi_1\xi_1} = \frac{1}{A}\iint_A \left(\sum_{n1} c_{n1} \cos(xk_{xn1} + yk_{yn1} + \varepsilon_{n1}) + \sum_{n2} c_{n2} \cos(xk_{xn2} + yk_{yn2} + \varepsilon_{n2}) \right)^2 dxdy \tag{4.15}$$

Similarly

$$\overline{\xi_2\xi_2} = \frac{1}{A}\iint_A \left(\sum_{n1} -c_{n1}k_{xn1} \sin(xk_{xn1} + yk_{yn1} + \varepsilon_{n1}) + \sum_{n2} -c_{n2}k_{xn2} \sin(xk_{xn2} + yk_{yn2} + \varepsilon_{n2}) \right)^2 dxdy$$

(4.16)

and so on for other covariances. Thus we have

$$N_{ij} = \begin{pmatrix} m_{00} & 0 & 0 & -m_{20} & -m_{11} & -m_{02} \\ 0 & m_{20} & m_{11} & 0 & 0 & 0 \\ 0 & m_{11} & m_{02} & 0 & 0 & 0 \\ -m_{20} & 0 & 0 & m_{40} & m_{31} & m_{22} \\ -m_{11} & 0 & 0 & m_{31} & m_{22} & m_{13} \\ -m_{02} & 0 & 0 & m_{22} & m_{13} & m_{04} \end{pmatrix} \tag{4.17}$$

We note that covariances involving odd functions vanish in equation (4.17) implying that the distribution of slopes is independent of the heights and curvatures. The inverse of the matrix N_{ij} is as follows

$$M_{ij}=\begin{pmatrix} \frac{2m_4}{\Delta_1} & 0 & 0 & \frac{2m_4}{\Delta_1} & 0 & \frac{2m_4}{\Delta_1} \\ 0 & \frac{1}{m_2} & 0 & 0 & 0 & 0 \\ 0 & 0 & \frac{1}{m_2} & 0 & 0 & 0 \\ \frac{3m_2}{2\Delta_1} & 0 & 0 & \frac{9\Delta_2}{4m_4\Delta_1} & 0 & -\frac{3\Delta_3}{4m_4\Delta_1} \\ 0 & 0 & 0 & 0 & \frac{3}{m_4} & 0 \\ \frac{3m_2}{2\Delta_1} & 0 & 0 & -\frac{3\Delta_3}{4m_4\Delta_1} & 0 & \frac{9\Delta_2}{4m_4\Delta_1} \end{pmatrix} \tag{4.18}$$

Where

$$\begin{cases} \Delta_1=(2m_0m_4-3m_2^2) \\ \Delta_2=(2m_0m_4-m_2^2) \\ \Delta_3=(m_0m_4-3m_2^2) \end{cases} \tag{4.19}$$

And Δ is the determinant of N_{ij}, which is expressed as

$$\Delta=\frac{4}{27}(2m_0m_4)^2(2m_0m_4-3m_2^2) \tag{4.20}$$

Therefore, equation(4.13) can be rewritten as

$$p(\xi_1\ldots\xi_6)=(2\pi)^{-3}\Delta^{-\frac{1}{2}}\exp(-\frac{1}{2}\begin{pmatrix} \frac{2m_4}{\Delta_1}\xi_1^2+\frac{9\Delta_4}{4m_4\Delta_1}(\xi_4^2+\xi_6^2)+\frac{3}{m_4}\xi_5^2+ \\ \frac{3m_2}{\Delta_1}\xi_1(\xi_4+\xi_6)+\frac{3\Delta_3}{2m_4\Delta_1}\xi_4\xi_6+\frac{1}{m_2}(\xi_2^2+\xi_3^2) \end{pmatrix}) \tag{4.21}$$

4.2 Asperity contact height and curvature probability distribution

When two asperities contact each other, the sum of their heights yields the local summit, as shown in Figure 4.2. The probability of height of the composite topography is given as

$$p_{ac}(\xi_1)d\xi_1 = d\xi_1 \int_{-\infty}^{\infty}\int_{-\infty}^{\infty}\int_{-\infty}^{\infty}\int_{-\infty}^{\infty}\int_{-\infty}^{\infty} p(\xi_1,\xi_2,\xi_3,\xi_4,\xi_5,\xi_6)d\xi_2 d\xi_3 d\xi_4 d\xi_5 d\xi_6 \qquad (4.22)$$

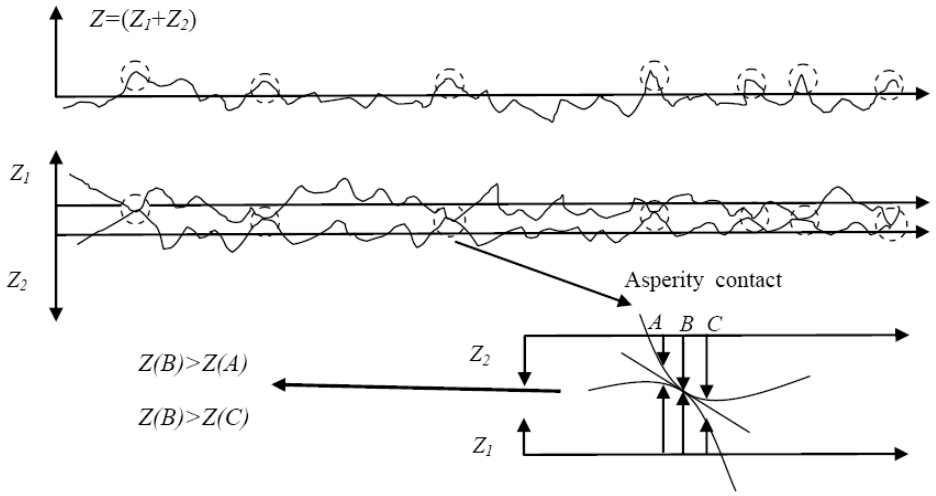

Figure 4.2: Asperity contact conditions.

Furthermore, the condition for the local summit is

$$\begin{cases} \xi_2 = \xi_{21} + \xi_{22} = 0 \\ \xi_3 = \xi_{31} + \xi_{31} = 0 \\ \xi_4 < 0, \xi_6 < 0, \xi_4\xi_6 - \xi_5^2 \geq 0 \end{cases} \qquad (4.23)$$

For further derivation we note that ξ_2 and ξ_3 are functions of x and y, therefore

$$d\xi_2 d\xi_3 = \begin{vmatrix} \dfrac{\partial\xi_2}{\partial x} & \dfrac{\partial\xi_2}{\partial y} \\ \dfrac{\partial\xi_3}{\partial x} & \dfrac{\partial\xi_3}{\partial y} \end{vmatrix} dxdy = \left(\xi_4\xi_6 - \xi_5^2\right) dA \qquad (4.24)$$

Substituting equation (4.24) into equation (4.22) and integrating over the spatial domain (x, y) and considering the conditions expressed in equation (4.23), the probability of asperity contact is found to be

$$p_{ac}(\xi_1)d\xi_1 = d\xi_1 \iiint_V p(\xi_1, 0, 0, \xi_4, \xi_5, \xi_6)\left|\xi_4\xi_6 - \xi_5^2\right| d\xi_4 d\xi_5 d\xi_6 \qquad (4.25)$$

where V indicates the integration should satisfy the condition expressed in equation (4.23).

We note that equation(4.25) has the same form as that of Nayak although we consider two surfaces. For completeness we write out all the derivation here. From equation (4.25), we have

$$p_{ac}(\xi_1) = \frac{\exp(-m_4\xi_1^2/\Delta_1)}{(2\pi)^3\Delta^{1/2}} \times \iiint_V \left|\xi_4\xi_6 - \xi_5^2\right| \exp\left(\begin{array}{l} \frac{-9\Delta_4}{9m_4\Delta_1}(\xi_4^2+\xi_6^2) - \frac{3}{2m_4}\xi_5^2 - \\ \frac{3m_2}{2\Delta_1}\xi_1(\xi_4+\xi_6) + \frac{3\Delta_3}{4m_4\Delta_1}\xi_4\xi_6 \end{array} \right) d\xi_4 d\xi_5 d\xi_6$$

(4.26)

We define

$$\begin{cases} \alpha = \dfrac{m_0 m_4}{m_2^2} \\ C_1 = \dfrac{\alpha}{2\alpha - 3} \\ C_2 = C_1\left(\dfrac{12}{\alpha}\right)^{1/2} \end{cases} \qquad (4.27)$$

And make the following substitution to simplify the integration [82]

$$(s, r\cos\theta, r\sin\theta) = \left(\frac{3}{m_4}\right)^{1/2} \left(1/2(\xi_4+\xi_6), \quad \xi_5, \quad 1/2(\xi_4-\xi_6)\right) \qquad (4.28)$$

Thus, equation(4.26) can be rewritten as

$$p_{ac}(\xi_1, s, r, \theta) = \frac{m_4\sqrt{C_1}}{24m_2\sigma\pi^3}\exp(-C_1\frac{\xi_1^2}{\sigma^2})\left|s^2 - r^2\right| r\exp\left(-\frac{1}{2}(C_1 s^2 + r^2 + C_2 s\frac{\xi_1}{\sigma})\right) \qquad (4.29)$$

After integration with θ=(0,2π), equation (4.29) can be rewritten as

$$p_{ac}(\xi_1, s, r) = \frac{m_4\sqrt{C_1}}{12m_2\sigma\pi^2}\exp(-C_1\frac{\xi_1^2}{\sigma^2})\left|s^2 - r^2\right| r\exp\left(-\frac{1}{2}(C_1 s^2 + r^2 + C_2 s\frac{\xi_1}{\sigma})\right) \quad (4.30)$$

It is noted that $r^2 < s^2$ since s<0, thus $0<r<-s$. Further, integration with respect to r leads to the joint probability distribution of summit heights, ξ_1, and mean curvature, s:

$$p_{ac}(\xi_1, s) = \frac{m_4\sqrt{C_1}}{12m_2\sigma\pi^2}\exp(-C_1\frac{\xi_1^2}{\sigma^2})\left(s^2 - 2 + 2\exp(-\frac{1}{2}s^2)\right)\exp\left(-\frac{1}{2}(C_1 s^2 + C_2 s\frac{\xi_1}{\sigma}\right)$$

(4.31)

Integrating with respect to ξ_1, we have the probability distribution of mean curvature, s, of the asperity contact

$$p_{ac}(s) = \frac{m_4}{12\pi\sqrt{\pi}m_2}\exp(-\frac{1}{4}s^2)\left(s^2 - 2 + 2\exp\left(-\frac{1}{2}s^2\right)\right) \quad (4.32)$$

Further integration with s, yields the density of the summit, N, which is

$$N = \int_{-\infty}^{0} p_{ac}(s)ds = \frac{m_4}{6\pi\sqrt{3}m_2} \quad (4.33)$$

Thus the density function of summit curvature can be obtained via

$$p_{acd}(s) = \frac{p_{ac}(s)}{N} = \frac{\sqrt{3}}{2\sqrt{\pi}}\exp(-\frac{1}{4}s^2)\left(s^2 - 2 + 2\exp\left(-\frac{1}{2}s^2\right)\right) \quad (4.34)$$

The density function of summit radius of curvature denoted by, R, can be obtained from equation (4.34) by making the following variable change

$$R = -\left(\frac{m_4}{3}\right)^{1/2}\frac{1}{s} \quad (4.35)$$

to obtain

$$p_{acd}(R)=\frac{3}{2R^4\sqrt{\pi m_4^3}}\exp(-\frac{3}{4m_4R^2})\left(2m_4R^2-3-2m_4R^2\exp(-\frac{3}{2m_4R^2})\right) \quad (4.36)$$

The expectation of summit radius of curvature denoted by, R_m, is thus given as

$$R_m=\frac{3\left(2-\ln(3)\right)}{2\sqrt{\pi m_4}}\approx\frac{0.76}{\sqrt{m_4}} \quad (4.37)$$

Integrating with respect to *s* in equation(4.31) and divided by *N*, we have asperity contact summit height density function

$$p_{acd}(\xi_1)=\frac{\sqrt{3}}{2\pi\sigma}\left\{\begin{array}{l} e^{-c_1\frac{\xi_1^2}{\sigma^2}}\frac{\xi_1}{\sigma}\left[\frac{3(2\alpha-3)}{\alpha^2}\right]^{1/2}+\frac{3\sqrt{2\pi}}{2\alpha}e^{-\frac{1}{2}\frac{\xi_1^2}{\sigma^2}}(1+erf\,\beta)(\frac{\xi_1^2}{\sigma^2}-1) \\ +\sqrt{2\pi}\left[\frac{\alpha}{3(\alpha-1)}\right]^{1/2}\exp\left\{-\left[\alpha\frac{\xi_1^2}{\sigma^2}/(2(\alpha-1))\right]\right\}(1+erf\,\lambda) \end{array}\right\} \quad (4.38)$$

$$\left\{\begin{array}{l} \beta=\left[\frac{3}{2(2\alpha-3)}\right]^{1/2}\frac{\xi_1}{\sigma} \\ \gamma=\left[\frac{\alpha}{2(\alpha-1)(2\alpha-3)}\right]^{1/2}\frac{\xi_1}{\sigma} \end{array}\right. \quad (4.39)$$

The expectation of asperity contact height can be obtained from equation(4.38) as $(16\sigma/\alpha\pi)^{1/2}$. For further discussion, we consider shifted asperity contact height $r=r_m-\xi_1$ and radius of curvature *R*, to find *H(r,R)* as follows

$$H(r,R)=\frac{3\sqrt{C_1}}{2\sigma\pi R^2\sqrt{m_4}}\left\{\begin{array}{l} \exp(-C_1\frac{\left(r_m-r\right)^2}{\sigma^2})\left(\frac{3}{m_4R^2}-2+2\exp(\frac{-3}{2m_4R^2})\right) \\ \exp\left(\frac{\sqrt{3}C_2}{2R\sqrt{m_4}}\frac{r_m-r}{\sigma}-\frac{3C_1}{2m_4R^2}\right) \end{array}\right\} \quad (4.40)$$

where r_m is highest point of composite topography. And $H_r(r)$ is expressed as

$$H_r(r)=\frac{-\sqrt{3}}{2\pi\sigma}\left\{\begin{array}{l} e^{-c_1\frac{(r_m-r)^2}{\sigma^2}}\frac{(r_m-r)}{\sigma^2}\left[\frac{3(2\alpha-3)}{\alpha^2}\right]^{1/2}+\frac{3\sqrt{2\pi}}{2\alpha}e^{-\frac{1}{2}\frac{(r_m-r)^2}{\sigma^2}}(1+erf\,\beta_1)(\frac{(r_m-r)^2}{\sigma^2}-1) \\ +\sqrt{2\pi}\left[\frac{\alpha}{3(\alpha-1)}\right]^{1/2}\exp\left\{-\left[\alpha\frac{(r_m-r)^2}{\sigma^2}/(2(\alpha-1))\right]\right\}(1+erf\,\lambda_1) \end{array}\right\} \quad (4.41)$$

where

$$\left\{\begin{array}{l} \beta_1=\left[\frac{3}{2(2\alpha-3)}\right]^{1/2}\frac{r_m-r}{\sigma} \\ \gamma_1=\left[\frac{\alpha}{2(\alpha-1)(2\alpha-3)}\right]^{1/2}\frac{r_m-r}{\sigma} \end{array}\right. \quad (4.42)$$

4.3 Asperity contact orientation distribution

As we have shown before, the asperity slope is independent of the surface height and curvature. Thus for surface 1, the slope distribution can be expressed as

$$p_1(\xi_{21},\xi_{31})=\frac{1}{2\pi\Delta_2^{1/2}}\exp\left[\left(-m_{02}\xi_{21}^2-2m_{11}\xi_2\xi_3+m_{20}\xi_3^2\right)/2\Delta_2\right] \quad (4.43)$$

Or in a simplified form for isotropic surfaces (m_{11}=0) as follows

$$p_1(\xi_{21},\xi_{31})=\frac{1}{2\pi M_{21}}\exp\left[-\left(\xi_{21}^2+\xi_{31}^2\right)/M_{21}\right] \quad (4.44)$$

Where $M_{21}=2m_{02}=2m_2$. Similarly, the slope distribution for surface 2 can be expressed in the same form,

$$p_2(\xi_{22},\xi_{32})=\frac{1}{2\pi M_{22}}\exp\left[-\left(\xi_{22}^2+\xi_{32}^2\right)/M_{22}\right] \quad (4.45)$$

Asperity slopes at the asperity contacts will have same magnitude with opposite sign. Thus, the asperity contact orientation is conditional joint distribution of two surfaces given as

$$p(\xi_2 \left| \xi_{21} = -\xi_{22}, \xi_3 \right| \xi_{31} = -\xi_{32}) = \frac{p_1 p_2 (\xi_{22} = -\xi_{21}, \xi_{32} = -\xi_{31})}{\int_{-\infty}^{\infty} \int_{-\infty}^{\infty} p_1 p_2 d\xi_{21} d\xi_{31}} \tag{4.46}$$

Or

$$p(\xi_2, \xi_3) = \frac{1}{\pi^2 M_{22} M_{21}} \exp\left[-\left(\xi_2^2 + \xi_3^2 \right) / M_{22} - \left(\xi_2^2 + \xi_3^2 \right) / M_{21} \right] / P_{sum} \tag{4.47}$$

where P_{sum} is expressed as

$$P_{sum} = \int_{-\infty}^{\infty} \int_{-\infty}^{\infty} \frac{1}{\pi^2 M_{22} M_{21}} \exp\left[-\left(\xi_2^2 + \xi_3^2 \right) / M_{22} - \left(\xi_2^2 + \xi_3^2 \right) / M_{21} \right] d\xi_2 d\xi_3 = \frac{1}{\pi (M_{22} + M_{21})} \tag{4.48}$$

As a result, the probability density of asperity contact slope is given as

$$p(\xi_2, \xi_3) = \frac{M_{22} + M_{21}}{\pi M_{22} M_{21}} \exp\left[-\left(\xi_2^2 + \xi_3^2 \right) / M_{22} - \left(\xi_2^2 + \xi_3^2 \right) / M_{21} \right] \tag{4.49}$$

Now we use the spherical coordinate written as

$$\begin{cases} \xi_2 = \tan\theta \cos\phi \\ \xi_3 = \tan\theta \sin\phi \end{cases} \tag{4.50}$$

such that the transformation is related though the jacobian as:

$$d\xi_2 d\xi_3 = \begin{vmatrix} \frac{\partial \xi_2}{\partial \theta} & \frac{\partial \xi_2}{\partial \phi} \\ \frac{\partial \xi_3}{\partial \theta} & \frac{\partial \xi_3}{\partial \phi} \end{vmatrix} d\theta d\phi = \frac{\tan\theta}{\cos^2 \theta} d\theta d\phi \tag{4.51}$$

Thus, the asperity contact orientation density function in spherical coordinates can be derived by applying the coordinate transformation as

$$\xi(\theta,\phi)d\theta d\phi = p(\xi_2,\xi_3)d\xi_2 d\xi_3 \tag{4.52}$$

which yields:

$$\xi(\theta,\phi) = \frac{\tan\theta}{\chi\pi\cos\theta^2}\exp(-\frac{\tan\theta^2}{\chi}) \tag{4.53}$$

Where

$$\chi = \frac{M_{22}M_{21}}{M_{22}+M_{21}} \tag{4.54}$$

It is noted that χ is the expectation of $\xi_2^2+\xi_3^2$.

This page left intentionally blank.

Chapter 5 Rough Contact Behavior Based on Statistical Method

In last chapter, we discussed the statistical parameters of contacting surfaces. For the description of contacting surface, three parameters are considered important: (1) the asperity contact height distribution which will affect the number of asperity contacts; (2) the asperity contact radii distribution which directly affects the asperity contact stiffness according the Hertz-Mindlin theory; and (3) asperity contact orientation distribution which affects coupling effect on shear and normal direction. The statistical approach is to sum the local behavior to get interface response. In this chapter, a statistical model is proposed to study the normal and shear behavior of contacting surfaces.

5.1 Methodology

The statistical model can be considered as a homogenization method in which the local behavior contributes the global interface behavior via its probability. In other words, global force is sum of the weighted local force, i.e., asperity contact force. The weight of local force is determined by its height, curvature and orientation. Simultaneously, the local behavior obeys the displacement consistency. As we can see in Figure 5.1, when two surfaces are approaching, whether they are in contact or not depends upon the asperity contact height of the location. It is noted here asperity contact height is the sum of the two corresponding contacting asperity heights. But how they are in contact depends upon the orientation and their curvatures. As we have discussed in chapter 4, we

know asperity contact height and curvature are correlated with each other, while the orientation is independent. For simplicity, we take the highest asperity contact as the *r=0* plane as shown in Figure 5.2.

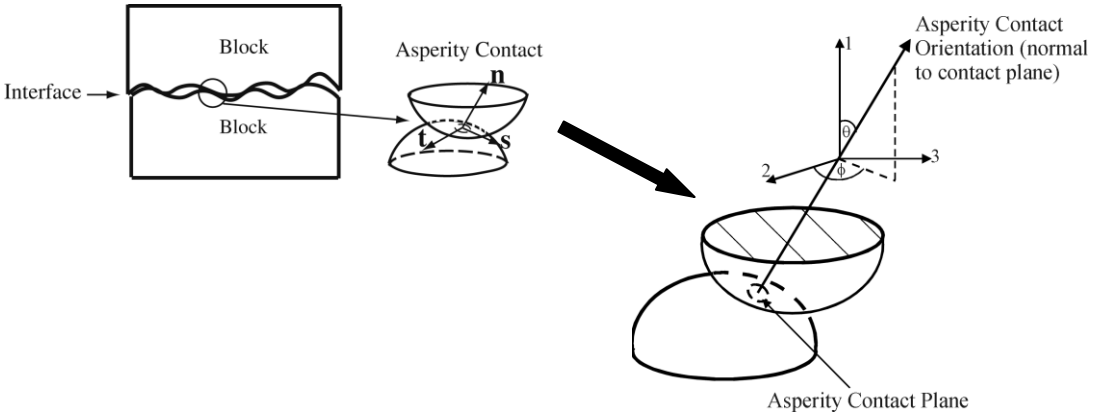

Figure 5.1: Sketch of the global coordinate and local coordinate.

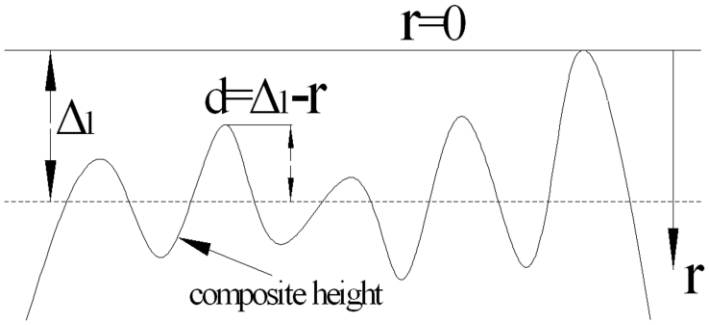

Figure 5.2: Asperity contact height in global coordinate.

5.2 Micromechanical stress-displacement relationship

For displacement consistency, we assume that the asperity contact displacement, δ_j, at a given asperity contact height is the same and directly related to the overall displacement of the interface, Δ_j. The subscripts in this chapter follow the established tensor convention unless specified otherwise. Under this kinematic assumption, the asperity

contact displacement in the local coordinate system can be written in terms of the overall interface displacements as follows:

$$\begin{Bmatrix} \delta_n \\ \delta_s \\ \delta_t \end{Bmatrix} = \begin{bmatrix} n_1 & n_2 & n_3 \\ s_1 & s_2 & s_3 \\ t_1 & t_2 & t_3 \end{bmatrix} \begin{Bmatrix} \Delta_1 - r \\ \Delta_2 \\ \Delta_3 \end{Bmatrix} \tag{5.1}$$

where δ_n is the asperity contact normal displacement, while δ_s and δ_t are the asperity contact shear displacements resolved along the local coordinate axes. The local Cartesian coordinate system is formed by the normal vector, ***n***, shown in Figure 5.1, and vectors, ***s*** and ***t*** chosen arbitrarily on the plane tangential to the asperity contact surface, such that the vectors ***n,s,t*** are given as follows:

$$\begin{aligned} n_i &= \langle \cos\theta, \quad \sin\theta\cos\phi, \quad \sin\theta\sin\phi \rangle \\ s_i &= \langle -\sin\theta, \quad \cos\theta\cos\phi, \quad \cos\theta\sin\phi \rangle \\ t_i &= \langle 0, \quad -\sin\theta, \quad \cos\phi \rangle \end{aligned} \tag{5.2}$$

Therefore, for a normal interface displacement Δ_1, the displacement of the asperity contact at height r is Δ_1-r as shown in Figure 5.2. This kinematic assumption disregards the nonlocality of asperity contact interactions. The assumption is reasonable for interfaces with relatively large asperity contact spacing in stiff materials such that the overlap of deformation fields associated with neighboring asperity contacts is minimal and the statistical description of the interface remains unchanged during loading. This assumption has been widely used and appears to be especially useful for describing contacts between metals and stiff geomaterials, such as rock joints [6, 25]. In some cases,

however, the asperities may undergo damage. The consequent change in the interface geometry has to be appropriately modeled[57].

5.2.1 Asperity contact force-displacement relationship

In local coordinate system, considering the Hertz-Mindlin contact theory of perfectly smooth elastic interfaces as well as other theories of smooth elastic-plastic interfaces[64], it is reasonable to assume that normal asperity contact stiffness K_n depends on the normal asperity contact displacement δ_n according to the following power law:

$$f_n = K_n \delta_n = \lambda K \delta_n^{\eta+1} \tag{5.3}$$

Where δ_n is the magnitude of normal compression at the asperity contact, and K, λ and η are constants. The asperity contact stiffness, K_n given by equation(5.3), becomes identical with the Hertz stiffness for contact of perfectly smooth elastic spheres when

$$\lambda = \frac{2-\nu}{2(1-\nu)}; \quad \eta = \frac{1}{2}; \quad K = \frac{8G\sqrt{R}}{3(2-\nu)} \tag{5.4}$$

where G is the shear modulus, ν is Poisson's ratio and R is asperity contact radius of curvature. It is noteworthy that the exponent η can vary from 0 for perfectly plastic to ½ for perfectly elastic behavior at contact of perfectly smooth spherical asperities[64]. In addition, the asperity contact area, a_c, for the Hertzian contact is given as:

$$a_c = \pi \delta_n R \tag{5.5}$$

The asperity contact loading in the tangential direction is complicated when an interface is subjected to a sequential loading in which an interface is first subjected to a normal closure followed by shearing as is typically done in laboratory experiments. In this case, the inclined asperity contacts first experience tangential loading along specific directions (determined by their orientations) as the interface is subjected to normal closure. Subsequently upon the application of shear loading, the asperity contacts may experience unloading or loading with changed obliquity and out-of-plane tangential loading. Chapters 2 and 3 examined in detail the consequences of unloading, changing obliquity and out-of-plane loading. It was shown that hysteretic loop may form during such unloading or out-of-plane loading, which represent a loss of energy at the asperity contact while the overall interface is subjected to loading. The complete loading history of each asperity contact must be strictly followed to determine the true tangential traction, slip annulus and the resultant tangential force-displacement behavior as described in Chapter 2 and 3. Clearly, such an approach will entail additional computational efforts. For the case of monotonic shear loading subsequent to normal loading considered in this chapter, the effect of obliquity change and out-of-plane at individual asperity contact are expected to be small as seen from Figure 3.6. Therefore, for our calculations we have considered the case of constant normal asperity contact force and monotonically increasing asperity

contact shear force, such that the asperity contact shear force-displacement relationship is given as:

$$f_{st} = \mu K_n \delta_n \left[1 - (1 - \frac{\delta_{st}}{\lambda \mu \delta_n})^{\frac{3}{2}} \right] \tag{5.6}$$

Where f_{st} is the asperity contact shear force and δ_{st} is the asperity contact shear displacement given by,

$$\delta_{st} = \sqrt{\delta_s^2 + \delta_t^2} \tag{5.7}$$

Thus, in *s* and *t* direction, we have the following force displacement relationship:

$$f_s = f_{st} \frac{\delta_s}{\delta_{st}} = \mu K_n \frac{\delta_n}{\delta_{st}} \left[1 - (1 - \frac{\delta_{st}}{\lambda \mu \delta_n})^{\frac{3}{2}} \right] \delta_s = K_s \delta_s \tag{5.8}$$

$$f_t = f_{st} \frac{\delta_t}{\delta_{st}} = \mu K_n \frac{\delta_n}{\delta_{st}} \left[1 - (1 - \frac{\delta_{st}}{\lambda \mu \delta_n})^{\frac{3}{2}} \right] \delta_t = K_t \delta_t \tag{5.9}$$

where K_s and K_t are stiffness in s and t directions, respectively. We note equations. (5.8) and (5.9) are valid when $\lambda \mu \delta_n > \delta_{st}$. When this condition is violated, sliding occurs at the contact per the Amonton–Coulomb's friction law. In this case, equations. (5.8) and (5.9) can be rewritten as:

$$f_s = \mu K_n \frac{\delta_n}{\delta_{st}} \delta_s = K_s \delta_s \tag{5.10}$$

$$f_t = \mu K_n \frac{\delta_n}{\delta_{st}} \delta_t = K_t \delta_t \tag{5.11}$$

Thus, for a single asperity contact the force-displacement can be written in the following matrix form in the local coordinate system:

$$\begin{Bmatrix} f_n \\ f_s \\ f_t \end{Bmatrix} = \begin{bmatrix} K_n & 0 & 0 \\ 0 & K_s & 0 \\ 0 & 0 & K_t \end{bmatrix} \begin{Bmatrix} \delta_n \\ \delta_s \\ \delta_t \end{Bmatrix} \tag{5.12}$$

Or in the global coordinate system, the asperity contact forces, f_i, and displacements, δ_j, are related as follows:

$$\begin{Bmatrix} f_1 \\ f_2 \\ f_3 \end{Bmatrix} = \begin{bmatrix} K_{11} & K_{12} & K_{13} \\ K_{12} & K_{22} & K_{23} \\ K_{13} & K_{23} & K_{33} \end{bmatrix} \begin{Bmatrix} \Delta_1 - r \\ \Delta_2 \\ \Delta_3 \end{Bmatrix} \quad or \quad f_i = K_{ij}\left(\Delta_j - \delta_{1j} r\right) \tag{5.13}$$

Where the asperity contact stiffnesses, K_{ij}, given by:

$$K_{ij} = K_n n_i n_j + K_s s_i s_j + K_t t_i t_j \tag{5.14}$$

where K_n, K_s and K_t denote asperity contact stiffness along the *n*, *s* and *t* direction of the asperity contact.

5.2.2 Interface contact force-displacement and force-contact area relationship

At a rough interface, numerous asperity contacts of varying height overlap and orientations occur under a given loading condition. These asperity contacts can be classified into three groups: (1) those in contact but without sliding, (2) those in contact but with sliding, and (3) those not in contact. The overall interface stress can be obtained as the sum of the asperity contact forces contributed by groups (1) and (2). Utilizing the orientation distribution and height distribution introduced in chapter 4, we obtain the following expression for the overall interface stress:

$$F_i = N\begin{pmatrix} \int_{r^{el}}\int_{R^{el}}\int_{\Omega^{el}} f_i^{el}\xi(\theta,\phi)d\theta d\phi H(r,R)drdR \\ +\int_{r^{p}}\int_{R^{p}}\int_{\Omega^{p}} f_i^{p}\xi(\theta,\phi)d\theta d\phi H(r,R)drdR \end{pmatrix} \tag{5.15}$$

where the superscript e denotes the domain and forces of asperity contacts that are not sliding, the superscript p denotes the domain and forces of asperity contacts experiencing sliding, and $\Omega=(\theta,\phi)$. Similarly, the contact area can be obtained as follows:

$$A_i = N\left(\int_r\int_R\int_\Omega a_c n_i \xi(\theta,\phi)d\theta d\phi H(r,R)drdR\right) \tag{5.16}$$

where A_i is the projection of contact area in the interface coordinate directions and the nominal contact area is defined as the total contact area denoted by A_c.

5.3 Numerical implementation for nonlinear force-displacement relationship

Based on the expression derived above, if the overall interface displacements are known, the overall interface stresses can be calculated directly from equation(5.15). However, the loading conditions utilized during laboratory testing of interfaces or for computations involving fractured bodies are in many cases specified either in terms of stresses or a mix of stresses and displacement. If the stress loading conditions or mixed loading conditions are given, we have to solve the nonlinear equation system given by equation(5.15) to obtain the corresponding displacements. In this section, we utilize the Newton-Raphson method to solve this set of nonlinear equations. For further discussion, equation(5.15) is rewritten as

$$R_i\left(\Delta_i\right) \equiv N\left(\begin{array}{l}\int_{r^{el}}\int_{R^{el}}\int_{\Omega^{el}} f_i^{el}\xi(\theta,\phi)d\theta d\phi H(r,R)drdR \\ +\int_{r^{p}}\int_{R^{p}}\int_{\Omega^{p}} f_i^{p}\xi(\theta,\phi)d\theta d\phi H(r,R)drdR\end{array}\right) - F_i^E = 0 \qquad (5.17)$$

where $R_i\,(\Delta_i)$ is the residual vector, F_i^E is understood as the external force vector. We expand the residual $R_i\,(\Delta_i)$ in Taylor's series with respect to displacement vector Δ_i at (n-1)th iteration to obtain:

$$R_j\left(\Delta_i\right) = R_j\left(\Delta_i\right)^{n-1} + \left(\frac{\partial R_j}{\partial \Delta_i}\right)^{n-1} d\Delta_i + \ldots \qquad (5.18)$$

where we omit the terms of order 2 and higher. Now, using equation(5.18) we get

$$\left(T_{ji}\right)^{n-1} d\Delta_i = -R_j\left(\Delta_i\right)^{n-1} \qquad (5.19)$$

where T_{ji} is recognized as the tangent stiffness tensor given as,

$$\left(T_{ji}\right)^{n-1} = \left(\frac{\partial R_j}{\partial \Delta_i}\right)^{n-1} \qquad (5.20)$$

We can thus obtain the increment of displacement, $d\Delta_i$, corresponding to the residual at the (n-1)th iteration as

$$d\Delta_i = \frac{-R_j\left(\Delta_i\right)^{n-1}}{\left(T_{ji}\right)^{n-1}} \qquad (5.21)$$

and, subsequently, update the interface displacement in the usual manner

$$\left(\Delta_i\right)^n = \left(\Delta_i\right)^{n-1} + d\Delta_i \qquad (5.22)$$

The above numerical scheme has been implemented as follows:

Step 1: Discretize the integration domain in equation(5.17) into sufficient points representing asperity contact heights and orientations so as to obtain a converged solution.

For our computations we have used $\Delta r = 0.01 r_{90}$, where r_{90} is the 90th percentile of asperity contact height for r-discretization, and grid of 20x40 for θ and ϕ-discretization. The integration is performed using Simpson's rule.

Step 2: Use the (n-1)th iteration displacement $(\Delta_i)^{n-1}$ to determine sliding condition of each contact point and sum all of the forces of contacts points to obtain the overall force, $(F_i)^{n-1}$, using discretized equation(5.15).

Step 3: Use a small interface displacement increment, $\partial\Delta_i$, typically taken as $0.01 r_{90}$, to compute the corresponding increment of interface force, ∂F_j, following step 2 and evaluate tangential stiffness $\left(T_{ji}\right)^{n-1} = \left(\frac{\partial F_j}{\partial \Delta_i}\right)^{n-1}$.

Step 4: Calculate the residual force $R_j^{n-1} = F_j^E - (F_j)^{n-1}$, and use equation (5.21) to find the interface displacement increment, $d\Delta_i$. Update the interface displacement $(\Delta_i)^n$ and check for convergence.

In the subsequent sections, we demonstrate the applicability of the derived overall stress-displacement relationship and its numerical implementation under a variety of loading conditions.

5.4 Sliding behavior of asperity contacts at different orientations

Here we discuss the sliding behavior of asperity contacts subjected to a combined normal and shear displacement. We consider asperity contacts with different orientations at the same asperity contact height, r. We note that the asperity contact orientation are defined

by θ and ϕ and forms a hemi-spherical surface. As we discussed before, asperity contacts with the same height r experience the same global displacements Δ_1-r, Δ_2 and Δ_3. However, the local displacements δ_n, δ_s and δ_t which determine the sliding behavior of asperity contacts are different since these are functions of contact orientations. For simplicity but without loss of generality, let us consider the asperity contacts subjected to the exterior displacement that lies on the 1-3 plane of the global coordinate system and makes an oblique loading angle, ω, with 1-axis. In this case, the asperity contacts of height, r, will experience a displacement of $(\Delta_1 - r) = d$, in the direction of 1-axis and a displacement of $\Delta_2 = 0$ and $\Delta_3 = d \tan(\omega)$ in the directions of 2- and 3-axis, respectively The asperity contact displacement in the local coordinate system can then be written as follows based on equation(5.1):

$$\begin{cases} \delta_n = d\cos(\theta) + d\tan(\omega)\sin(\theta)\sin(\varphi) \\ \delta_s = -d\sin(\theta) + d\tan(\omega)\sin(\theta)\sin(\varphi) \\ \delta_t = r\tan(\omega)\cos(\varphi) \end{cases} \tag{5.23}$$

Using these expressions for asperity contact displacement, we can determine whether a contact is in sliding condition. To this end, we discretize the asperity contact orientation domain into various asperity contact directions denoted by the pair (θ_i, ϕ_i). For each asperity contact direction, we evaluate the local displacement using equation(5.23). When the normal displacement, $\delta_n(\theta_i, \phi_i) < 0$, no contact exists; when the normal displacement, $\delta_n(\theta_i, \phi_i) > 0$, and the shear displacement, $\delta_{st}(\theta_i, \phi_i) < \mu\lambda\delta_n(\theta_i, \phi_i)$, contact

exists, however is not sliding. Finally when the normal displacement, $\delta_n(\theta_i, \phi_i) > 0$, and the shear displacement, $\delta_{st}(\theta_i, \phi_i) \geq \mu\lambda\delta_n(\theta_i, \phi_i)$, contact experiences sliding. An extensive numerical search is performed using these criteria to define the asperity contact orientation groups as no-contact area, no-sliding area, or sliding area. In Figure 5.3 and Figure 5.4, we illustrate how the three areas evolve for different ω *and* $\mu\lambda$ respectively. The three areas are plotted on $\theta=0$ plane looking down along the 1-axis. The area designated as no-sliding, given by the closed interior loop, represents the asperity contact orientations that satisfy the no-sliding criterion. The area designated as sliding, given by the space between the no-sliding area and no-contact area, represents the asperity contact orientations that satisfy the sliding criterion. The remaining directions represent asperity contacts that satisfy no-contact criterion. Under normal loading, shown in Figure 5.3(a), all asperity contacts at that height r are in contact, the no-sliding area is centered at $\theta=0^o$ direction and the sliding areas is given by $\theta \geq 45^o$ for the product $\mu\lambda=1$. In Figure 5.3, we observe that the no-sliding area shifts towards $\phi=90^o$ and is centered at $\theta>0^o$ as the interface is subjected to shear along the 3-axis. We find that as we increase the loading angle, ω, the no-sliding domain moves closer to the horizon accompanied by an expanding no-contact area. We also find that the extent of sliding area depends upon the contact parameter given by the product, $\mu\lambda$., as shown in Figure 5.4.

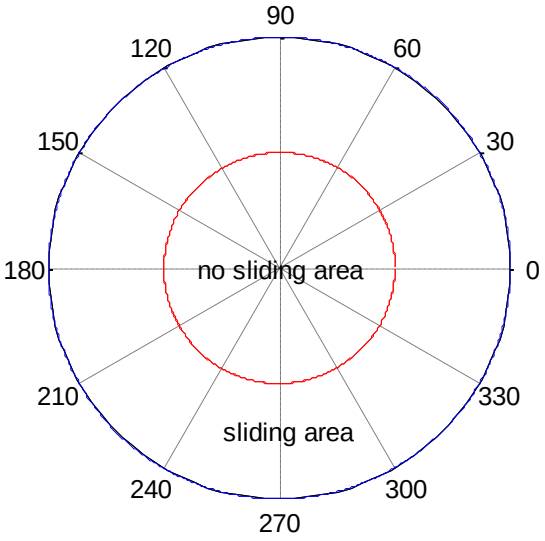

(a) ω=0

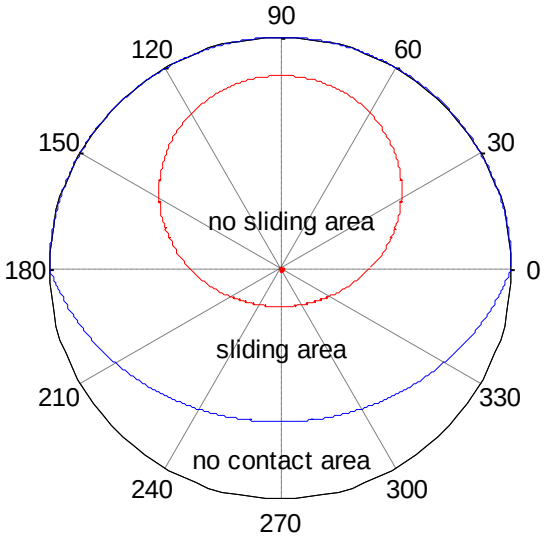

(b) ω=π/6

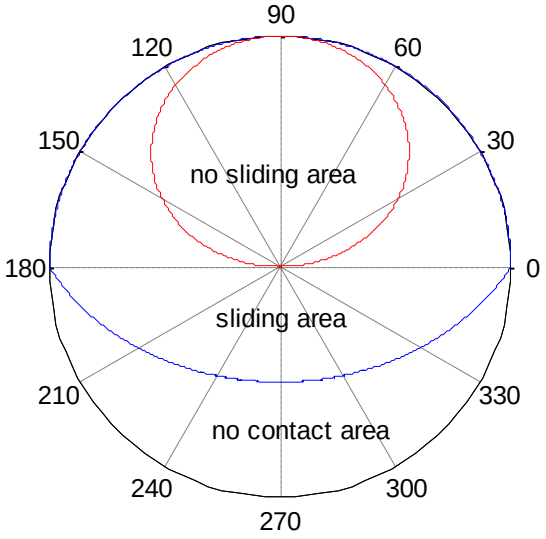

(c) ω=π/4

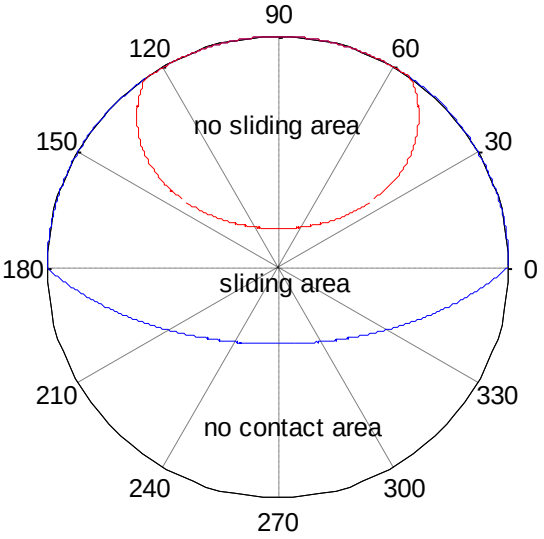

(d) ω=π/3

Figure 5.3: ω effect on sliding and no sliding distribution $\mu\lambda$=1.

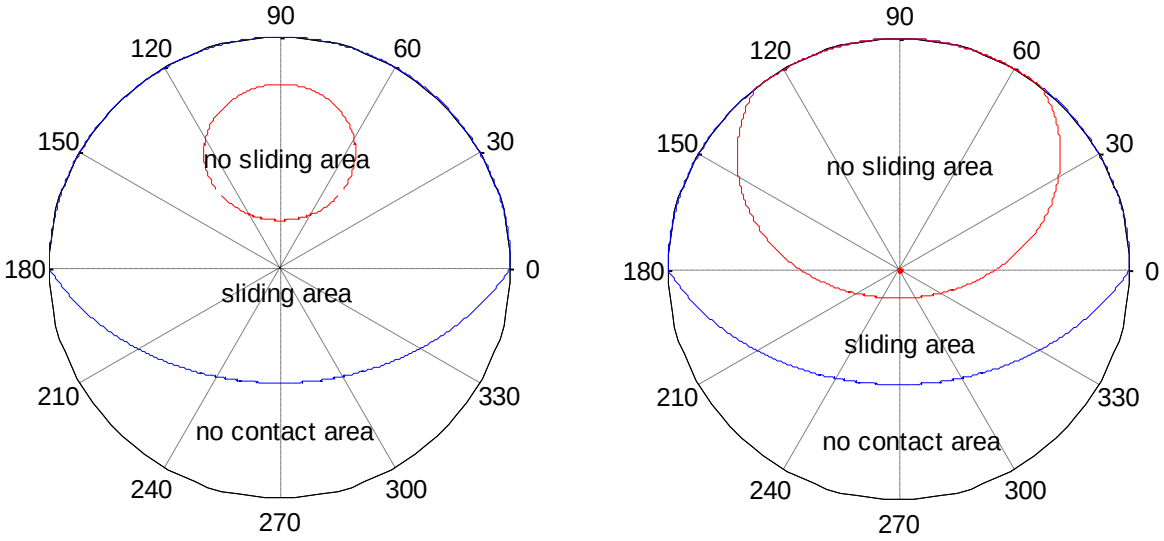

(a) $\mu\lambda$=0.5 (b) $\mu\lambda$=1.5

Figure 5.4: $\mu\lambda$ effect on sliding and no sliding distribution (ω=π/4)

5.5 Interface behavior under normal loading

This section we will study the interface behavior under normal loading. The interface properties used for our example computations are tabulated in Table 1. Correspondingly, the asperity contact height and orientation distributions are shown as Figure 5.5. These parameters are for illustrative purposes and are loosely based upon observations of lab tests on stiff rock, ceramic and metal samples.

Table 1: Interface properties.

Parameters	*R1* (rough)	*S1* (smooth)
m_0	$8/\mu m^2$	4 /mm^2
m_2	0.1	0.05
m_4	8.16E+08/m^2	2.78E+08/m^2
Asperity friction, μ	1	1
Shear modulus, G	8.0 GPa	8.0 GPa
Poisson's ratio, ν	0.3	0.3
χ (χ=2 m_2)	0.2	0.1

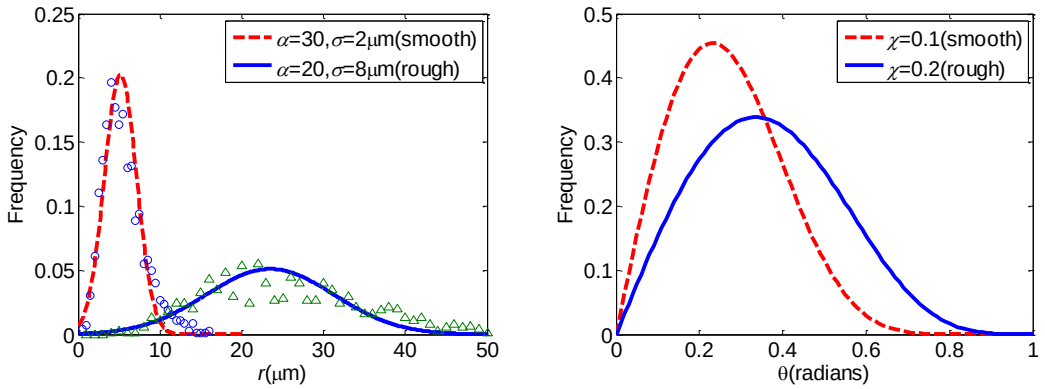

Figure 5.5: Asperity contact height and orientation distribution used in this chapter. Data from Yoshioka and Scholz[27, 28].

In most previous statistical models of rough surface in contact with a plane, such as the G-W model, the radii of curvatures are assumed to be constant. This assumption disagrees with the statistical analysis presented in Chapter 4. Therefore, to evaluate the effect of dependency of asperity contact height and curvature, we present the following computations for both rough surface and smooth surfaces: (1) we use the joint probability function, *H(r,R)*, given in equation(4.40) to consider the dependency of height and curvature, and (2) we use the probability function, $H_r(r)$, given in equation(4.41) while assuming a mean radius of curvature R_m given in equation(4.37).

Figure 5.6 shows the normal force-displacement relationship for the above two cases. It is found that using *H(r,R)* yields almost the same results as that using $H_r(r)$, with less than 5% difference in either rough surface or smooth surface. Thus the choice for a meam R_m is a reasonable simplification as discussed by Greenwood[82]. Moreover, we found that smooth surface has a high stiffness than that of rough surface (see Figure

5.6(a)). We also note that the calculated normal stress-displacement behavior does not follow a power-law behavior with the usual Hertzian exponent of 3/2. Instead, the behavior is highly nonlinear as shown by the nonlinear curve in the log-log plot in Figure 5.6(b). However, the contact area and stress exhibits a quasi-linear relationship, as shown in Figure 5.6(c), which is similar to the results presented by Carbone[79].

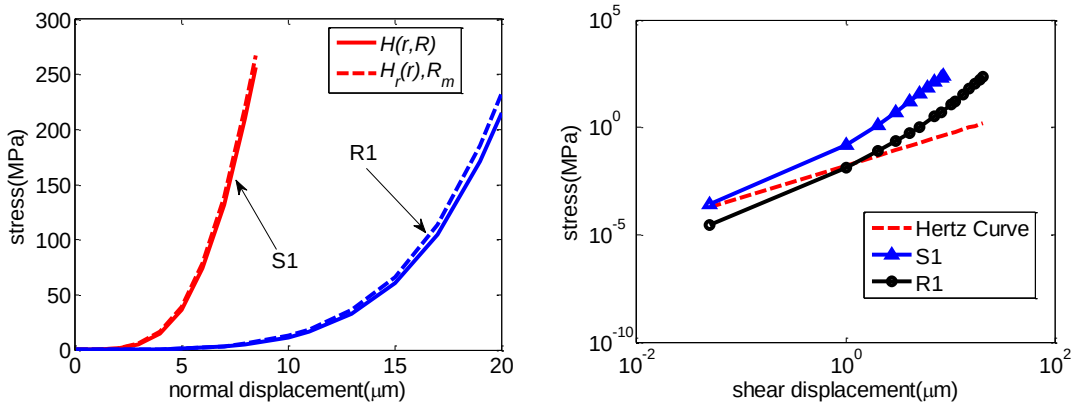

(a) (b)

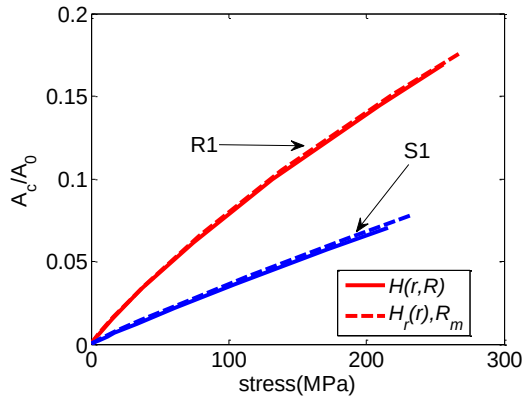

(c)

Figure 5.6: Interface behavior under normal loading.

5.6 Interface behavior under shear loading

For the evaluation of shear behavior prediction, we have computed the result for the rough interface R1 and the smooth interface S1. The calculation is performed under mixed loading condition consisting of two steps. In step 1, we incrementally increase the normal stress to 100 MPa. In step 2, we keep the normal stress constant at 100 MPa and incrementally increase the tangential stress till a substantial number of asperity contacts achieve sliding and the interface can be considered as failed in shear. The results of the step 2 loading are plotted in Figure 5.7-Figure 5.10.

Figure 5.7(a) shows the evolution of shear resistance, defined as the ratio of the interface shear and normal stresses, with shear displacement for smooth and rough interfaces. In Figure 5.7(a) inset, we have included the measurements reported by [83] on interfaces between two smooth or two rough surfaces of Westerly granite blocks. The computed results show qualitative agreement with the measurements. No attempt was made to obtain quantitative agreement due to lack of data for surface roughness parameters.

The difference between the shear behaviors of the smooth and rough interfaces in Figure 5.7(a) may be considered in two distinct regimes of shear displacements. In the small shear displacement regime, we observe that the smooth interface is significantly stiffer in shear compared to the rough interface. Measurements performed on interfaces of same materials but different roughness [27, 83] confirm that smoother interfaces are stiffer.

The stiffer shear response of smooth interface can be attributed to the concentration of asperity contact orientation distribution toward the direction normal to the interface. Under small shear displacements, the effect of applied normal stress is dominant. Therefore, interfaces with larger number of asperity contact in the direction normal to the interface or with a larger real contact area tend to be stiffer. At the large shear displacement regime, we observe that the curves crossover and the rough interfaces are found to have a higher shear resistance, and eventually, a higher frictional strength compared to smooth interfaces.

As the shear loading is increased, a larger proportion of asperity contacts inclined close to the direction normal to the interface begin to slide. Since smooth interfaces have a larger proportion of asperity contacts inclined close to the interface normal direction, the interface exhibits a rather sharp yield point with very little displacement hardening. As seen from Figure 5.7(a), smooth interface reaches a frictional resistance at only 1.7 times of the asperity friction coefficient. In contrast, the rough interface exhibits considerable displacement hardening without a distinct yield point and possesses a significantly higher frictional resistance than the asperity friction coefficient.

The shear behavior is also affected by the strong coupling between normal and shear displacements. In Figure 5.7(b) the closure behavior during interface shear loading is plotted as the normal displacement in step 2 of loading, $d\Delta_1$, versus Δ_2(dilation vs. shear

displacement). Both interfaces first compress before dilating, with the rough interface experiencing greater compression as well as dilation compared to the smooth interface. Although the magnitude of normal displacement is small, it has significant effect upon the displacement hardening and frictional strength of interface.

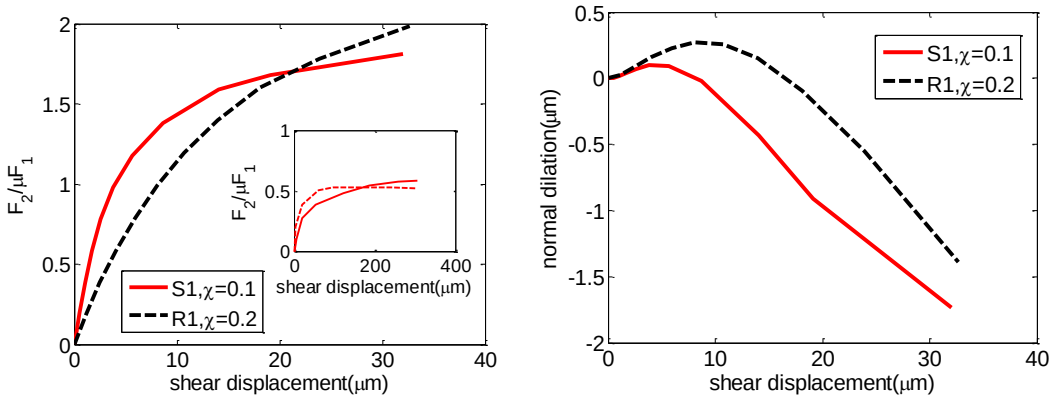

Figure 5.7: Shear behavior under constant normal stress for a rough (R1) and a smooth (S1) interfaces: (a) shear resistance-displacement curves; (b) interface normal dilation curve.

To study the orientation effect, in Figure 5.8(a), we change the value of asperity contact orientation parameter, χ , to 0.3 for the interface S1 for comparison(S1 vs S1). As we can see in Figure 5.8(a), larger χ yields high shear resistance in later loading. This is because small χ contribute more asperity contact close to normal direction, which leads to small displacement hardening in late loading. In this case, when χ=0.3, mean asperity contact inclination is 16.7^{o} ; when χ=0.1,mean asperity contact inclination is 5.7^{o} . Furthermore, dilation curve in Figure 5.8(b) demonstrate the coupling effect tends to small in later loading with small χ.

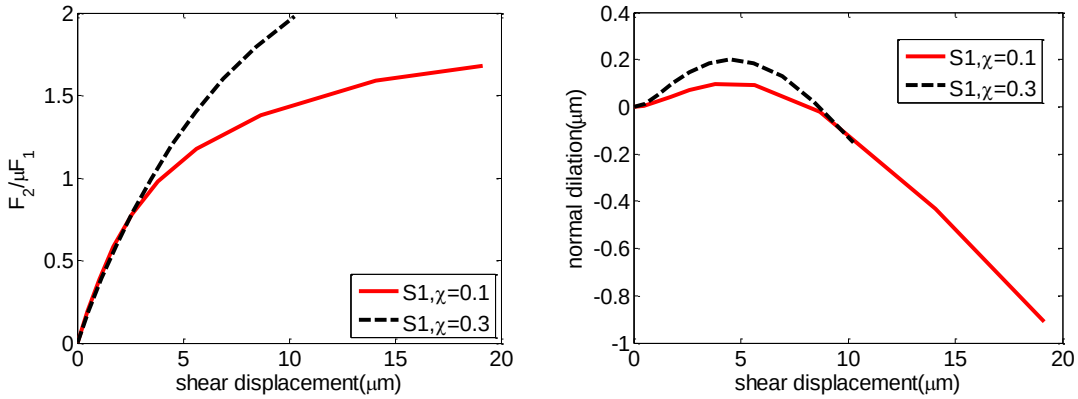

Figure 5.8: (a) Shear resistance-displacement curves under constant normal stress for different orientation with same asperity contact height distributions; (b) Interface normal dilation curve.

In contrast, in Figure 5.9, we change the value of asperity contact orientation parameter, χ , to 0.1 for the interface R1 for comparison(R1 vs. S1). The crossover in the shear resistance-displacement curves is not observed in this case. We note that the asperity contact orientations and heights are a function of the surface topography; consequently for a real interface the parameters for both the roughness measure should change simultaneously. The example presented here demonstrates the significant role asperity contact orientations play in the determination of the overall shear stress-displacement behavior and, particularly, the shear strength behavior of interfaces.

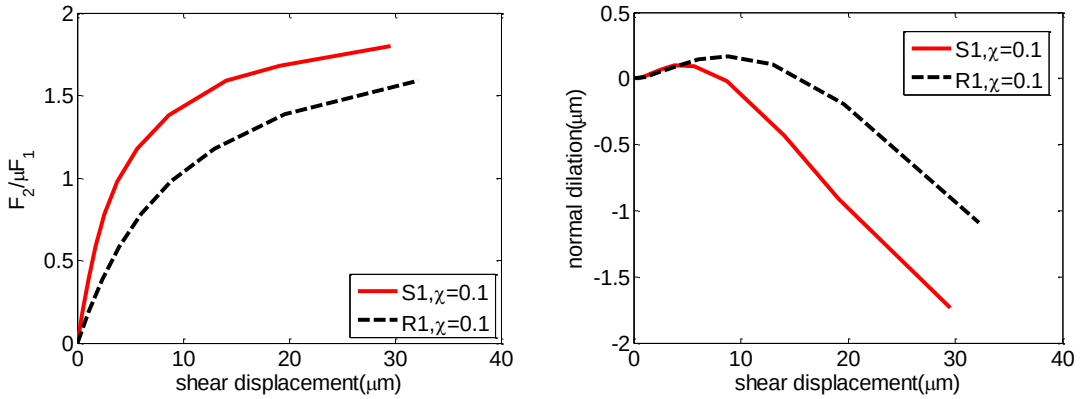

Figure 5.9: (a) Shear resistance-displacement curves under constant normal stress for different height distributions with same asperity contact orientation distributions; (b) Interface normal dilation curve.

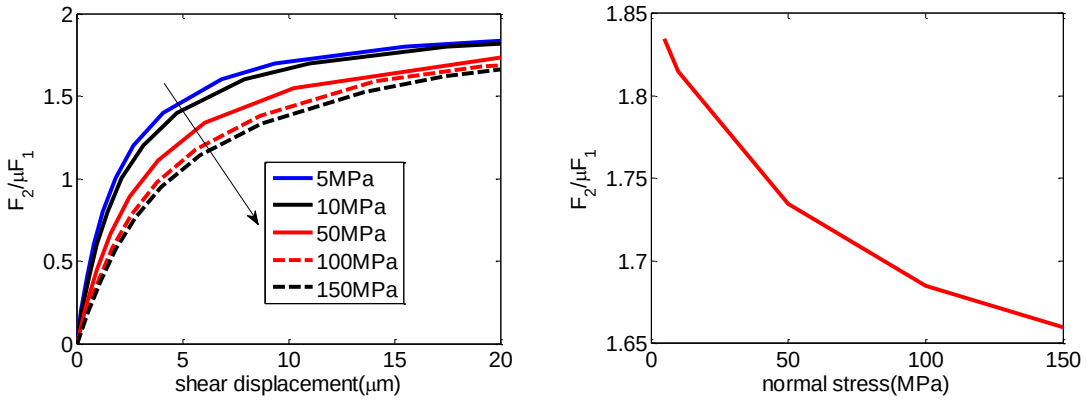

Figure 5.10: (a) Shear resistance-displacement curves under different constant normal stresses; (b) Interface sliding resistance as a function of normal stress.

In Figure 5.10(a), we illustrate the effect of interface normal stress on the shear resistance- displacement behavior. As expected the shear stress close to interface sliding increases with normal stress, however, this increase is nonlinear as shown by the plot of shear resistance versus normal stress in Figure 5.10(b). We find that the shear resistance

decreases (or the effective friction coefficient) decreases with normal stress which is in agreement with experimental studies on interfaces between rock blocks [84].

5.7 Coupling effect between normal and tangential loading

For rough interface, the interaction of normal and tangential loading can be significant. To this end, we have investigated the coupling effect between normal and tangential loading under a 3-step loading path for two interfaces with different roughness (R1 and S1). The interface properties used for our example computations are tabulated in Table 1. As illustrated in Figure 5.11, we first apply a normal displacement, Δ_1, subsequently, we apply a shear displacement in the 2-direction, Δ_2, followed by shear displacement in the 3-direction, Δ_3.

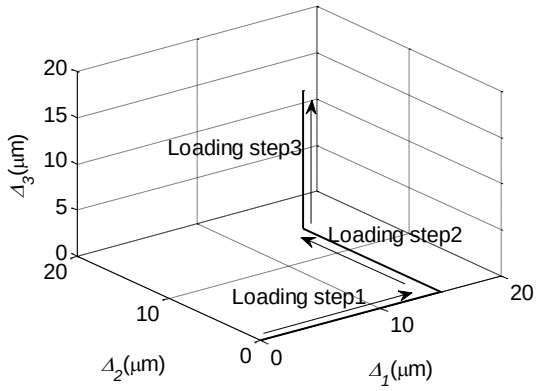

Figure 5.11: The 3-step normal-shear loading procedure.

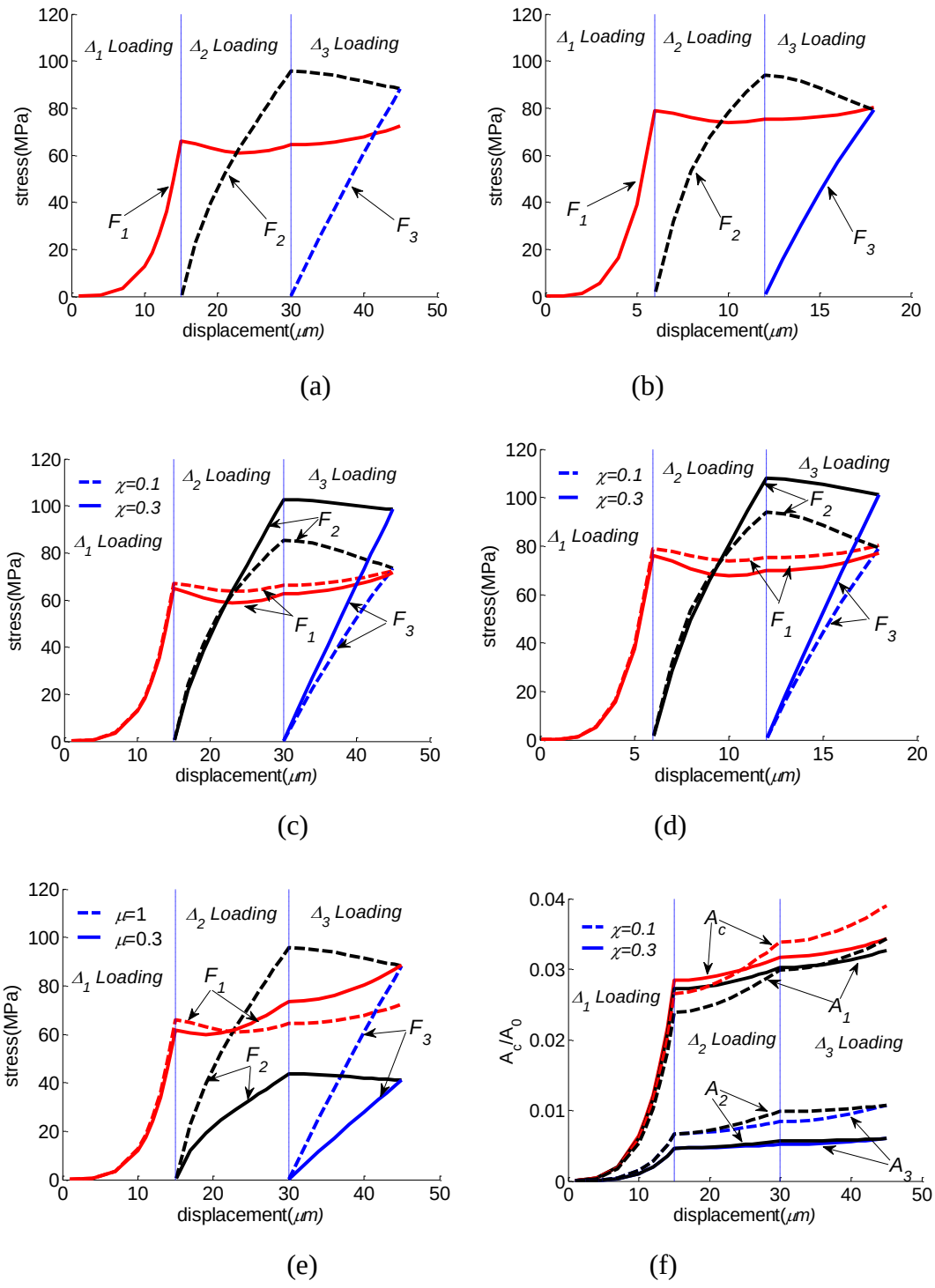

Figure 5.12: Coupling effect between normal and shear loading.

Figure 5.12 shows the resultant stress-displacement curves. During loading step 1, stress, F_1, increases as interface undergoes closure. Under shear loading in step 2, the normal stress, F_1, increases although the normal displacement, Δ_1, is kept constant. The increase in normal stress shows the coupling between the normal and shear behavior induced by the shear loading and is indicative of the fact that the interface is constrained from dilating. As we now apply the shear loading in step 3 while keeping the normal displacement, Δ_1, and the shear displacement, Δ_2, we see further coupling develop between the normal-shear and shear directions. During this loading step, we find a significant difference between the shear stresses, F_1 and F_2, although the corresponding shear displacements may be the same, showing a clear manifestation of the loading induced anisotropy. At the asperity contact-level, the no-contact, no-sliding and sliding areas evolve in response to the applied load-path. The result, of course, is a highly load path dependent overall behavior.

To study the orientation effect, in Figure 5.12 (c) and (d), we choose two different values of asperity contact orientation parameter (χ=0.1 and χ=0.3) for the interface S1 and R1 for comparison. Again, we can see the orientation plays a significant role in both in normal and shear behavior. It is noted that larger χ leads to stronger coupling effect between normal and shear.

To further illustrate how the stress-displacement behavior changes as a function of the surface characteristics, we plot the stress-displacement curves for different asperity friction coefficients (μ*=1 and* μ*=0.3)*, in Figure 5.12(e), for the interface R1. Small μ leads to more asperities sliding. Thus the shear resistance of the interface can be reduced significantly.

The contact area change during the loading process is also illustrative of the coupling phenomena as seen from Figure 5.12(f). In this case, we choose two different values of asperity contact orientation parameter (χ=0.1 and χ=0.3) for the interface R1 for comparison. Here, A_c is the contact area; A_1, A_2 and A_3 are the projections of the contact area in axis 1, 2 and 3. We note that with the shear loading, the total contact area as well as the area projection in the 1-direction increases. This result is in contrast with the traditional view that the contact area depends solely on the normal loading. This implies that the shear resistance is not only a function of the normal loading but also a function of the shear loading.

5.8 Summary

The effect of asperity contact orientations on the stress-displacement behavior of rough interfaces has not been adequately investigated. Models based upon the composite topography approach, either ignore the asperity contact orientation or treat their effects in an approximate manner. As a consequence, these approaches have difficulty in

describing a number of phenomena observed during interface shear, such as dilation-contraction and shear displacement hardening. In this chapter, we have utilized a micromechanical model of rough interfaces to study the role of asperity contact orientations. This micromechanical model is based upon a methodology developed by the authors that considers asperity contacts and statistical description of interface roughness [29, 56, 58]. In the present approach, the asperity contact orientations are explicitly considered. The nonlinear stress-displacement equation system of the extended model is solved by the Newton-Raphson method for different loading conditions. We demonstrate the applicability of the derived model under a variety of loading conditions for smooth and rough interfaces, including comparisons with experimental results.

The numerical results demonstrate that the model replicates the closure and shear behavior of smooth and rough surfaces both qualitatively and quantitatively. We find that the rough interfaces generally have a larger asperity orientation extent than the smooth interfaces. The orientation plays a significant role when the interface is sheared following the application of normal loading. We also find that the coupling between the normal and the shear response, the interface frictional strength and the shear displacement hardening behavior are closely related to the asperity contact orientations.

Finally we observe that the shear behavior of the interfaces under constant normal stress should be considered in two distinct regimes of shear displacements. In the small shear displacement regime, the smooth interfaces stiffer in shear compared to the rough interfaces. As the shear displacement is increased and a large number asperity contacts reach their frictional resistance, the shear stress-displacements curves of the smooth and rough interfaces crossover. Thus, at the large shear displacement regime, the rough interfaces are found to have a higher shear resistance, and eventually, a higher frictional strength compared to smooth interfaces. While the smooth interfaces show an abrupt yield close to frictional strength, the rough interfaces exhibit a shear displacement hardening and gradual transition to frictional strength. This distinction in shear behavior with varying roughness can also be attributed to the asperity contact orientations.

This page left intentionally blank.

Chapter 6 Scale Dependent Property of the Rough Interface

Typically a profilometer is used to measure the surface roughness. When the profilometer goes through the surface, thousands of discrete points are obtained. The interval between two adjacent points is the resolution. Researchers surprisingly found that the resolution plays a very important role in the roughness measurement. Using different resolutions, different topographies are obtained such that the statistical parameters are resolution-dependent. The rough surfaces are, therefore, often considered to be scale-dependent. Another property that some surfaces possess is self-affinity; i.e., the surface is able to reproduce itself as the sampling-window is changed. In other words, these surfaces have the same configurations regardless of the sampling window. Such surface is well known as fractal geometry in mathematics. Many rough surfaces exhibit self-affine property over a range of scales of interest in engineering analysis. In this chapter, we consider self-affine rough surfaces and investigate their scale dependent interface behavior

6.1 Surface generation

There are several methods to generate fractal geometry, such as Weierstrass- Mandelbrot function, spectral synthesis method and the random midpoint displacement method (RMD). RMD method is widely used due to its simplicity. Basically, a recursive

algorithm is used to implement the self-affinity the surface displays. More details can be found in literature[80].

In Figure 6.1 and Figure 6.2, RMD method is used to generate two surfaces. In Figure 6.1, 32×32 points are used, thus the resolution is 1/(32×32); in Figure 6.2, the resolution is 1/(64×64). As we can see, when high resolution is used, the surface tends to be rougher based upon visual examination.

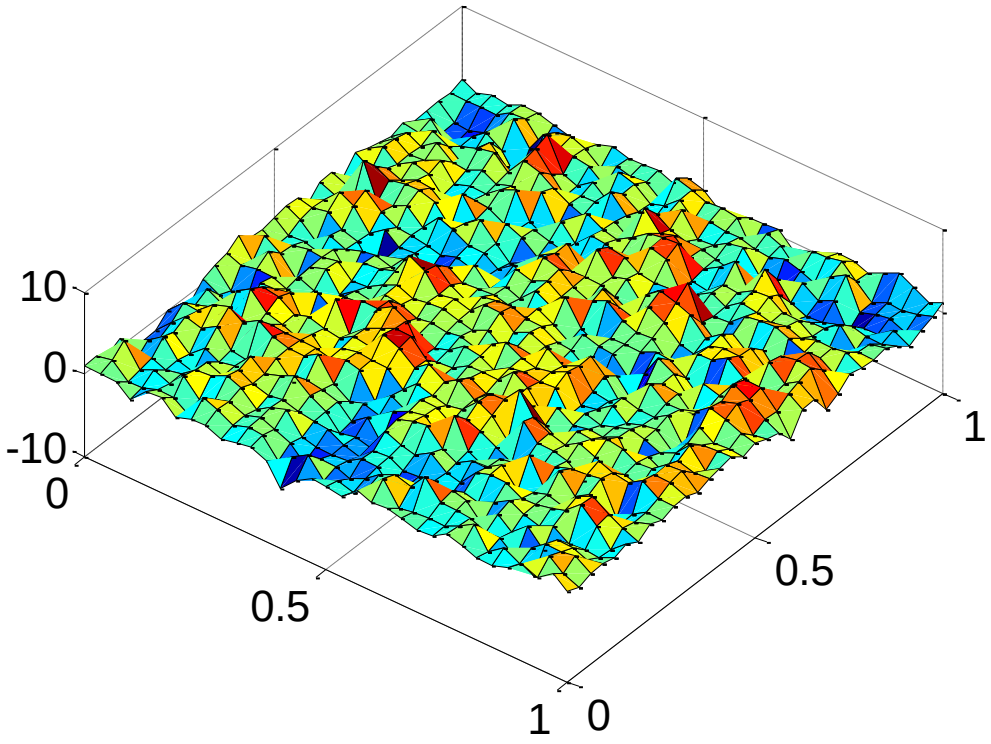

Figure 6.1: RMD method simulation for the rough surface (32×32).

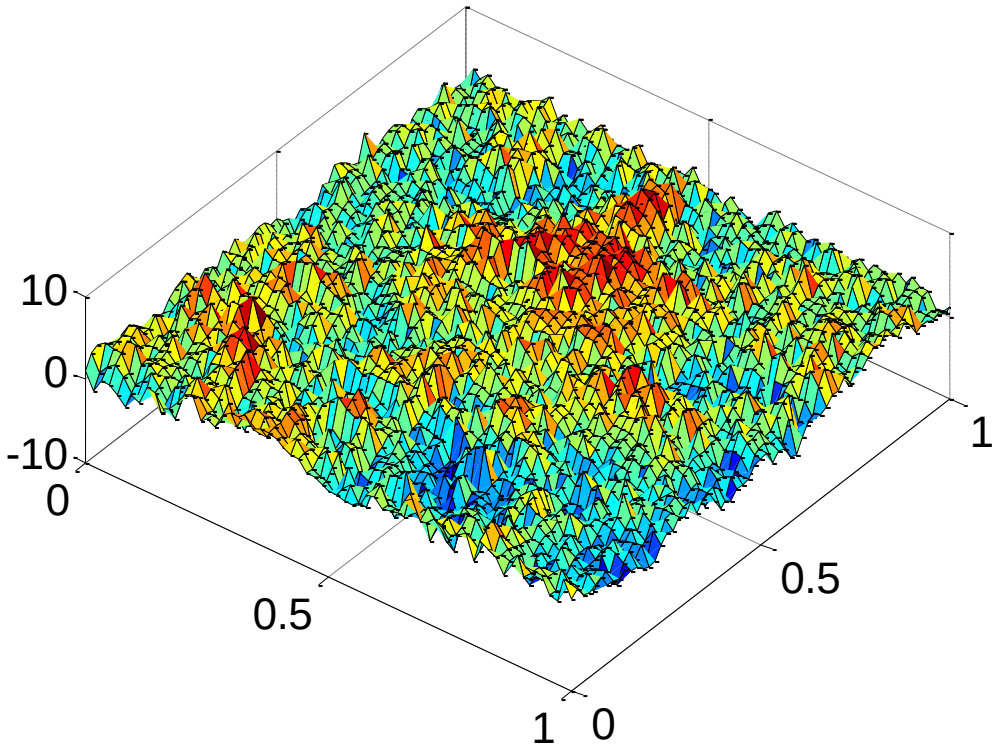

Figure 6.2: RMD method simulation for the rough surface (64×64).

6.2 The scale-dependency of the statistical parameters

Although the surfaces exhibit randomness and scale dependency, it has been observed that many engineering surfaces have similar spectra. In other words, those random surfaces in physical domain have the similar forms in frequency domain. Sayles and Thomas[84] gave the following form to express the PSD of the surface profile:

$$\Phi_{\phi}(\omega) = B\omega^{-(5-2D)} \tag{6.1}$$

where B is a constant determined by the surface roughness and ω is the wavelength; D is the profile fractal dimension ($1<D<2$).

Thus the moments of the profile can be written as using equation(4.9)

$$m_n = \int_{\omega_l}^{\omega_h} \omega^n \Phi_\phi(\omega) d\omega \tag{6.2}$$

where ω_l and ω_h are the low and high wave numbers, respectively, related to the resolution and sample size as

$$\begin{cases} \omega_l = \delta \\ \omega_h = L \end{cases} \tag{6.3}$$

where δ is the resolution and L the sample size. Given that, $L \gg \delta$, thus we have

$$m_0 \cong \frac{-B}{2D-4}\left(\frac{2\pi}{L}\right)^{2D-4} \tag{6.4}$$

$$m_2 \cong \frac{B}{2D-2}\left(\frac{2\pi}{\delta}\right)^{2D-2} \tag{6.5}$$

$$m_4 \cong \frac{B}{2D}\left(\frac{2\pi}{\delta}\right)^{2D} \tag{6.6}$$

Such that

$$\alpha = \frac{m_0 m_4}{m_2^2} = \left(\frac{\delta}{L}\right)^{2D-4} \frac{1-D}{D} \tag{6.7}$$

The other parameters based on m_0, m_2 and m_4 in chapter 4 can be easily obtained as follows:

$$N = \frac{1}{6\pi\sqrt{3}}\left(m_4 / m_2\right) = \frac{1}{6\pi\sqrt{3}}\left(\frac{D-1}{D}\right)\left(\frac{2\pi}{\delta}\right)^2 \tag{6.8}$$

$$R_m = \frac{0.76}{\sqrt{m_4}} = \frac{\delta^D}{(2\pi)^D}\sqrt{\frac{2D}{B}} \tag{6.9}$$

$$\sigma = \sqrt{m_0} \cong \left(\frac{-B}{2D-4}\left(\frac{2\pi}{L}\right)^{2D-4}\right)^{1/2} \tag{6.10}$$

$$\chi = 2m_2 \cong \frac{B}{D-1}\left(\frac{2\pi}{\delta}\right)^{2D-2} \tag{6.11}$$

6.3 Numerical study of Scale dependency on the surface statistical parameters

In this section, we study the interface property with different fractal dimension, sample size and resolution. The interface properties used for our example computations are tabulated in Table 2. It is noted that the values inside the squares in Table 2 are options for comparison. Based on the basic interface property, statistical parameters can be obtained as we discussed in last section. Table 3,Table 4 and Table 5 are the statistical parameters with different fractal dimension, sample size and resolution.

Table 2: Interface property for composite topography.

Parameters	value
Sample size L	2[1 2 3]mm
Resolution δ	20[10 20 30]μm
Fractal dimension D	1.35[1.3 1.35 1.4]

Asperity friction, μ	1
Shear modulus, G	8.0 GPa
Poisson's ratio, ν	0.3
Surface constant B	0.14E-5

Table 3: Interface statistical parameters under different fractal dimension D.

D	1.3	1.35	1.4
$N(m^2)$	6.98E+08	7.84E+08	8.64E+08
$R_m(\mu m)$	64.01292	34.64219	18.73462
α	62.40237	55.57621	47.84546
$\sigma(\mu m)$	3.601318	5.589994	8.702617

Table 4: Interface statistical parameters under different sample size L.

L	1	2	3
$N(m^2)$	7.84E+08	7.84E+08	7.84E+08
$R_m(\mu m)$	34.64219	34.64219	34.64219
α	22.57096	55.57621	94.14724
$\sigma(\mu m)$	3.562393	5.589994	7.27563

Table 5: Interface statistical parameters under different resolutions δ.

$\delta(\mu m)$	10	20	30
$N(m^2)$	3.13E+09	7.84E+08	3.48E+08
$R_m(\mu m)$	13.58986	34.64219	59.88645
α	136.8447	55.57621	32.80729
$\sigma(\mu m)$	5.589994	5.589994	5.589994

As we can see in Figure 6.3, fractal dimension D has a strong effect on both asperity contact height and orientation probability distribution. As D increases, the distributions become wider. In other words, larger D leads to a rougher surface. Figure 6.4 shows that larger L leads to rough interface but no effect on orientation distribution. Figure 6.5 shows that high resolution gives a rougher interface but no effect on height distribution.

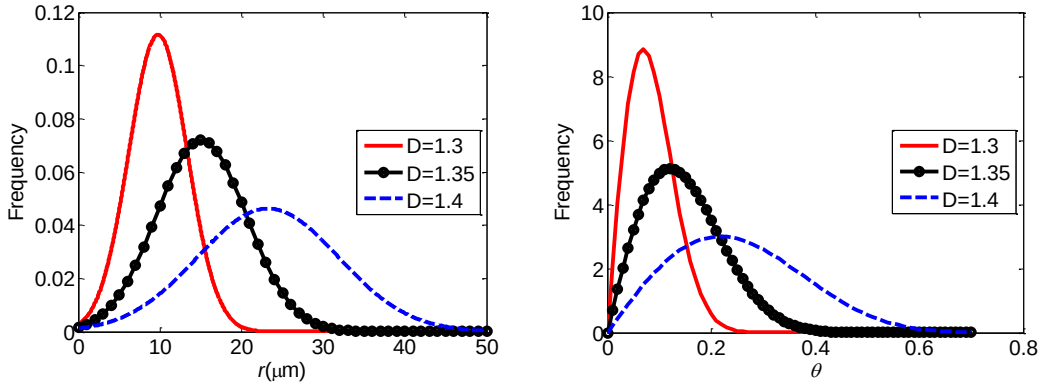

Figure 6.3: Fractal dimension D effect on asperity contact height and orientation distribution.

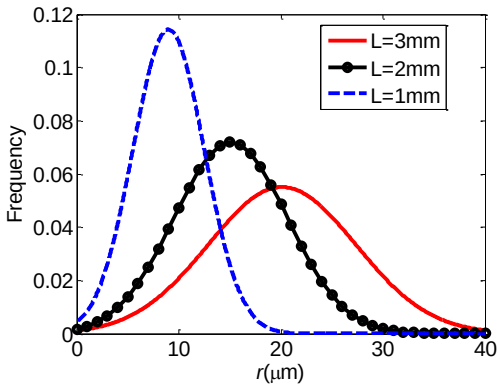

Figure 6.4: Sample size, L, effect on asperity contact height distribution.

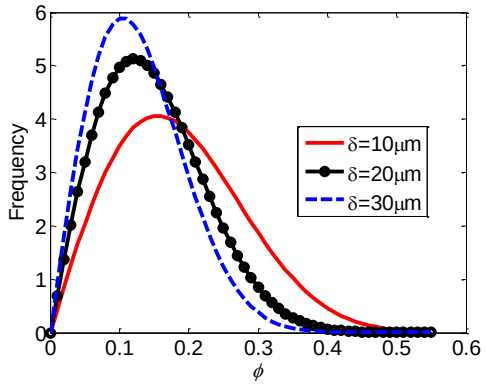

Figure 6.5: Effect of resolution, δ, on asperity contact orientation distribution.

In the subsequent sections, we demonstrate the applicability of the derived overall stress-displacement relationship and its numerical implementation in chapter 5 to study the scale dependency of the interface behavior under different loading conditions.

6.4 Normal behavior under different scales

Figure 6.6-Figure 6.8 shows the computed normal behavior of the three interfaces considered in section 6.3. It is noted that the left figures demonstrate the displacement-stress curve, while the right figures demonstrate the displacement-contact area curve. We observe that the interface stiffness becomes softer with increasing fractal dimension D and increasing sample size L. Similar dependency on fractal dimension[85, 86] and sample size[87] have been observed in experiments as shown in Figure 6.9. As seen in section 6.3, higher D and L imply a rougher surface. Therefore, the results in Figure 6.6 are not surprising since the normal stiffness of rougher interface is generally softer than that of smoother interface as observed in chapter 5.

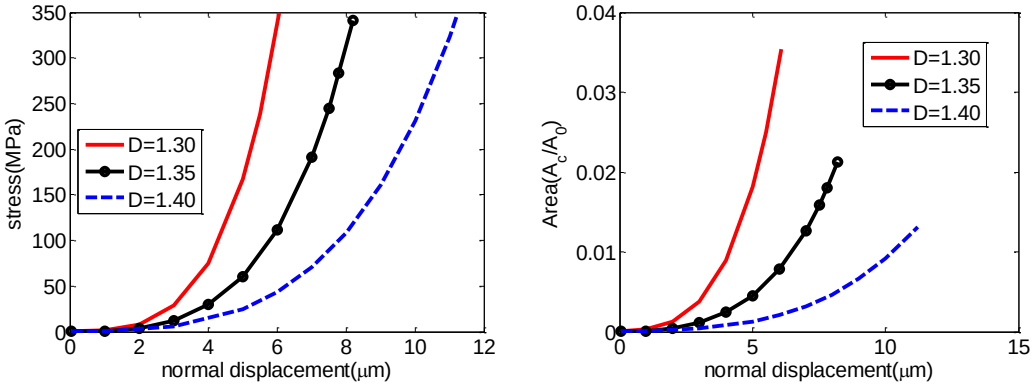

Figure 6.6: *D* effect on normal behavior.

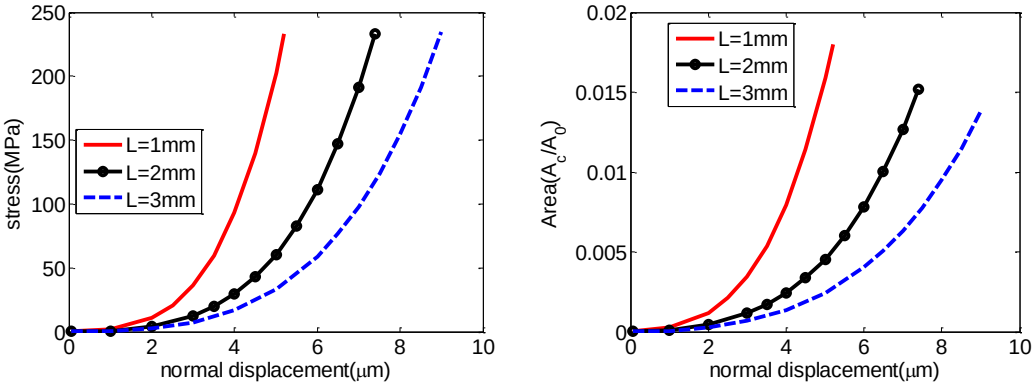

Figure 6.7: *L* effect on normal behavior.

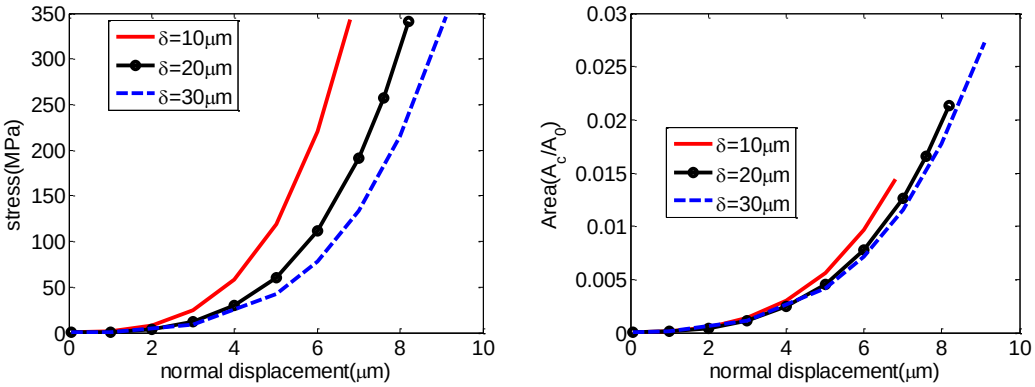

Figure 6.8: δ effect on normal behavior.

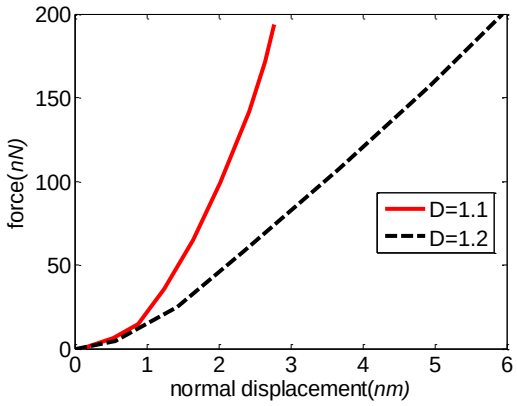

Figure 6.9: Experimental results[85] for the fractal dimension effect on normal behavior.

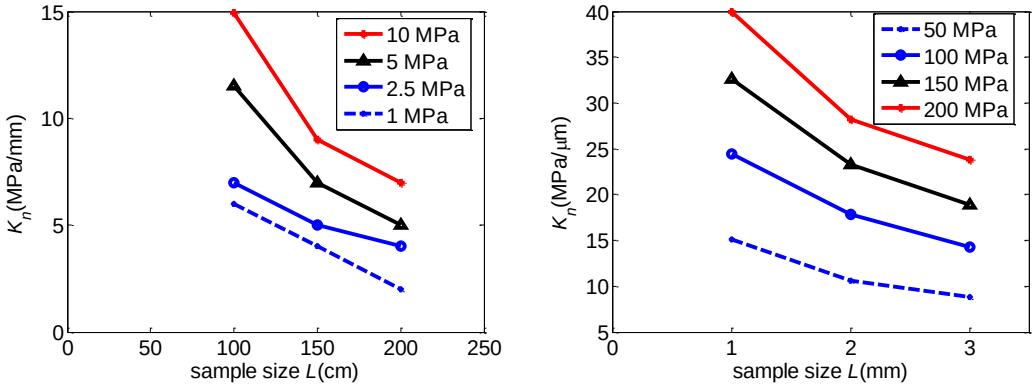

Figure 6.10: (a) Fardin's experiment[87] for sample size L effect on normal stiffness behavior; (b) Model prediction.

Similar observation is made for the resolution, where we note that coarser resolution results in a behavior that is akin to a rougher interface, while finer resolution results in behavior resembling smoother interface. The fine resolution results in reducing the mean radius curvature, which is reasonable since smaller asperities are revealed as finer resolutions are used. These smaller asperities can result in inclined contacts and we note that the orientation distribution tends towards rough interface. However, the asperity

contact density becomes large as more asperities are revealed and this affect causes the interface behavior to be stiffer or akin to a smooth interface.

6.5 Shear behavior under different scale

Figure 6.11-Figure 6.13 shows the computed shear behavior of the three interfaces considered in section 6.3. As discussed in chapter 5, the shear behavior can be considered in two regimes. In the small shear displacement regime, we observe that the interface behavior significantly stiffer with decreasing fractal dimension *D*. At the large shear displacement regime, we observe that the curves crossover and surfaces with smaller *D* fail at smaller shear resistance. Such cross-over behavior was also observed in chapter 5 when comparing smooth and rough interfaces and has also been observed in experimental results. The variation with *D* obtained here is reasonable since smaller fractal dimension implies a smoother surface as seen from the discussion in section 6.3. Further, we find that the behavior is stiffer for smaller sample size, *L*. Similar dependence of interface shear stiffness on sample size[87] has been observed in experiments as shown in Figure 6.14. The behavior is also consistent with the observations regarding smooth and rough interfaces since larger sample size implies a rougher interface, as discussed section 6.3. However, no crossover behavior is observed with the change of sample size, *L*. We note that sample size only effects the height

distribution. The cross-over behavior is intimately related to the asperity contact orientation distribution.

Similar observation is made for the resolution, where we note that coarser resolution results in a behavior that is akin to a rougher interface, while finer resolution results in behavior resembling smoother interfaces.

The shear behavior based upon finer resolution is found to be stiffer with no cross-over. The fine resolution results in revealing smaller asperities which form inclined contacts, such that the orientation distribution tends towards a rough interface. In addition, the asperity contact density becomes large as more asperities are revealed and this affect causes the interface behavior to be stiffer or akin to a smooth interface.

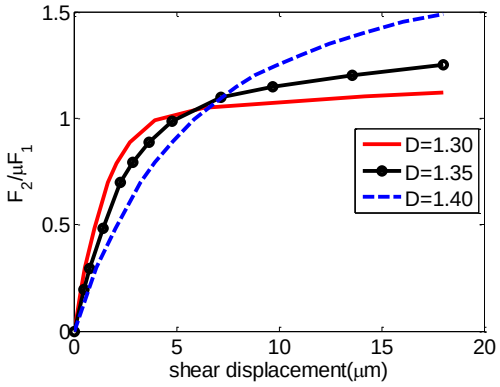

Figure 6.11: *D* effect on shear behavior.

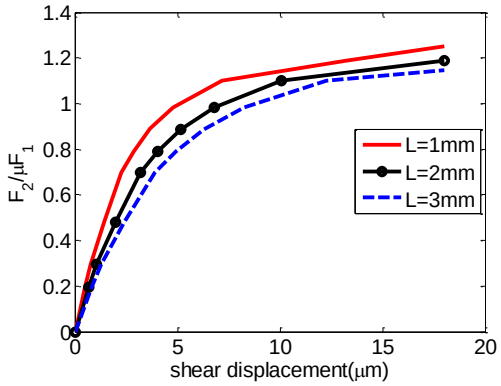

Figure 6.12: *L* effect on shear behavior.

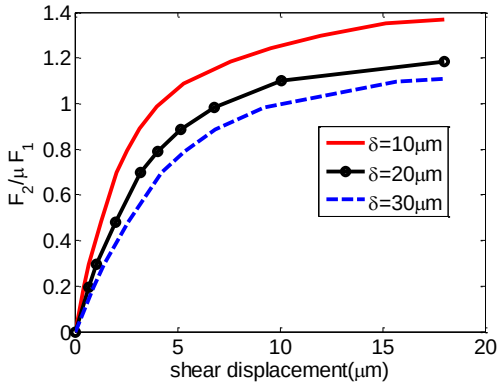

Figure 6.13: δ effect on shear behavior.

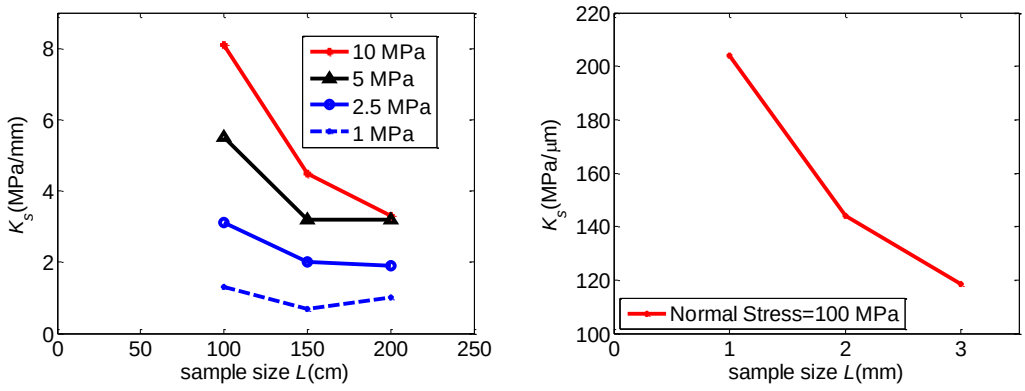

Figure 6.14: (a) Fardin's experiment for sample size *L* effect on shear stiffness behavior; (b) Model prediction.

6.6 Summary

In this chapter, we discussed the scale effect on the behavior of rough surface. We found that larger fractal dimension D leads to the rougher surface. Both of the asperity contact height distribution and orientation are affected by D. The sample size L also plays a very important role on asperity contact height distribution but no effect on orientation distribution. Larger L leads to rougher surface. In contrast to sample size L, resolution δ has no effect on asperity contact height distribution but have effect on orientation distribution. High resolution gives a rougher surface.

Furthermore, we found that normal and shear behavior are also scale dependent. Roughly speaking, rough surface has a low normal stiffness. However, when both height and orientation distribution tend to rough, shear behavior experiences two stages: the first loading stage exhibits smooth surface has higher shear stiffness while the second stage shows that rough surface has higher stiffness. If only either asperity contact height or orientation distribution tends to rough, two stages behavior is not observed. Therefore, surface parameters should include asperity contact height and orientation distribution.

We note that the scale-dependency as modeled in this work will lead to zero contact area as the resolution is decreased. Furthermore, the behavior retains scale-dependency as the sample-size is increased infinitely. Such behaviors in the limits are unreasonable. Although, scale-dependency is observed in experiments, it is clear such observations

must have limits. In other words, the self-affinity occurs only over ranges of resolution and sample size. Beyond these ranges, the surfaces cannot be considered fractal and they should be treated as stationary surfaces. Future work will incorporate appropriate PSD that transition from fractal behavior to stationary behavior at both small-scales (corresponding to resolution) and large scales (corresponding to sample sizes).

This page left intentionally blank.

Chapter 7 Summary and future work

Interfaces formed by contacting rough surfaces are ubiquitous in nature and their mechanical behavior is of significance in many areas of engineering. In this dissertation, we have used the statistical approach to study the interface mechanical behavior under combined normal and shear loading. We have first discussed the local behavior of the interface, i.e., asperity contact behavior. Then we have further developed the statistical description for the rough contacting surfaces. Finally, we have used homogenization of asperity contact to obtain the interface behavior. Here we summarize the work accomplished and provide a synopsis of the main findings of this dissertation. The potential future work is also discussed briefly.

(1) *Asperity contact modeling under oblique loading*: Asperity contacts were modeled as contact between spherical elastic bodies. Although, the contacts of spherical bodies have been studied since the pioneering work of Hertz more than a century ago, there are number of aspects that need further work. In chapter 2, we have extended the continuous method proposed by Mindlin and Deresiewicz to contacts under oblique forces whose inclination is different at different loading stages. We have presented a general procedure for obtaining the tangential traction at any loading stage of both monotonic and cyclic loading. The procedure updates the tangential traction with loading, thus it has the ability

to account for the effect of loading history on the contact behavior. It was demonstrated that the tangential displacement, compliance and energy dissipation can be totally different for different loading paths although the final loading state may be the same.

(2) *Asperity contact modeling under out-of-plane loading*: For rough surface contact subjected to combined normal and shear loads, it can be anticipated that asperity contact will experience shear loads that are not confined within a unique normal-shear loading plane. In chapter 3 we have developed the asperity contact model under out-of-plane loading condition. We have found that under such general loading condition, the contact undergoes simultaneous loading and unloading in orthogonal directions on the shear plane. Thus the tangential traction, displacement and compliance cannot be merely labeled as that for loading or unloading condition. Moreover, due to its path dependent nature, the tangential traction cannot be simplified as that due to a resultant force. Instead, for each shear force application, the entire loading history has to be considered.

(3) *Statistical description of rough interface geometry*: The contact of two rough surfaces occurs at their asperities. The number density of the resultant asperity contacts under a given loading depends upon the asperity contact heights. In addition, the mechanical behavior and the loading condition of an asperity contact depends upon its

curvature and orientations. In chapter 4 we have developed the statistical description for the rough interface based upon Longuet-Higgins random process analysis for the rough sea surface. We have derived the joint probability distribution of asperity contact heights and curvatures. We have also derived a probability distribution function for asperity contact orientations. These distributions are shown to be essential for the homogenization model of interface mechanical behavior.

(4) *Homogenization model of rough interface mechanics*: The overall mechanical behavior of a rough interface is closely related to the asperity contact behavior. In chapter 5, we have developed homogenization model based on micromechanical approach. This micromechanical approach is based upon displacement consistency between the asperity contact and interface and utilizes the statistical descriptions derived in chapter 4. The resultant model is applied to study the interface mechanical behavior under combined normal and shear loading. It was shown that the asperity contact statistics play a significant role in the interface behavior. The coupling between the normal and the shear response, the interface frictional strength and the shear displacement hardening behavior were shown to be closely related to the asperity contact orientations. Finally we observe that at small shear displacements, the smooth interfaces are stiffer compared to the rough interfaces, while at the large shear displacements, the rough interfaces are found to have a higher shear resistance compared to smooth

interfaces. This crossover in the shear behavior with varying roughness can also be attributed to the asperity contact orientations.

(5) *Scale dependence of rough interface mechanics*: The resolution of surface sampling as well as the sample size can affect the statistics of the interface geometry. In chapter 6 we have discussed the effect of this scale-dependency upon the interface contact behavior. The surfaces are treated as self-affine fractal geometries to obtain scale-dependent parameters of asperity contact probability distributions in terms of the measurement resolution, sample size and surface fractal dimension. We have found that larger fractal dimensions lead to rougher surfaces. We have also found that the asperity contact height and orientation distributions are affected by fractal dimension. The sample size plays an important role in determining the asperity contact height distribution but has no effect on orientation distribution. We have found that larger sample size leads to a rougher surface. Finally, in contrast to sample size, resolution is found to have no effect on height distribution but has an effect on orientation distribution. The influence of these changes in asperity contact statistics on the interface mechanical behavior is discussed in details.

This dissertation has focused upon fundamental aspects of rough interface behavior. The method developed in this work can be potentially extended to incorporate the following aspects:

(1) Anisotropic statistical description of rough interface.

(2) Plasticity, damage and cyclic behavior of asperity contact.

(3) The range of the scale dependency of rough interface.

(4) Rate- and time-dependent behavior of rough interfaces.

(5) Dynamic and wave propagation behavior of rough interfaces.

The developed interface behavior will find applications in discrete element modeling of granular materials, jointed and fractured rocks, and friction prediction and tribology of machine parts.

This page left intentionally blank.

References

1. Hertz, H., *On the contact of rigid elastic solids and on hardness.* Verhandlungen des Vereins zur Befoderung des Gewerbefleisses, 1882.
2. Hertz, H., *On the contact of elastic solids.* Journal fur de reine und angewandte Mathematik, 1881. **92**: p. 156-171.
3. Mindlin, R.D. and H. Deresiewicz, *Elastic Spheres in Contact under Varying Oblique Forces.* Journal of Applied Mechanics-Transactions of the Asme, 1953. **20**(3): p. 327-344.
4. Archard, J.F., *Elastic Deformation and the Laws of Friction.* Proceedings of the Royal Society of London Series a-Mathematical and Physical Sciences, 1957. **243**(1233): p. 190-205.
5. Bowden, F.P. and D. Tabor, *the friction and lubrication of solids.* 1950.
6. Greenwood, J.A. and J.B. Williamson, *Contact of Nominally Flat Surfaces.* Proceedings of the Royal Society of London Series a-Mathematical and Physical Sciences, 1966. **295**(1442): p. 300-319.
7. Greenwood, J.A. and J.H. Tripp, *The contact of two nominally flat rough surfaces.* Proceedings of the Institution of Mechanical Engineers, 1971. **185**: p. 625-633.
8. Wriggers, P. and T.A. Laursen, *Computational Contact Mechanics*. CISM International Centre for Mechanical Sciences, 4982008, Vienna: CISM.
9. Shankar, S. and M.M. Mayuram, *A finite element based study on the elastic-plastic transition behavior in a hemisphere in contact with a rigid flat.* Journal of Tribology-Transactions of the Asme, 2008. **130**(4): p. 044502-1-6.
10. Wriggers, P., *Computational contact mechanics*. 2nd ed2006, Berlin ; New York: Springer. xii, 518 p.
11. Hyun, S., et al., *Finite-element analysis of contact between elastic self-affine surfaces.* Physical Review E, 2004. **70**(2): p. 026117-1-12.
12. Laursen, T.A., *Computational Contact and Impact Mechanics*2002, New York: Springer. 454.
13. Yoshioka, N., *Elastic Behavior of Contacting Surfaces under Normal Loads - a Computer-Simulation Using 3-Dimensional Surface Topographies.* Journal of Geophysical Research-Solid Earth, 1994. **99**(B8): p. 15549-15560.
14. Majumdar, A. and B. Bhushan, *Role of Fractal Geometry in Roughness Characterization and Contact Mechanics of Surfaces.* Journal of Tribology-Transactions of the Asme, 1990. **112**(2): p. 205-216.
15. Persson, B.N.J., et al., *On the nature of surface roughness with application to contact mechanics, sealing, rubber friction and adhesion.* Journal of Physics-Condensed Matter, 2005. **17**(1): p. R1-R62.
16. Yang, J. and K. Komvopoulos, *A mechanics approach to static friction of elastic-plastic fractal surfaces.* Journal of Tribology-Transactions of the Asme, 2005. **127**(2): p. 315-324.
17. Ciavarella, M., V. Delfine, and V. Demelio, *A new 2D asperity model with interaction for studying the contact of multiscale rough random profiles.* Wear, 2006. **261**(5-6): p. 556-567.

18. Whitehouse, D.J. and J.F. Archard, *Properties of Random Surfaces of Significance in Their Contact.* Proceedings of the Royal Society of London Series a-Mathematical and Physical Sciences, 1970. **316**(1524): p. 97-121.
19. Nayak, P.R., *Random Process Model of Rough Surfaces.* Journal of Lubrication Technology, 1971. **93**(3): p. 398-407.
20. Bush, A.W., R.D. Gibson, and T.R. Thomas, *Elastic Contact of a Rough Surface.* Wear, 1975. **35**(1): p. 87-111.
21. Bush, A.W., R.D. Gibson, and G.P. Keogh, *Strongly Anisotropic Rough Surfaces.* Journal of Lubrication Technology-Transactions of the Asme, 1979. **101**(1): p. 15-20.
22. Adler, R.J. and D. Firman, *A Non-Gaussian Model for Random Surfaces.* Philosophical Transactions of the Royal Society of London Series a-Mathematical Physical and Engineering Sciences, 1981. **303**(1479): p. 433-462.
23. Mccool, J.I. and S.S.Gassel, *The contact of two surfaces having anisotropic roughness geometry*, in *Energy technology, Special Publication*1981, American Society of Lubrication Engineers: New York. p. 29-38.
24. Brown, S.R. and C.H. Scholz, *Closure of Random Elastic Surfaces in Contact.* Journal of Geophysical Research-Solid Earth and Planets, 1985. **90**(Nb7): p. 5531-5545.
25. Brown, S.R. and C.H. Scholz, *Closure of Rock Joints.* Journal of Geophysical Research-Solid Earth and Planets, 1986. **91**(B5): p. 4939-4948.
26. Chang, W.R., I. Etsion, and D.B. Bogy, *An Elastic-Plastic Model for the Contact of Rough Surfaces.* Journal of Tribology-Transactions of the Asme, 1987. **109**(2): p. 257-263.
27. Yoshioka, N. and C.H. Scholz, *Elastic Properties of Contacting Surfaces under Normal and Shear Loads .1. Theory.* Journal of Geophysical Research-Solid Earth and Planets, 1989. **94**(B12): p. 17681-17690.
28. Yoshioka, N. and C.H. Scholz, *Elastic Properties of Contacting Surfaces under Normal and Shear Loads .2. Comparison of Theory with Experiment.* Journal of Geophysical Research-Solid Earth and Planets, 1989. **94**(B12): p. 17691-17700.
29. Misra, A., *Mechanistic model for contact between rough surfaces.* Journal of Engineering Mechanics-Asce, 1997. **123**(5): p. 475-484.
30. Vignjevic, R., T. De Vuyst, and J.C. Campbell, *A frictionless contact algorithm for meshless methods.* Computer Modeling in Engineering & Sciences, 2006. **13**(1): p. 35-47.
31. Han, Z.D., et al., *The applications of meshless local Petrov-Galerkin (MLPG) approaches in high-speed impact, penetration and perforation problems.* Cmes-Computer Modeling in Engineering & Sciences, 2006. **14**(2): p. 119-128.
32. Selvadurai, A.P.S. and Q. Yu, *Mechanics of discontinuity in a geomaterial.* Computers and Geotechnics, 2005. **32**(2): p. 92-106.
33. Sellgren, U., S. Bjorklund, and S. Andersson, *A finite element-based model of normal contact between rough surfaces.* Wear, 2003. **254**(11): p. 1180-1188.
34. Buczkowski, R. and M. Kleiber, *Statistical Models of Rough Surfaces for Finite Element 3D-Contact Analysis.* Archives of Computational Methods in Engineering, 2009. **16**(4): p. 399-424.

35. Nayak, P.R., *Some Aspects of Surface-Roughness Measurement.* Wear, 1973. **26**(2): p. 165-174.
36. Nayak, P.R., *Random Process Model of Rough Surfaces in Plastic Contact.* Wear, 1973. **26**(3): p. 305-333.
37. Yamada, K., et al., *Surface Density of Asperities and Real Distribution of Asperity Heights on Rubbed Surfaces.* Wear, 1978. **47**(1): p. 5-20.
38. Yamada, K., et al., *Mechanisms of Elastic Contact and Friction between Rough Surfaces.* Wear, 1978. **48**(1): p. 15-34.
39. Mccool, J.I., *Comparison of Models for the Contact of Rough Surfaces.* Wear, 1986. **107**(1): p. 37-60.
40. Ozaki, S., et al., *Finite element analysis of particle assembly-water coupled frictional contact problem.* Cmes-Computer Modeling in Engineering & Sciences, 2007. **18**(2): p. 101-119.
41. Guz, A.N., et al., *Contact problem for the flat elliptical crack under normally incident shear wave.* Cmes-Computer Modeling in Engineering & Sciences, 2007. **17**(3): p. 205-214.
42. Guz, A.N. and V.V. Zozulya, *Investigation of the effect of frictional contact in III-mode crack under action of the SH-Wave harmonic load.* Computer Modeling in Engineering & Sciences, 2007. **22**(2): p. 119-128.
43. Persson, B.N.J., et al., *Contact area between a viscoelastic solid and a hard, randomly rough, substrate.* Journal of Chemical Physics, 2004. **120**(18): p. 8779-8793.
44. Abuzeid, O.M. and P. Eberhard, *Linear viscoelastic creep model for the contact of nominal flat surfaces based on fractal geometry: Standard linear solid (SLS) material.* Journal of Tribology-Transactions of the Asme, 2007. **129**(3): p. 461-466.
45. Farhang, K. and A. Lim, *A kinetic friction model for viscoelastic contact of nominally flat rough surfaces.* Journal of Tribology-Transactions of the Asme, 2007. **129**(3): p. 684-688.
46. Haiat, G. and E. Barthel, *An approximate model for the adhesive contact of rough viscoelastic surfaces.* Langmuir, 2007. **23**(23): p. 11643-11650.
47. Kogut, L. and I. Etsion, *A static friction model for elastic-plastic contacting rough surfaces.* Journal of Tribology-Transactions of the Asme, 2004. **126**(1): p. 34-40.
48. Mukherjee, S., S.M. Ali, and P. Sahoo, *An improved elastic-plastic contact model of rough surfaces in the presence of adhesion.* Proceedings of the Institution of Mechanical Engineers Part J-Journal of Engineering Tribology, 2004. **218**(J6): p. 557-567.
49. Hariri, A., J.W. Zu, and R. Ben Mrad, *Modeling of elastic/plastic contact between nominally flat rough surfaces using an n-point asperity model.* Journal of Tribology-Transactions of the Asme, 2006. **128**(4): p. 876-885.
50. Nelias, D., V. Boucly, and M. Brunet, *Elastic-plastic contact between rough surfaces: Proposal for a wear or running-in model.* Journal of Tribology-Transactions of the Asme, 2006. **128**(2): p. 236-244.
51. Konyukhov, A., P. Vielsack, and K. Schweizerhof, *On coupled models of anisotropic contact surfaces and their experimental validation.* Wear, 2008. **264**(7-8): p. 579-588.

52. Lin, L.P. and J.F. Lin, *An elliptical elastic-plastic microcontact model developed for an ellipsoid in contact with a smooth rigid flat.* Journal of Tribology-Transactions of the Asme, 2007. **129**(4): p. 772-782.
53. Jones, R.E. and P. Papadopoulos, *Simulating anisotropic frictional response using smoothly interpolated traction fields.* Computer Methods in Applied Mechanics and Engineering, 2006. **195**(7-8): p. 588-613.
54. Buczkowski, R. and M. Kleiber, *Elasto-plastic statistical model of strongly anisotropic rough surfaces for finite element 3D-contact analysis.* Computer Methods in Applied Mechanics and Engineering, 2006. **195**(37-40): p. 5141-5161.
55. Hjiaj, M., et al., *On the modelling of complex anisotropic frictional contact laws.* International Journal of Engineering Science, 2004. **42**(10): p. 1013-1034.
56. Misra, A., *Micromechanical model for anisotropic rock joints.* Journal of Geophysical Research-Solid Earth, 1999. **104**(B10): p. 23175-23187.
57. Misra, A., *Effect of asperity damage on shear behavior of single fracture.* Engineering Fracture Mechanics, 2002. **69**(17): p. 1997-2014.
58. Misra, A. and S. Huang, *Micromechanics based stress-displacement relationships of rough contacts: Numerical implementation under combined normal and shear loading.* Cmes-Computer Modeling in Engineering & Sciences, 2009. **52**(2): p. 197-215.
59. Misra, A. and S. Huang, *Effect of loading induced anisotropy on the shear behavior of rough interfaces.* Tribology International, 2011. **doi:10.1016/j.triboint.2010.12.010**.
60. Ford, I.J., *Roughness Effect on Friction for Multi-Asperity Contact between Surfaces.* Journal of Physics D-Applied Physics, 1993. **26**(12): p. 2219-2225.
61. Thornton, C. and C.W. Randall, eds. *Applications of theoretical contact mechanics to solid particle system simulation*. Micromechanics of granular materials, ed. M.Satake and J.T. Jenkins1987, Elsevier: the Netherlands. 245-252.
62. Dobry, R., et al., *General-Model for Contact Law between Two Rough Spheres.* Journal of Engineering Mechanics-Asce, 1991. **117**(6): p. 1365-1381.
63. Mindlin, R.D., *Compliance of Elastic Bodies in Contact.* Journal of Applied Mechanics-Transactions of the Asme, 1949. **16**(3): p. 259-268.
64. Johnson, K.L., *Contact mechanics*1985, Cambridge: Cambridge University Press. 452 p.
65. Aleshin, V. and K. Van Den Abeele, *Preisach analysis of the Hertz-Mindlin system.* Journal of the Mechanics and Physics of Solids, 2009. **57**(4): p. 657-672.
66. Jager, J., *Elastic Contact of Equal Spheres under Oblique Forces.* Archive of Applied Mechanics, 1993. **63**(6): p. 402-412.
67. Cundall, P.A. and O.D.L. Strack, *Discrete Numerical-Model for Granular Assemblies.* Geotechnique, 1979. **29**(1): p. 47-65.
68. Vu-Quoc, L. and X. Zhang, *An accurate and efficient tangential force-displacement model for elastic frictional contact in particle-flow simulations.* Mechanics of Materials, 1999. **31**(4): p. 235-269.
69. Cattaneo, C., *Sul contatto di due corpi elasti:distribuzione locale degli sforzi.* Rendicotti dell' Accademia dei lincei, 1938. **27**(6): p. 342-348.

70. Kruggel-Emden, H., S. Wirtz, and V. Scherer, *Applicable Contact Force Models for the Discrete Element Method: The Single Particle Perspective.* Journal of Pressure Vessel Technology-Transactions of the Asme, 2009. **131**(2): p. 024001-1-11.
71. Zhu, H.P., et al., *Discrete particle simulation of particulate systems: Theoretical developments.* Chemical Engineering Science, 2007. **62**(13): p. 3378-3396.
72. Deresiewicz, H., *Contact of Elastic Spheres under an Oscillating Torsional Couple.* Journal of Applied Mechanics-Transactions of the Asme, 1954. **21**(1): p. 52-56.
73. Hills, D.A. and A. Sackfield, *The Stress-Field Induced by a Twisting Sphere.* Journal of Applied Mechanics-Transactions of the Asme, 1986. **53**(2): p. 372-378.
74. Lubkin, J.L., *The Torsion of Elastic Spheres in Contact.* Journal of Applied Mechanics-Transactions of the Asme, 1951. **18**(2): p. 183-187.
75. Munisamy, R.L., D.A. Hills, and D. Nowell, *Static Axisymmetrical Hertzian Contacts Subject to Shearing Forces.* Journal of Applied Mechanics-Transactions of the Asme, 1994. **61**(2): p. 278-283.
76. Etsion, I., *Revisiting the Cattaneo-Mindlin Concept of Interfacial Slip in Tangentially Loaded Compliant Bodies.* Journal of Tribology-Transactions of the Asme, 2010. **132**(2): p. 020801-1-9.
77. Longuet-Higgins, M.S., *The statistical analysis of a random, moving surface.* Philosophical Transactions of the Royal Society of London. Series A. Mathematical and Physical Sciences, 1957. **249**(966): p. 321-387.
78. Longuet-Higgins, M.S., *Statistical Properties of an Isotropic Random Surface.* Philosophical Transactions of the Royal Society of London Series a-Mathematical and Physical Sciences, 1957. **250**(975): p. 157-174.
79. Carbone, G., *A slightly corrected Greenwood and Williamson model predicts asymptotic linearity between contact area and load.* Journal of the Mechanics and Physics of Solids, 2009. **57**(7): p. 1093-1102.
80. Zavarise, G. and M. Paggi, *Reliability of Micromechanical Contact Models: a Still Open Issue*, in *CISM International Centre for Mechanical Sciences, 498*, P. Wriggers and T.A. Laursen, Editors. 2008, CISM, Udine: Vienna.
81. Zavarise, G., M. Borri-Brunetto, and M. Paggi, *On the resolution dependence of micromechanical contact models.* Wear, 2007. **262**(1-2): p. 42-54.
82. Greenwood, J.A., *A simplified elliptic model of rough surface contact.* Wear, 2006. **261**(2): p. 191-200.
83. Biegel, R.L., et al., *Micromechanics of rock friction, 1, Effects of surface roughness of initial friction and slip hardening in Westerly Granite.* Journal of Geophysical Research-Solid Earth, 1992. **97**: p. 8951-8964.
84. Sayles, R.S. and T.R. Thomas, *Surface-Topography as a Nonstationary Random Process.* Nature, 1978. **271**(5644): p. 431-434.
85. Buzio, R., et al., *The contact mechanics of fractal surfaces.* Nature Materials, 2003. **2**(4): p. 233-236.
86. Xie, H.P., J.A. Wang, and W.H. Xie, *Fractal effects of surface roughness on the mechanical behavior of rock joints.* Chaos Solitons & Fractals, 1997. **8**(2): p. 221-252.

87. Fardin, N., *Influence of structural non-stationarity of surface roughness on morphological characterization and mechanical deformation of rock joints.* Rock Mechanics and Rock Engineering, 2008. **41**(2): p. 267-297.